Development and evaluation of a near-infrared photovoltaic implant for wireless neural stimulation

Danashi Imani MEDAGODA

École
polytechnique
fédérale
de Lausanne

2024

It turns out life isn't a puzzle that can be solved
one time and it's done. You wake up every day,
and you solve it again.
— Chidi Anagonye, *The Good Place*

To my parents…

Acknowledgements

First and foremost, I have been incredibly fortunate to have not one, but two exceptional advisors who have shaped my PhD experience. I extend my deepest gratitude to Dr Diego Ghezzi, who first welcomed me into his research group and provided early guidance and support. His door was always open for questions, and he consistently encouraged me to explore my own ideas and interests, fostering an environment of intellectual curiosity and independent thinking. I am equally thankful to Prof Stéphanie Lacour, who graciously took me under her wing and offered invaluable mentorship throughout the remainder of my studies. Their combined expertise, diverse perspectives, and belief in my potential have been instrumental to the successful completion of this thesis. Next, I would like to express my gratitude to Professor Van de Ville, Professor Micera, Professor Santoro and Dr Głowacki for accepting to be part of my jury committee and reviewing my PhD thesis.

Working at Campus Biotech has been an incredible opportunity with so many great minds and facilities in one place. A large portion of this thesis came from the Neural Microsystems Platform cleanroom, where my love for microfab started. Thank you to Anthony Guillet, Valérian Ruhaut, Michaël Stoeckel and Jeremy Laedermann for keeping the whole place running and always being responsive when there was an issue. No device would exist without this team and their willingness to help. I am deeply grateful to Anthony, the wizard behind the machines, for his unwavering technical support, his willingness to always lend an ear, and his patience in the face of my persistent requests. I would also like to extend my thanks to Jeremy for his understanding and patience in navigating my incessant requirements. A special shoutout to Michaël for keeping the ship on course and handling the chaos that is the cleanroom. I am grateful to the staff at the EPFL Center of MicroNanoTechnology (CMi), especially Jeoffrey and Oscar, as well as the numerous PhD students who created a welcoming and supportive environment. Thank you to the Pre-clinical Neuroscience Platform and the associated staff for letting me put my implants to the test and providing guidance and understanding.

I am deeply grateful to the LNE team, my first PhD home, for providing me with a supportive and stimulating environment where I could hone my research skills and grow as a scientist. Their guidance and mentorship played a pivotal role in shaping my early PhD journey, fostering my passion for scientific inquiry and equipping me with the necessary foundation to tackle the challenges that lay ahead. I'd like to mention my big sister Eleonora B for her understanding

i

Acknowledgements

ear, the chats from finance to psychology to microfab, have made me grow as a both a scientist and a person. Thank you to Adele for her kindness and motivating words, not only in the lab but also when we needed to sweat out the stress. A special mention to Franklin for the fun chats and letting me beat you at table tennis. This journey may not have even started if it wasn't for Marta and Golnaz who taught me what organic photovoltaics are and introduced me to fabricating these devices. Additional thanks to Sandrine, Jake, Elodie, Paola, Vivien and Naig for the fun and supportive environment you created. I am grateful for the opportunity to have mentored several talented students, particularly Martina and Justina, whose exceptional work and enthusiasm were a pleasure to guide.

To the amazing members of LSBI, I extend my sincere gratitude for their unwavering support and collaborative spirit, particuarly during the latter part of my PhD journey. Their open-door policy, shared knowledge, and enthusiasm for scientific discovery created a vibrant and inspiring environment. I am especially thankful for their flexibility and support during my transition into their group, which made me feel like a valued member of the team from day one. Thank you to Valentina, who was with me from the start of my lab experience at EPFL, for all the time spent in the cleanroom together and the only one understanding my references. To Eleonora M, thank you for your incredible positive spirit and advice ranging from relationships to lab nonsense. Kangling, the eternal presence in the lab, thank you for always being there to talk and make sure I'm alive when we work on weekends. Thank you to Emilie for all the help with the in vivo experiments and the calm guidance you've provided in writing this thesis. Special mention to Ivan for his incredible mind and problem-solving skills and willingness to always lend a hand and thank you to the rest of the Bollo buds; Outman, Yash, Matteo, Laurine, Victor, William, Scott and Emilio for keeping the lab a fun and lively place to be.

Thank you also to the CLSE team for their fun conversations when I was at EPFL for lunch and Prof Carlotta Guiducci for her mentoring and support.

Outside of the lab, I have to thank the Cossonay Cricket Club and Cricket Switzerland for letting me have fun and keep my sanity. In particular, I want to express my thanks to Jacqui, Liz, Anna, Natty, Andrew, Bharath, Sandra, Wan-Ching and Pari to name but a few people who have given me an outlet away from science. Thank you to the Leman Black Swans, for being an amazing group of footballers, and Fight District, an amazing group of fighters, who provided much-needed stress relief and fun throughout this journey.

I would like to finish by acknowledging those closest to me. To Giulia, your unwavering love, support, and belief in me have been an endless source of motivation and inspiration throughout this journey. Your creative soul and dedication to your own research have not only kept me focused but also reignited my curiosity. I am deeply grateful to have met you. Your incredible mind and gentle heart are qualities I admire every day. Thank you for being my teammate, partner and champion.

Lastly, I owe a huge debt of gratitude to my entire family for their unwavering love and support throughout my PhD journey, even from afar. Special mention to my grandma, cousins, aunts

and uncles who have always been there to listen and lend their advice. I'd like to express my deep gratitude to Amma and Appachchi, Eran and Tati, Lash and Anh and the best kids: Kiran, Luna and Tiago. Their unwavering belief in my abilities, their constant encouragement, and their patience have been a constant source of strength and inspiration. I am deeply grateful for their understanding, their sacrifices, and their unconditional love, which transcends distance. This thesis, every achievement I celebrate, and the person I have become are all reflections of them.

Geneva, May, 2024   D. I. M.

Abstract

Neural implants have demonstrated efficacy in implementing therapies for neurological disorders but their rigid design often leads to complications due to the mechanical mismatch with soft neural tissue. Current research focuses on developing flexible electrode interfaces to improve biocompatibility. However, the challenge of miniaturizing components such as wires and power sources remains. Wireless implants offer a solution by eliminating these bulky components thus reducing the overall size and invasiveness of the implant. This thesis explores the development and characterization of an organic near-infrared photovoltaic implant for wireless neural stimulation.

First, the work focuses on the fabrication and characterization of green-sensitive organic photovoltaic pixels. The chosen material, P3HT:PCBM, was selected for its established use in organic photovoltaics and its absorption spectrum in the visible range. A series of characterization techniques were employed to assess the performance of these pixels. These methods provided insights into the electrical properties, light-harvesting capabilities, and dynamic response of the photovoltaic pixels under various conditions.

Next, the work investigated the performance targets required to elicit cortical stimulation in the in vivo setting. Bipolar electrical stimulation of the mouse motor cortex served as a benchmark to establish the threshold charge and current values necessary for eliciting a motor response. This involved systematically varying the implant design to investigate electrode layout and stimulation parameters while monitoring muscle activity. The results from these in vivo experiments demonstrated that direction and distance were key in minimizing the current threshold amplitude to elicit a motor response. These findings served as a reference point for subsequent photovoltaic stimulation studies.

Finally, these guidelines were used to fabricate a near-infrared sensitive organic photovoltaic pixel capable of stimulating neural tissue. The material PDPP3T was chosen for its absorption range and combined with the acceptor molecule Y6. Extensive characterization of the pixels was performed to assess their electrical properties, light-harvesting capabilities, and stability. While promising results were obtained in terms of charge generation, a critical challenge arose regarding the stability of the pixels in aqueous environments. Various encapsulation techniques were explored to mitigate this issue with varying degrees of success. Preliminary in vivo experiments were conducted to evaluate the efficacy of the near-infrared photovoltaic

pixel for neural stimulation. However, no significant neural responses were observed in vivo. This outcome underscores the complexities associated with translation to in vivo devices and highlights the need for further refinement and optimization of the photovoltaic implant design.

Overall, by defining clear metrics and fabrication processes, this thesis makes promising headway in developing wireless neural implants powered by near-infrared light. It contributes knowledge on the design, optimization, and characterization of organic photovoltaic pixels, highlighting their potential for neural stimulation while acknowledging challenges in stability and in vivo translation. This work lays a solid foundation for future advancements in organic photovoltaic neural interfaces, offering new possibilities for minimally invasive neuromodulation therapies.

Résumé

Les implants neuronaux ont démontré leur efficacité dans le traitement des troubles neurologiques, mais leur conception rigide entraîne souvent des complications dues à l'incompatibilité avec les tissus neuronaux mous. La recherche actuelle se concentre sur le développement d'interfaces d'électrodes flexibles pour améliorer la biocompatibilité. Cependant, le défi de miniaturiser les composants supplémentaires tels que les fils et les sources d'énergie demeure. Les implants sans fil offrent une solution en éliminant ces composants encombrants, réduisant ainsi la taille globale et l'invasivité de l'implant. Cette thèse explore le développement et la caractérisation d'un implant photovoltaïque organique proche infrarouge pour la stimulation neuronale sans fil.

La première partie de ce travail s'est concentrée sur la fabrication et la caractérisation de pixels photovoltaïques organiques sensibles au vert. Le matériau choisi, P3HT :PCBM, a été sélectionné pour son utilisation établie dans les photovoltaïques organiques et son spectre d'absorption dans le visible. Une série de techniques de caractérisation a été employée pour évaluer la performance de ces pixels. Ces méthodes ont fourni des informations précieuses sur les propriétés électriques, les capacités de récolte de lumière et la réponse dynamique des pixels photovoltaïques dans diverses conditions.

Le chapitre suivant a examiné les objectifs de performance requis pour susciter une stimulation corticale in vivo. La stimulation électrique bipolaire du cortex moteur de la souris a servi de référence pour établir les valeurs de seuil de charge et de courant nécessaires pour provoquer une réponse motrice. Cela impliquait de faire varier systématiquement la conception de l'implant pour étudier la disposition des électrodes et les paramètres de stimulation tout en surveillant l'activité musculaire. Les résultats de ces expériences in vivo ont démontré que la direction et la distance étaient essentielles pour minimiser l'amplitude du seuil de courant pour provoquer une réponse motrice. Ces résultats ont servi de point de référence pour les études ultérieures de stimulation photovoltaïque.

Enfin, ces directives ont été utilisées pour fabriquer un pixel photovoltaïque organique sensible au proche infrarouge capable de stimuler le tissu neuronal. Le matériau PDPP3T a été choisi pour sa plage d'absorption et combiné avec la molécule acceptrice Y6. Une caractérisation approfondie des pixels a été effectuée pour évaluer leurs propriétés électriques, leurs capacités de récolte de lumière et leur stabilité. Bien que des résultats prometteurs aient été obtenus en

Résumé

termes de génération de charge, un défi critique est apparu concernant la stabilité des pixels dans les environnements aqueux. Diverses techniques d'encapsulation ont été explorées pour atténuer ce problème avec des degrés de succès variables. Des expériences préliminaires in vivo ont été menées pour évaluer l'efficacité du pixel photovoltaïque NIR pour la stimulation neuronale. Cependant, aucune réponse neuronale significative n'a été observée in vivo. Ce résultat souligne les complexités associées à la traduction en dispositifs in vivo et souligne la nécessité d'un raffinement et d'une optimisation supplémentaires de la conception de l'implant photovoltaïque.

Dans l'ensemble, en définissant des paramètres clairs et des processus de fabrication, cette thèse ouvre une voie prometteuse dans le développement d'implants neuronaux sans fil alimentés par la lumière proche infrarouge. Elle apporte des connaissances précieuses sur la conception, l'optimisation et la caractérisation des pixels photovoltaïques organiques, mettant en évidence leur potentiel pour la stimulation neuronale tout en reconnaissant les défis en matière de stabilité et de traduction in vivo. Ce travail jette les bases de futures avancées dans les interfaces neuronales photovoltaïques organiques, offrant de nouvelles possibilités pour des thérapies de neuromodulation peu invasives.

Contents

Contents

Contents

List of Figures

Acronyms

BHJ Bulk heterojunction.

DBS Deep brain stimulation.

EMG Electromyography.

ETL Electron transport layer.

FBR Foreign body reaction.

FDA U.S. Food and Drug Administration.

FF Fill factor.

HOMO Highest Occupied Molecular Orbital.

HTL Hole transport layer.

IrOx Iridium Oxide.

ITO Indium tin oxide.

J$_{sc}$ Short-circuit current density.

LED Light-emitting diode.

LUMO Lowest Unoccupied Molecular Orbital.

MEA Microelectrode array.

MoO$_3$ Molybdenum oxide.

MPP Maximum power point.

NFA Non-fullerene acceptor.

NiO Nickel oxide.

Acronyms

NIR Near-infrared.

OSC Organic solar cell.

OSTEmer Off-stoichiometry thiol-ene-epoxy polymer.

P3HT poly(3-hexylthiophene-2,5-diyl).

PaC Parylene C.

PC$_{61}$BM Phenyl-C61-butyric acid methyl ester.

PC$_{71}$BM Phenyl-C71-butyric acid methyl ester.

PCE Power conversion efficiency.

PDMS Polydimethylsiloxane.

PDPP3T Poly2,2'-[(2,5-bis(2-hexyldecyl)-3,6-dioxo-2,3,5,6-tetrahydropyrrolo[3,4-c]pyrrole-1,4-diyl)dithiophene]-5,5'-diyl-alt-thiophen-2,5-diyl.

PEDOT:PSS poly(3,4-ethylenedioxythiophene) polystyrene sulfonate.

PI Polyimide.

PV Photovoltaic.

R$_{sh}$ Shunt resistance.

R$_s$ Series resistance.

TiO$_2$ Titanium dioxide.

UV Ultraviolet.

V$_{oc}$ Open-circuit voltage.

ZnO Zinc oxide.

µECoG Micro-electrocorticographic array.

1 Introduction

Neural implants exist within a transformative era where neuroscience and engineering converge to unravel and influence the brain's complexities. These implants, capable of bridging the gap between biological systems and manmade devices, offer unprecedented opportunities to interface with the intricate circuitry of the nervous system. With the ability to both record and modulate neural signals, implants hold the potential to restore lost functions, alleviate the devastating symptoms of neurological disorders, and enhance our understanding of the brain. Neural implants represent an intersection of cutting-edge science and engineering, with profound implications for both clinical applications and fundamental neuroscience research.

1.1 The potential of neurostimulation

Neurostimulation, the targeted delivery of electrical signals to modulate neural activity, has emerged as a powerful therapeutic tool to address a wide range of neurological conditions (Figure 1.1). By interfacing with specific regions of the central and peripheral nervous system, neurostimulation can restore disrupted circuits[1], alleviate pain[2], and facilitate neural regeneration[3].

In particular, direct stimulation of the brain's cortex holds promise in treating conditions such as epilepsy[4], movement disorders[5], and chronic pain[2]. Techniques include deep brain stimulation (DBS)[1], where implanted electrodes deliver electrical stimulation to specific degenerated brain regions to assist abnormal motor functions, and cochlear implants[6] which are devices that convert sound waves into electrical signals to stimulate the auditory nerve, helping restore hearing in individuals with severe hearing loss. Spinal cord stimulation primarily targets the dorsal columns of the spinal cord and is a recognized treatment for intractable chronic pain[7]. Additionally, spinal cord stimulation has shown clear promise for applications in motor control for the regain of mobility and limb function following injury[8].

Interfacing with the peripheral nervous system involves delivering stimulation to nerves outside the brain and spinal cord. Applications include chronic pain management[9], treating

conditions such as complex regional pain syndrome and peripheral neuropathy. It is also being investigated for bladder[10] and bowel control[11] by modulating sacral nerves to improve function in individuals with neurological impairments. Through stimulation of the longest cranial nerve, vagus nerve stimulation holds the potential to treat a variety of neurological diseases[12] and is approved by the FDA.
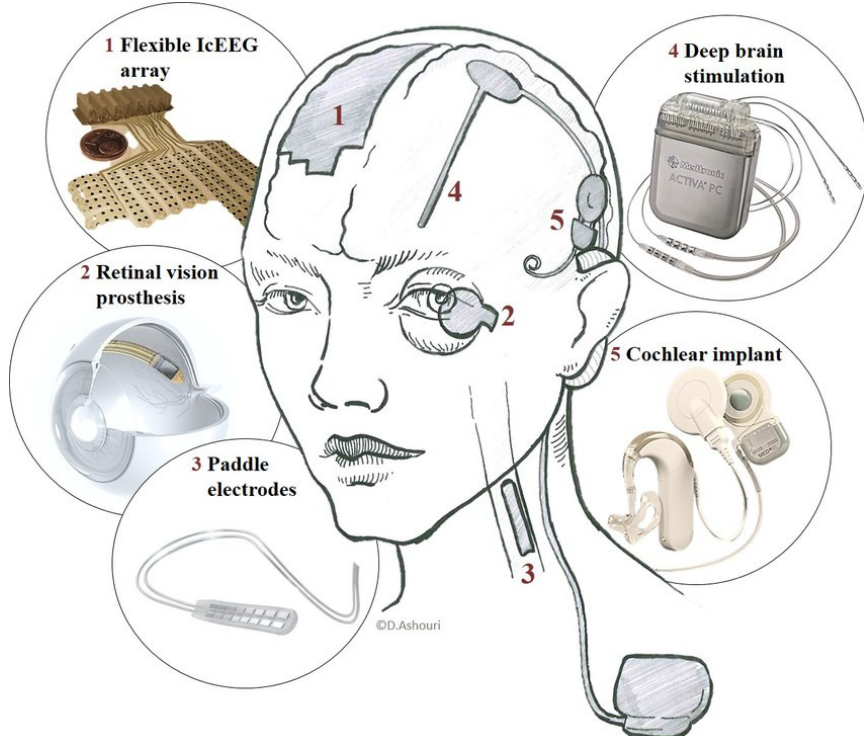
Figure 1.1: **Examples of neurostimulation devices** Neurostimulation devices that have been implanted in humans for clinical purposes. Each device has a form of implanted pulse generator as depicted in the bottom, grey drawing. Adapted from Erhardt *et al.*[13]

All of these therapeutic strategies rely on the same traditional architecture of the neural implant. They generally have a passive electrode array, which is placed close to the target neural tissue, and connected to a set of electronic components, including a stimulator, batteries, and control electronics[14] (Figure 1.1). The control unit, powered by an implanted battery, delivers electrical charge to the electrodes that then stimulates the adjacent area as neural tissue is electrically excitable. This thesis focuses on a wireless strategy, using photovoltaics, to generate and deliver electrical stimulation. Thus, it would replace the need for the implanted control unit and battery for all applications to address the challenges mentioned below.

1.2 Challenges for neural implants

While neurostimulation offers significant clinical benefits, challenges remain. The biological environment is particularly harsh with electrolytic tissues[15], biofouling[16], and mechanical

stresses[17]. In addition to this, material failures also limit the lifespan of these devices[18]. A critical challenge arising from these factors is the foreign body reaction (FBR, Figure 1.2) . The body's immune system recognizes the implant as a foreign intrusion, triggering a cascade of responses aimed at isolating and potentially rejecting the device.

The FBR unfolds in a series of stages[19]. Initially, proteins from the surrounding tissue rapidly adsorb onto the implant surface. This triggers an acute inflammatory response, with the recruitment of neutrophils and macrophages to the implant site. Macrophages attempt to phagocytose the implant, but its size often renders this impossible, leading to a state of "frustrated phagocytosis". This sustained activation of immune cells results in the release of inflammatory cytokines and potentially damaging oxidative species, causing local tissue irritation and damage[20].

Over time, the FBR transitions into a chronic phase[19]. Macrophages may fuse to form foreign body giant cells and a dense fibrotic capsule composed of collagen and fibroblasts develops around the implant. This capsule serves to isolate the foreign material from the rest of the body, significantly hindering the neural implant's ability to communicate effectively with the surrounding neurons. Signal transmission can be degraded, stimulation thresholds increase, and the overall effectiveness of the implant declines.

The severity and progression of the FBR depends on several factors. One of these is the material properties[21] where the mechanical stiffness, surface chemistry and topography tailor the immune system response. Softer, more flexible materials tend to elicit milder FBR. This flexibility comes from the combination of material type and geometry, with even stiff materials becoming flexible at very thin scales. A smaller device, hence with less material, can cause less damage to the surrounding tissue[20]. Additionally, the site of implantation heavily influences the FBR with penetrating electrodes naturally causing more tissue damage, and thus more FBR, while electrodes on the surface of the tissue minimize this invasiveness. Strategies to mitigate the FBR lie at the forefront of neural implant research.
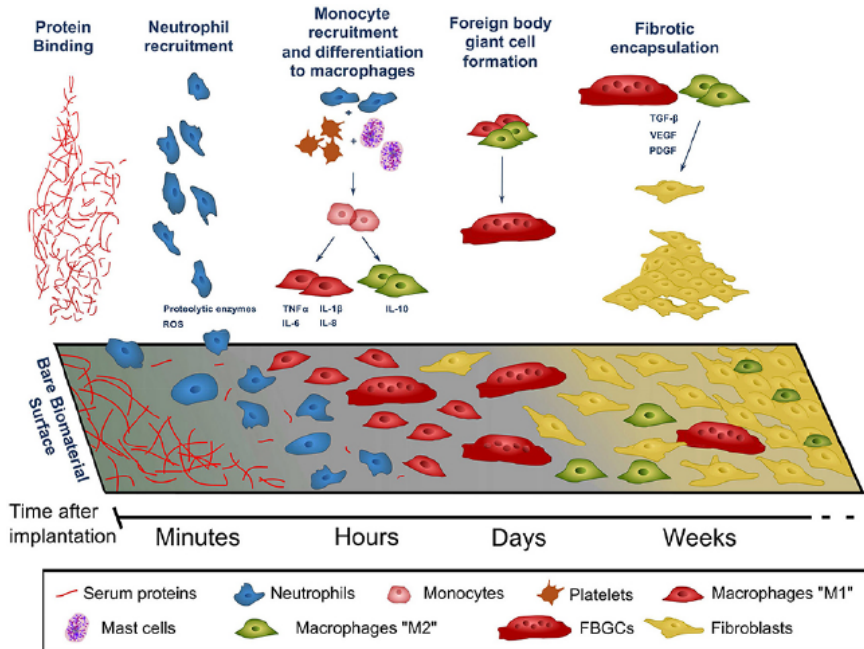
Figure 1.2: **The foreign body reaction** The progression of the foreign body reaction over time with different cell infiltrations leading to the fibrotic scar. Adapted from Carnicer-Lombarte *et al.*[20]

1.3 Avenues to overcome FBR

Overcoming the hurdle of the foreign body reaction is critical for realizing the long-term potential of neurostimulation. Commercially available neural interfaces often rely on metals or inorganic semiconductors such as platinum, titanium, stainless steel, gold and silicon. While these materials have exceptional conductivity, their high Young's moduli, meaning a highly stiff material, creates a stark mismatch with the soft neural tissue[21]. To bridge this gap, extensive research has focused on making stiff electronics more flexible and stretchable.

One popular approach involves replacing traditional substrates with polymers such as poly-imide (PI), Parylene C (PaC), or polydimethylsiloxane (PDMS) to support microfabricated probes[22]. These polymers can also serve packaging and insulation functions. Further exploration utilizes organic conductors like poly(3,4-ethylenedioxythiophene) polystyrene sulfonate (PEDOT:PSS) in place of metals[23]. While polymeric materials have demonstrated a milder FBR compared to their stiffer counterparts[20], neural implants made of these materials still exhibit a stiffness 3 to 6 orders of magnitude higher than brain tissue (Figure 1.3).

While material stiffness and flexibility are crucial considerations, another promising avenue to mitigate the FBR lies in surface modification and coatings[24]. By altering the surface properties of the implant, it is possible to influence its interaction with the surrounding biological environment. Hydrophilic coatings, for instance, can reduce protein adsorption and immune

cell adhesion, minimizing the initial inflammatory response. Zwitterionic polymers, known for their biomimetic properties, can further enhance biocompatibility by repelling proteins and cells through a hydration layer[25]. Additionally, nanotopographical modifications can be employed to create surface features that promote cell adhesion and integration, potentially facilitating a more seamless interface between the implant and the surrounding tissue[26]. Recently, the paradigm has begun shifting towards hydrogels due to their exceptional similarity to biological tissues and the ability to tailor their mechanical properties and chemical[27].

However, solely re-engineering materials to achieve a perfect match of the interface with the nervous system might not suffice. The remainder of the implanted system, with its bulky battery and control unit on the order of cubic centimetres, enhances the FBR when in contact with neural tissue due to their volume and mechanical properties. In the context of neuromodulation, a larger fibrotic capsule results in higher stimulation thresholds, lower spatial resolution and excess damage to the surrounding neural tissue.

To avoid the contact of bulky components with the tissue, they can be placed away from the interfacing electrodes resulting in connecting cables. The introduction of wires leads to more failure points, the possible introduction of noise and a higher risk of infection. Wireless neural implants offer a solution by inherently reducing the number of implanted components. Organic photovoltaics, in particular, are promising as they can be made into thin, flexible devices to minimize the FBR.
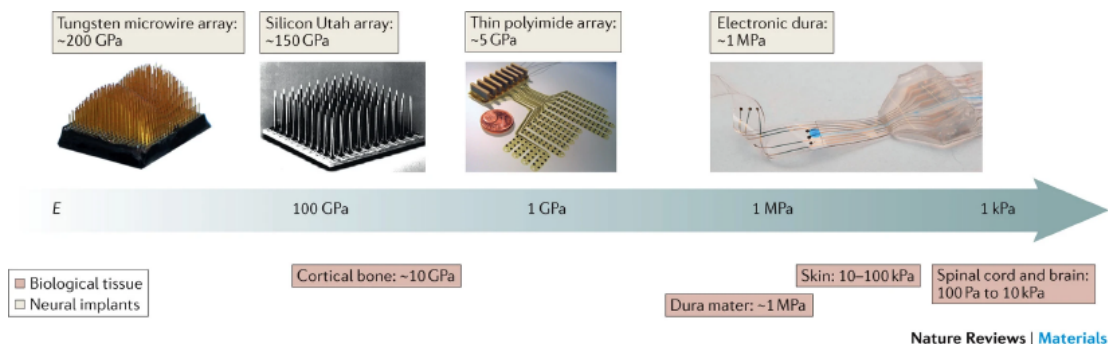
Figure 1.3: **Young's modulus of typical neural implants and biological tissue** Image from Lacour *et al.*[21]

1.4   Wireless neural implants

Wireless communication permeates modern society and is well-established in everyday life with consumer electronics. By eliminating the need for bulky electronic components and tethering cables, wireless implants pave the way for minimally invasive, flexible devices that reduce the risk of complications and better integrate with delicate neural tissue. This streamlined approach minimizes surgical intervention and lowers the potential for failure at component interfaces. Crucially, the reduced invasiveness and gentler interaction with

biological tissue hold promise for decreasing the severity of the FBR. Furthermore, wireless designs open possibilities for smaller, more conformal implants that unlock access to diverse regions of the nervous system.

There are numerous avenues of wireless stimulation strategies all of which represent active research in the neuroengineering space. These make use of magnetic, ultrasound or electromagnetic signals to transfer power.

1.4.1   Electromagnetic fields

By far, the most explored method of wireless power transfer is through inductive or capacitive coupling using electromagnetic waves[28]. Inductive and capacitive coupling offer distinct mechanisms for wireless power transfer vital to miniaturized neural implants. Inductive coupling, the most widely explored technique, relies on a pair of coils – a transmitter coil outside the body and a smaller receiver coil implanted near the neural device. Alternating current in the transmitter coil generates a magnetic field, which in turn induces an electrical current in the receiver coil, wirelessly powering the implant. Key advantages of this method include established technology, relatively high efficiency over short distances, and good biocompatibility. However, efficiency drops significantly with increased distance between the coils and heating of coils should be considered at higher power levels.

Capacitive coupling is an alternative method utilizing a pair of electrodes instead of coils. An external transmitter electrode applies an alternating electric field, inducing a current in a paired receiver electrode implanted near the device. Capacitive coupling boasts potential advantages, including the possibility of smaller implant designs and the ability to transmit through insulating materials like bone. However, this technique generally suffers from lower power transfer efficiency than inductive coupling. Furthermore, its effectiveness depends heavily on the alignment and distance between the electrodes, posing challenges for practical implementation.

Both inductive and capacitive coupling are actively researched to optimize power delivery to neural implants. Advances in materials science, circuit design, and miniaturization aim to improve efficiency, reduce implant size, and address safety concerns. The ideal choice for a specific neural implant depends on factors such as the target location, required power levels, and design constraints. The wireless power transfer to neurostimulation requires a transducer component, which remains stiff and potentially bulky with these coupling techniques.

1.4.2   Ultrasound

Ultrasound stimulation is available through both non-invasive methods[29] or implanted piezoelectric components[30]. While the precise non-invasive mechanisms remain under investigation, ultrasound is thought to stimulate neural tissue through a combination of mechanical, thermal, and cavitation-based effects. Focused ultrasound beams can exert mechanical forces

on cell membranes, potentially altering ion channel function and directly influencing neuronal excitability. Localized heating or the formation and collapse of microbubbles due to ultrasound exposure can further modulate neural activity[31]. These effects make ultrasound a promising tool for non-invasive neurostimulation with the potential for high spatial precision. However, incomplete understanding of these mechanisms, temporal limitations, the challenge of skull penetration, and the need for further technological development pose hurdles that ongoing research aims to address.

Piezoelectric materials, which generate an electrical charge in response to mechanical stress, offer a promising avenue for wireless neurostimulation[30]. By using focused ultrasound to remotely induce vibrations in a piezoelectric implant, it is possible to generate localized electrical currents sufficient to stimulate neural tissue. Ongoing research is focused on optimizing piezoelectric materials, ultrasound parameters, and device designs to achieve precise, targeted, and safe neurostimulation for various therapeutic applications.

1.4.3 Magnetic fields

Magnetic neurostimulation offers a distinct approach to influencing neural activity using time-varying magnetic fields to induce electrical currents within tissues. Transcranial magnetic stimulation utilizes a coil near the scalp to generate magnetic field pulses that penetrate the skull, inducing localized electric fields in the brain. Focused magnetic stimulation offers improved spatial precision[32]. A key advantage of magnetic stimulation is that magnetic fields readily pass through biological tissues allowing for deeper tissue penetration compared to some other non-invasive techniques. Magnetosensitive materials, paired with piezoelectrics, offer another way of stimulating tissue wirelessly by utilising the material properties of these two classes of devices however still require large magnetic fields and suffer from alignment issues for the time being[33].

1.4.4 Electromagnetic fields - light

Photovoltaic (PV) technology offers a novel approach to wireless power and stimulation for neural implants. Leveraging established principles from solar energy conversion, PV implants utilize light to generate the electrical current needed to power the device. Similar to how solar panels harvest energy from sunlight, these implants would employ miniaturized PV cells to convert light into electricity.

One exciting application of PV implants lies in prosthetic vision. The mechanism of photo-transduction in these devices mimics the natural function of photoreceptors in the human eye, potentially offering a more biomimetic approach to vision restoration[34].

Optogenetics, a technique that uses light to modulate neuronal activity, has gained popularity due to its high temporal resolution and ability to precisely target specific neural circuits[35]. However, traditional optogenetic approaches often rely on tethered connections or implanted

optical fibres to deliver light, hindering long-term usability. PV implants overcome this to offer stimulation using light without genetic modification of the issue, relatively avoided in modern neuroengineering for human applications for ethical reasons.

A key advantage of PV implants lies in their potential for miniaturization. Compared to radio frequency and inductive coupling methods, PV devices can be miniaturized to submillimeter scales, offering significant advantages for implant size and biocompatibility. Additionally, biological tissues exhibit high light transmittance in the near infrared (NIR) region[36]. Therefore, PV implants designed to be sensitive to wavelengths within the NIR range would maximize light penetration through tissues. Given these advantages, photovoltaics were chosen as the mechanism to deliver wireless neural implants for this thesis.

1.5 Theory of photovoltaic cells and applications in neurostimulation

Photovoltaics refers to the conversion of light energy into electrical current through the excitation of electrons within a material[37]. PV materials are typically semiconductors, exhibiting electrical conductivity that falls between that of metals and insulators.

The allure of harnessing a clean, abundant source like sunlight for continuous electricity generation has fueled significant research and development efforts in solar cell technology. Across the globe, researchers are actively exploring novel materials and fabrication techniques with a dual focus on maximizing conversion efficiency and minimizing production costs. The National Renewable Energy Lab efficiency chart (Figure 1.4) illustrates the remarkable advancements in record efficiencies achieved across various PV technologies over the past five decades. Notably, solar cells are categorized into distinct "generations"[38]. The first generation encompasses thick-film, wafer-based technologies utilizing monocrystalline and polycrystalline silicon (Si) as well as gallium arsenide (GaAs). Thin-film cells fabricated from materials such as amorphous silicon (a-Si), microcrystalline silicon (μc-Si), cadmium telluride (CdTe), cadmium sulphide (CdS), and copper indium gallium selenide (CIGS) constitute the second generation. Currently, crystalline silicon solar panels dominate the market due to their superior conversion efficiency and cost-effectiveness[39]. The third generation encompasses a diverse range of emerging PV technologies with promising potential, even if they are currently less competitive due to limitations in cost or efficiency. These technologies include cells based on perovskites, organic conducting polymers, dye-sensitized solar cells (DSSCs), and quantum dots. Notably, organic conducting polymers offer significant advantages in terms of cost and fabrication energy requirements and can be produced in flexible film formats.

Organic solar cells (OSCs), while generally exhibiting lower power conversion efficiencies compared to traditional silicon-based or emerging perovskite solar cells, hold several potential advantages that make them an attractive area of research. Currently, OSC efficiencies often reach the 15-18% range under laboratory conditions. In contrast, established inorganic solar

cell technologies like crystalline silicon routinely exceed 20% efficiency, with some experimental cells demonstrating efficiencies above 40%. Despite this gap, organic materials offer unique benefits such as mechanical flexibility and processability, opening possibilities for applications where rigid silicon panels are unsuitable. Their lower fabrication costs and potential for solution-based processing techniques hint at the possibility of cost-effective, large-scale production using roll-to-roll methods[40]. The tunability of organic materials through molecular design provides a pathway for further optimizing efficiency, stability, and tailoring properties for niche applications. Biocompatibility, flexibility and stretchability (upon specific manufacturing), high absorption coefficient in thin films, and consequently lightweight are among the main advantages of using organic technology in bioelectronic interfaces. For these reasons, this thesis will focus on neurostimulation using organic photovoltaic devices.
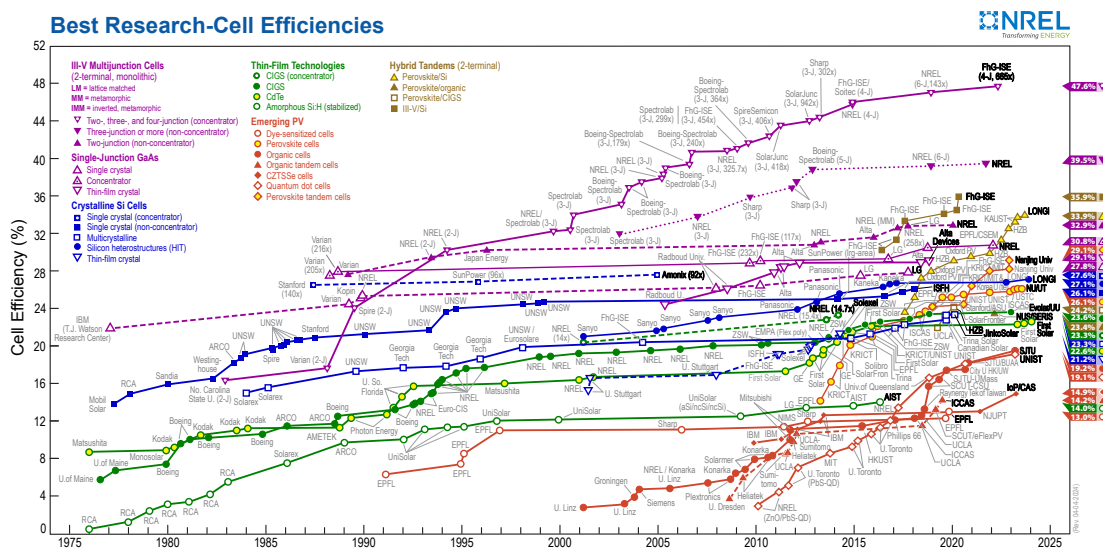
Figure 1.4: **National Renewable Energy Lab Efficiency Chart** Efficiencies of different types of solar cells assessed by the standard laboratory. Emerging technologies are depicted in red with organic cells being red, filled circles. Adapted from the NREL website[41]

1.5.1 Inorganic solar cells

While this thesis focuses on organic PVs, a conceptual understanding on inorganic semiconductor physics allows a more natural transition into organic solar cells. Understanding the current generation mechanism in inorganic solar cells necessitates a brief examination of p-n junctions.

The electrical conductivity of materials is fundamentally governed by the arrangement of their electron energy levels, specifically the valence and conduction bands. The valence band refers to the highest range of energy levels where electrons typically reside within the material. In contrast, the conduction band is the range of vacant electronic states where free electrons, capable of conducting electrical current, reside. In metals, the valence and

conduction bands overlap, providing a continuous supply of free electrons for conduction. Conversely, in insulators, a large energy gap separates the two bands, hindering electron transitions to the conduction band and resulting in low conductivity. Semiconductors occupy an intermediate position, possessing a smaller energy gap known as the bandgap. This bandgap allows electrons in the valence band to be excited into the conduction band with the absorption of energy (e.g., thermal energy or light), leading to a measurable degree of electrical conductivity.

Intrinsic semiconductors, in their pure form, possess a limited number of charge carriers for electrical conduction. These consist of both electrons in the conduction band and holes (positively charged vacancies) in the valence band (Figure 1.5A). The electron density in the conduction band equals the hole density in the valence band, known as the intrinsic carrier density. Doping, the intentional introduction of impurities into a semiconductor, significantly alters its conductivity and carrier densities. P-type doping introduces impurities with fewer valence electrons (such as boron). This creates an abundance of holes, significantly increasing hole density and making them the majority carriers. Conversely, n-type doping introduces impurities with extra valence electrons (such as phosphorus). These excess electrons readily enter the conduction band, making electrons the majority carriers and significantly increasing electron density.

When a p-type and n-type semiconductor are brought into contact, a p-n junction forms (Figure 1.5B). At this interface, the abundance of holes in the p-type region and electrons in the n-type region creates a strong concentration gradient. This drives a process called diffusion – the natural movement of charge carriers from regions of high concentration to low concentration. Consequently, holes diffuse from the p-side to the n-side, and electrons diffuse in the opposite direction. As these charge carriers cross the junction, they leave behind positively charged ionized dopant atoms in the n-region and negatively charged ionized dopant atoms in the p-region. This charge separation creates a built-in electric field within the depletion layer, a region located at the interface between the p-type and n-type materials. The electric field opposes further diffusion, establishing a competing process called drift. Drift current refers to the movement of charge carriers driven by this electric field. At equilibrium, the diffusion current and drift current balance out, maintaining a stable depletion layer where mobile charge carrier concentrations are significantly reduced.

Applying an external voltage across a p-n junction, known as biasing, significantly alters its behaviour. In forward bias, the positive terminal of the external voltage source is connected to the p-type side and the negative terminal to the n-type side. This external voltage reduces the built-in potential barrier within the depletion layer, narrowing its width. When the forward bias exceeds a certain threshold, it overcomes the built-in potential, allowing a significant flow of charge carriers across the junction. This results in a large forward current through the diode. Conversely, in reverse bias, the positive terminal of the external voltage source is connected to the n-type side and the negative terminal to the p-type side. This increases the built-in potential barrier and widens the depletion layer. Under reverse bias, only a very small leakage

current flows due to minority carriers, making the diode effectively non-conductive.

An inorganic solar cell is fundamentally a large-area p-n junction diode optimized for light absorption and charge collection[42]. When a photon with sufficient energy strikes the semiconductor material within the depletion layer or nearby regions, it can excite an electron from the valence band into the conduction band. This process generates a free electron and leaves behind a hole, creating an electron-hole pair. The built-in electric field of the p-n junction separates these charge carriers, driving electrons towards the n-type side and holes towards the p-type side. If these charge carriers reach the external contacts before recombining, they can flow through an external circuit, generating electrical current (Figure 1.5C). This is the fundamental mechanism of PV energy conversion in inorganic solar cells.
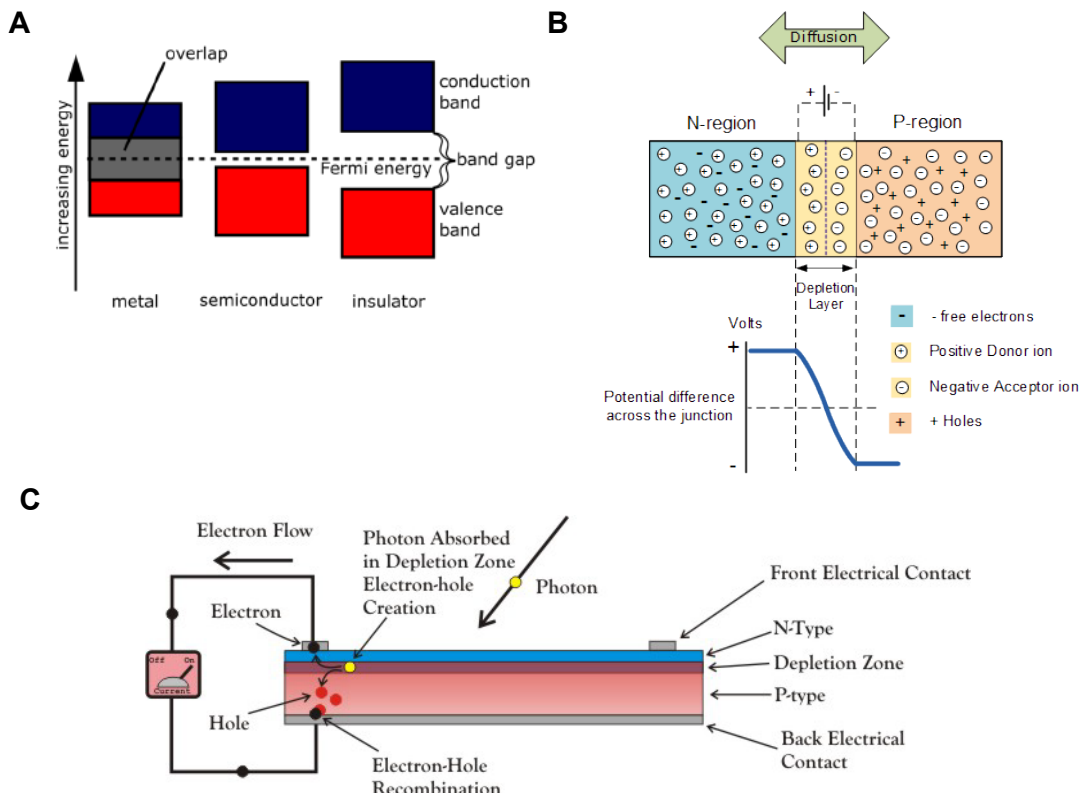
Figure 1.5: **Basic function of inorganic solar cells** A) The valence (red) and conduction (blue) bands of metals, semiconductors and insulating materials with the Fermi level and band gap (E_g) indicated. Adapted from Wikimedia[43] B) A p-n junction at equilibrium indicating the depletion region where charges have diffused into the adjacent material. Across this junction, there is a built-in electric field preventing further diffusion. Adapted from Images SI[44] C) Principle of a solar cell. Adapted from Electronics Tutorials[45]

1.5.2   Inorganic photovoltaic implants for neurostimulation

Pioneering work in neurostimulation with photoactive materials began with inorganic materials, leveraging their established presence in the solar cell industry. As the eye naturally converts light into neural signals, retinal implants were one of the first applications for such a technology. This was principally posited by the Palanker's group[46] where a silicon-based subretinal design with 2500 pixels/mm^2 was deemed feasible. This was continued with recent advancements in this PRIMA technology having opened doors for retinal stimulation, aiming to restore vision in those with damaged photoreceptors. The inorganic, silicon photovoltaic implants have been placed directly beneath the retina, to stimulate surviving retinal neurons, offering a potential approach for artificial vision[47]. This technology has shown a high degree of visual acuity in rats[48] and shown safety and stability in patients[34] with the 30 μm-thick array of pixels.

Expansion beyond the retina requires particular care into the way in which light is introduced to the photovoltaic device and whether the implant can generate sufficient charge for stimulation. This was simulated and modelled initially to determine the limits, dimensions and materials for use in cortical and spinal cord stimulation[49]. Critically, the output voltage of the device which could be tailored by the number of diodes in series had to be sufficient for stimulation however not exceed the water window to avoid electrolysis. Abdo and Sahin[49] determined that GaAs-based implants, sensitive to near-infrared light, at submillimeter scales were theoretically capable of neuromodulation. This was put into practise through spinal cord stimulation[50] to elicit muscle activation as low light intensities. These devices were comprised of a tandem AlGaAs/GaAs device with a final thickness of approximately 150 μm. This technology was expanded to have device addressability based on the wavelength of the input light through passive optical blocks[51].

Novel inorganic photoactive devices have also been actively explored, with research demonstrating the use of silicon nanowires modified for enhanced photosensitivity to modulate neuronal activity[52] and the use of tailored upconverting nanoparticles that can convert deep-tissue penetrating near-infrared light into localized stimulation signals for neurons[53].

1.5.3   Organic solar cells

Unlike inorganic solar cells, organic solar cells are based on molecules rather than crystalline semiconductors. This allows for solution processing which, along with their high absorption coefficient, mean that organic photoactive layers are in the tens of nanometers[54]. Instead of the traditional valence and conduction band model, the energy levels in organic materials are described in terms of the Highest Occupied Molecular Orbital (HOMO) and the Lowest Unoccupied Molecular Orbital (LUMO)[55] (Figure 1.6B). The HOMO can be thought of as analogous to the valence band in inorganic semiconductors, representing the highest energy level where electrons typically reside. Analogously, the LUMO is comparable to the conduction band, representing the lowest available energy state for an excited electron. The difference in

energy between the HOMO and LUMO in an organic material determines its bandgap.

In organic PVs, the absorption of a photon with an energy greater than the E_g either by the donor leads to the generation of an exciton. This excitation forms a tightly bound, neutral quasiparticle called an exciton, where the electron and hole remain electrostatically attracted. Unlike inorganic solar cells, this does not directly create free charge carriers. For current generation, the exciton must first diffuse a short distance to a donor-acceptor interface. There, the energy offset between the materials helps dissociate the exciton into free charge carriers (electrons and holes). The built-in electric field then drives the transport of these free carriers to their respective electrodes via drift and diffusion processes. Finally, the collection of free carriers at the electrodes allows current to flow through an external circuit. The efficiency of organic solar cells depends highly on the interplay between exciton diffusion length and the intricate nanoscale structure of donor-acceptor interfaces.

The limited exciton diffusion length in organic semiconductors (typically only a few nanometers) initially posed a significant challenge for efficient organic solar cells. Early designs often used a simple bilayer structure, where a donor layer was directly adjacent to an acceptor layer. However, only excitons generated very close to the donor-acceptor interface had a high probability of reaching it before decaying. To address this limitation, the bulk heterojunction (BHJ) concept was introduced[55]. In a BHJ structure, the donor and acceptor materials are intimately intermixed on a nanoscale, creating a vast network of donor-acceptor interfaces throughout the active layer (Figure 1.6A). This design dramatically increases the probability of excitons finding an interface before recombination, significantly boosting the efficiency of organic solar cells.

1.5.4   Organic solar cells - materials and design

A key distinction between organic and inorganic semiconductors lies in their charge carrier mobilities. Inorganic materials often exhibit mobilities several orders of magnitude higher than their organic counterparts[56]. This disparity in mobility can hinder efficient charge separation and collection within organic solar cells. To overcome this limitation, organic solar cell designs often incorporate buffer layers called hole transport layers (HTLs) and electron transport layers (ETLs) (Figure 1.6B). These layers are carefully chosen organic or inorganic materials with superior mobility for either holes or electrons, respectively. By positioning HTLs and ETLs between the electrodes and the active layer, they create a favourable energy level gradient that guides charge carriers towards their respective electrodes[57]. This not only improves charge separation at the donor-acceptor interface but also facilitates their efficient transport to the collecting electrodes, ultimately enhancing the overall power conversion efficiency of organic solar cells.

The positioning of the ETL and HTL within the device architecture plays a critical role in defining whether an OSC is classified as conventional or inverted (Figure 1.6C). In a conventional structure, the HTL is deposited onto the transparent anode, followed by the active layer, and

finally the ETL and the cathode. Conversely, in an inverted structure, the stacking order is reversed. The ETL is deposited first on the transparent anode, followed by the active layer, the HTL, and a top metal cathode. In both structures, the ETL and HTL function to improve charge extraction and prevent recombination, but their specific placement in relation to the electrodes dictates the polarity of the final device.

Organic solar cell research involves a wide array of materials, each with specific properties that determine device performance. Among the most extensively studied active layer materials is the combination of poly(3-hexylthiophene) (P3HT) as the donor and [6,6]-Phenyl C61 butyric acid methyl ester ($PC_{61}BM$) as the acceptor. These materials have historically served as a benchmark in the field due to their relatively good performance and ease of processing[58]. PEDOT:PSS is commonly employed as a hole transport layer (HTL), particularly in conventional architectures. Beyond organic transport layers, metal oxides such as zinc oxide (ZnO) or titanium dioxide (TiO_2) can serve as ETLs, while nickel oxide (NiO) or molybdenum trioxide (MoO_3) can function as HTLs. Metal oxides often offer advantages in terms of stability and processability.

Indium tin oxide (ITO) is a frequently used transparent conductive material. Inverted structures employing ITO as the bottom electrode often demonstrate improved stability. This is partially due to the acidic nature of PEDOT:PSS, which can degrade the ITO layer in conventional architectures over time. The inverted structure shields the ITO from this direct contact, enhancing device longevity.

The choice of top contact material differs between conventional and inverted structures to ensure proper charge extraction. Conventional cells often use low work function metals like aluminium or calcium as the top cathode. Inverted cells, conversely, require high work function materials as the top anode, such as silver or gold. While low work function metals are prone to oxidation and degradation, the inverted geometry with high work function metals are more resistant to the environment, contributing to improved device stability.
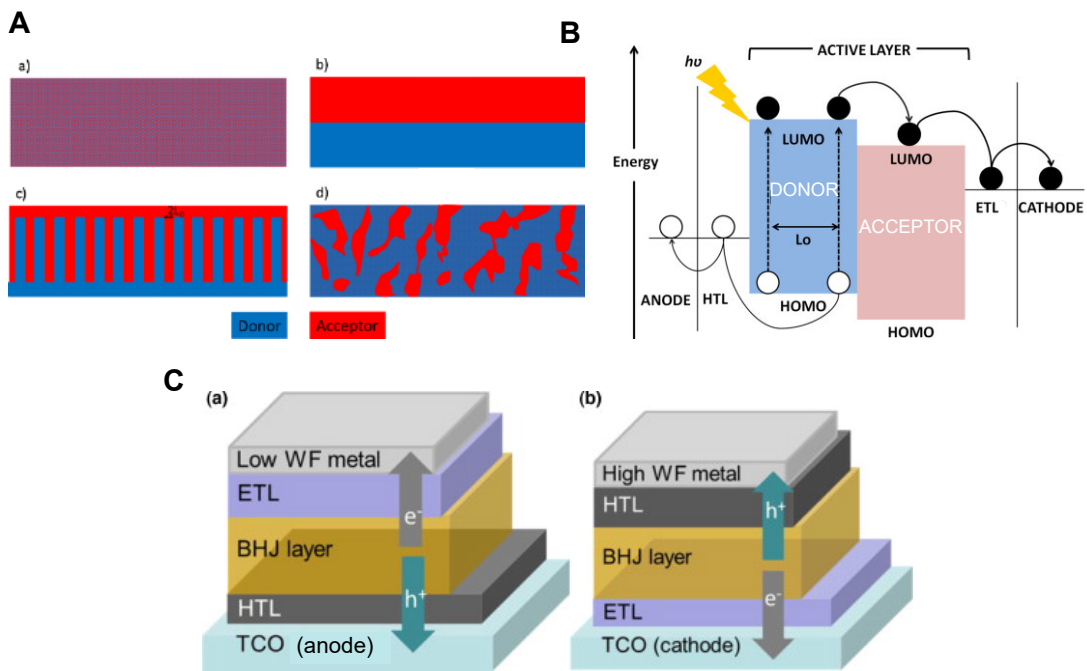
Figure 1.6: **Organic solar cell structure** A) Cross-section of organic donor-acceptor layers. a) Nano-scale mixing, below the diffusion limit (L_D) allowing charges to be collected from the acceptor layer however contact is not possible. b) Bilayer arrangement with minimal surface area for exciton dissociation d) Ideal arrangement of a bulk heterojunction of the donor and acceptor. d) Typical morphology in processed bulk heterojunction films. Adapted from Scharber *et al*[59]. B) Energy band diagram of an organic solar cell showing the steps from photon absorption, exciton formation, charge dissociation, charge collection and transport. Adapted from Paula *et al*[60]. C) Conventional (left) and inverted (right) solar cell arrangement with the flow of charges and top contact material. Adapted from Lai *et al*[61]

1.5.5 Application of organic semiconductors for neuromodulation

Adapted from Medagoda, Danashi Imani, and Diego Ghezzi. "Organic semiconductors for light-mediated neuromodulation." Communications Materials 2.1 (2021): 111.

Organic photovoltaic materials were pioneered for stimulation of cultured neurons in 2011 using a bulk heterojunction, composed of poly(3-hexylthiophene-2,5-diyl) (P3HT)and [6,6]-Phenyl-C61-butyric acid methyl ester ($PC_{60}BM$), paired to an indium tin oxide (ITO) conductor (ITO/P3HT:$PC_{60}BM$)[62]. A few years later, two studies showed the potential of organic semiconductors in retinal stimulation for artificial vision[63,64]. The effort culminated in the demonstration of recovery of visual functions in a rat animal model of blindness with an organic device composed of a silk substrate, a PEDOT:PSS conductor and a P3HT semiconductor layer[65]. Since then, a large number of studies have demonstrated the potential of organic bioelectronics for the photovoltaic stimulation of the retina or neuromodulation in general.

Several conductor/semiconductor interfaces have been explored for neuronal stimulation

in-vitro. Rand et al.[66] proposed a p-n bilayer structure composed of two organic pigments, phthalocyanine (H2Pc, p-type) and N,N'-dimethyl perylene-3,4:9,10-tetracarboxylic diimide (PTCDI, n-type), layered on top of a chromium/gold anode. Results showed the direct activation of cultured primary neurons and retinal ganglion cells in an embryonic chick retina with short pulses in the deep red via a capacitive coupling. Concurrently, Nizamoglu et al.[67–70] are investigating other device structures with nanomaterials to maximise the stimulation efficiency of the conductor/semiconductor interface. Han et al.[67] introduced a hybrid organic/inorganic structure exploiting a thin film of aluminium antimonide (AlSb) nanocrystals coated on top of a pristine P3HT film as the hole transport layer and interface layer to cultured neurons. The device structure had four layers: ITO as bottom conductor, zinc oxide (ZnO) as electron transport layer, P3HT and AlSb. Photocurrent measurements upon 20 ms blue light illumination showed strong capacitive currents at low irradiance leading to action potential generation in cultured neurons up to 20 Hz of repetition rate. Karatum et al.[68] showed that interfaces based on InP/ZnS core/shell quantum dots (QDs) generated Faradaic currents leading to either membrane depolarisation and action potential generation or membrane hyperpolarisation depending on the device structure (ITO/titanium oxide/QD for depolarisation and ITO/QD/ZnO for hyperpolarisation). In a second report[69], authors further explore QDs for capacitive current generation at the material/electrolyte interface by exploiting an heterojunction composed of InP/ZnO/ZnS core/shell/shell QDs as the electron donor and PC60BM as the electron acceptor layered over a ITO/ZnO conductor. Last, Srivastava et al.[70] proposed a high open-circuit voltage bulk heterojunction composed of poly[4,8-bis(5-(2-ethylhexyl)thiophen-2-yl)benzo[1,2-b;4,5-b']dithiophene-2,6-diyl-alt-(4-(2-ethylhexyl)-3-fluorothieno[3,4-b]thiophene-)-2-carboxylate-2-6-diyl)] (PTB7-Th) blended with [6,6]-Phenyl-C71-butyric acid methyl ester (PC71BM) coated over a ITO/ZnO conductor to elicit spikes in cultured primary neurons.

Ghezzi et al.[71–73] developed a photovoltaic wide-field spherical array for retinal stimulation, embedding several thousands of photovoltaic pixels composed of a P3HT:PC60BM layered between a polymeric anode (PEDOT:PSS) and an inorganic cathode (titanium/titanium nitride, Ti/TiN) for efficient capacitive stimulation (conductor/semiconductor/conductor interface). Results demonstrated efficient network-mediated stimulation of retinal ganglion cells with very high spatial resolution equivalent to the pitch of the photovoltaic pixels embedded in the array[73]. The same device was proposed exploiting a different electron donor material, the poly[2,6-(4,4-bis-(2-ethylhexyl)-4H-cyclopenta[2,1-b;3,4-b']dithiophene)-alt-4,7(2,1,3-benzothiadiazole)] (PCPDTBT) blended with the PC60BM electron acceptor (PCPDTBT:PC60BM) to provide sensitivity in the near infrared spectrum[74], crucial for applications in retinal stimulation.

Besides capacitive and Faradaic neuronal stimulation, heat generation can be exploited for neuromodulation. Martino et al.[75] showed that a thin P3HT film, or its bulk heterojunction with PC60BM, layered on an insulating glass substrate led to membrane depolarisation on Human Embryonic Kidney (HEK-293) cells, grown on top, mediated by heat transfer for sufficient long and intense exposure. Membrane depolarisation was associated with a

temperature-dependent change in the membrane capacitance. Feyen et al.[76] extended this approach reporting that prolonged illumination (e.g. 150 ms or longer) of the P3HT film led to membrane hyperpolarization and silencing of neuronal firing in cultured primary neurons, epileptic hippocampal slices and explanted blind retinas. The ability to silence neuronal firing might find applications in several conditions, such as inhibition of nerve activity for pain relief[77] or silencing epileptiform activity. While in these reports, the photothermal modulation of the cell membrane was independent of TRPV channels, Lodola et al.[78] showed that the same interface could activate TRPV1 channels, when they were stably transfected in HEK-293 cells. This possibility is also a key tool in neurotechnology due to the importance of TRPV1 channels as a receptor involved in body temperature regulation, heat and pain detection in sensory nociceptive fibres and functions in the central nervous system including response to neurogenic inflammation, cytoskeletal remodelling, synaptic remodelling and plasticity, neuronal excitability and cell survival[79].

In the broader realm of neural tissue, devices have expanded beyond cells and the retina to target other areas of the nervous system. One notable application is the use of light-induced electrical stimulation for chronic activation of the peripheral nervous system[80]. This approach involves implants that convert deep red light into electrical signals, enabling long-term modulation without transcutenous connections. Additionally, researchers have developed devices that directly interface with the cortex[81], demonstrating the potential of light-based neural stimulation across various neurological targets.

Apart from neurons, photostimulation of astrocytes, critical for supporting neuronal function, was also attempted[82]. Photoexcitation of the ITO/P3HT:PC60BM conductor/semiconductor interface caused membrane depolarisation mediated by the ClC-2 chloride channel, highlighting the possibility to use organic semiconducting materials to probe ion channels in non-excitable cells.

1.5.6 Further neurostimulation applications for organic photovoltaics

In addition to the POLYRETINA, epiretinal implant developed by Ghezzi et al.[71], the other main exploration of organic photocapacitive neurostimulation has been through a planar device developed in the Glowacki lab. In this case, a planar junction of organic pigments act as a photocapacitor with a thin metallic electrode beneath[66]. This has been applied to peripheral nerve stimulation[80] using deep red light to elicit a motor response in rodents during chronic implantation. It has also been applied to the somatosensory cortex of mice using laser pulses of deep red light[81].

1.5.7 Summary

The field of organic PVs, while relatively young compared to its inorganic counterpart, holds immense promise for revolutionizing neuromodulation applications. Its unique advantages,

including flexibility, semi-transparency, and the potential for cost-effective production using roll-to-roll processing techniques, make organic materials an attractive avenue for research in the realm of implantable devices. The ability to fine-tune their properties through molecular design further fuels optimism for advancements in efficiency, stability, and biocompatibility, which are essential for long-term functionality within the body.

The successful integration of organic PV materials for neurostimulation, as explored in this thesis, not only opens up new avenues for treating neurological disorders but also signifies a broader potential for OPVs to bridge the gap between energy generation and medical technologies. The inherent biocompatibility of certain organic materials, coupled with their tunable properties, allows for the development of devices that seamlessly integrate with biological systems. This thesis demonstrates the feasibility of utilizing organic PV implants to convert light into electrical energy for direct neural stimulation, paving the way for wireless and potentially less invasive neuromodulation therapies.

1.6   Thesis outline

1.6.1   General objective

The overall goal of this thesis was to develop a photovoltaic implant with sufficient efficiency to enable wireless neurostimulation with cortical stimulation as the primary avenue for exploration. The initial objective was to define microfabrication tools, characterization platforms and materials using a well-known photoactive polymer. A concurrent goal was to establish appropriate benchmarks for photovoltaic device performance by using electrical implants to determine the parameters necessary for activating cortical tissue. Combining the output from these studies, the main goal was then to develop a photovoltaic neural implant sensitive to near-infrared light and evaluate its function.

1.6.2   Outline

Continuing in this thesis, the following chapters present the investigated aspects pertaining to the objective of developing an organic photovoltaic neural implant. Each chapter begins with the relevant background sections critical for understanding the goals and mechanisms investigated in the chapter. The methods and results are then presented followed by a discussion specific to the gathered data.

Chapter 2: Establishing a measurement framework: using a common green-sensitive polymer to explore and define key parameters used to assess photovoltaic performance in vivo.

This chapter aims to develop reliable methods to fabricate photovoltaic devices for neural implants and define metrics to assess the performance of these fabricated devices.

Chapter 3: In vivo electrical neurostimulation: defining performance targets for photovoltaic

pixels

This chapter iterates various fabricated neural implants for cortical stimulation using electrical pulses. This is to reach the aim of determining the required electrical stimulation parameters needed for cortical stimulation.

Chapter 4: Fabrication and optimization of a near-infrared pixel for neurostimulation applications.

This chapter comprises of the incremental optimization steps involved in fabricating an organic photovoltaic pixel sensitive to NIR light.

Chapter 5: Discussion and Outlook

Each chapter has its own discussion but this chapter summarises and aggregates the achievements, limitations and future perspectives when taking the presented work as a whole.

2 Establishing a measurement framework for photovoltaic neurostimulation

Outline

This section details the development and characterization of a green-sensitive P3HT:PCBM photovoltaic device as a model system for establishing microfabrication techniques and evaluating photovoltaic performance metrics for neural stimulation.

Personal contribution

I designed the study, chose materials, designed and fabricated devices, performed experiments, ran simulations and conducted data analysis.

Acknowledgements

The results presented in this section were made possible by Marta Airaghi Leccardi, Golnaz Sherafatipour and Vivien Gaillet. MAL designed the optimized POLYRETINA. GS provided guidance in terms of design and material handling. VG developed the hybrid COMSOL and NEURON model used for simulations.

2.1 Background

An appropriate measurement system must be established to accurately assess whether fabricated photovoltaic pixels can elicit neuronal responses in the cortex. Standard solar cell characterization focuses on power efficiency as the main metric to optimize, however, for evaluating the performance in vivo, a more nuanced approach is required. To ensure the device can effectively interface with neural tissue, it is crucial to explore several key aspects. These include generating specific stimulation patterns for neural activation, determining stimulation thresholds, assessing the range of safely deliverable charge densities, and examining the temporal dynamics of the system.

2.1.1 Characterization of solar cells

The current density-voltage (JV) curve stands as a cornerstone for evaluating and enhancing solar cell performance. By plotting the relationship between the solar cell's generated current density (J, in mA/cm²) and the applied voltage (V) under illumination, the JV curve reveals key parameters such as short-circuit current (J_{sc}), open-circuit voltage (V_{oc}), fill factor (FF), series resistance (R_s), shunt resistance (R_{sh}) and ultimately, the power conversion efficiency (PCE). Figure 3.1 illustrates a typical JV curve, showcasing these parameters and their significance in understanding and optimizing solar cell technology.
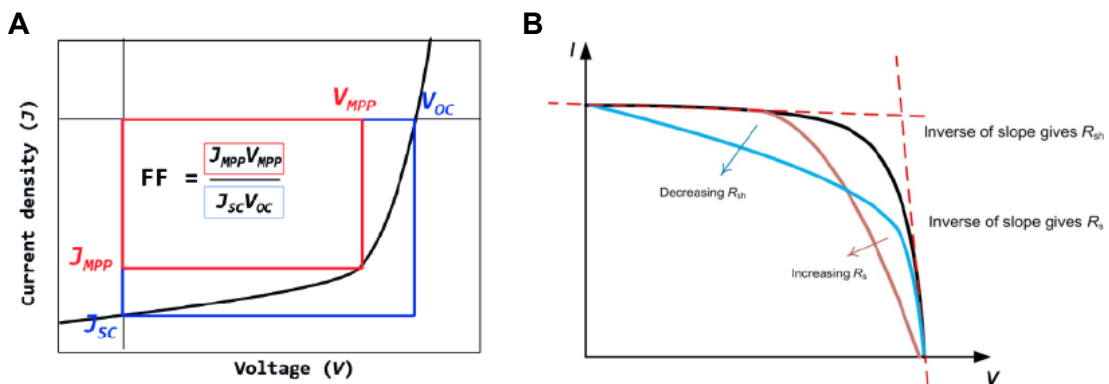
Figure 2.1: **JV curve and their metrics** A) Typical JV curve with short-circuit current density (J_{sc}), open-circuit voltage (V_{oc}), max power point (MPP) current density (J_{MPP}), MPP voltage (V_{MPP}) and associated fill factor (FF). Adapted from Doumon et al[83]. B) Effect of change in series resistance (R_s) and shunt resistance (R_{sh}). Adapted from Kontges[84].

One of the most fundamental parameters derived from the JV curve is the J_{sc}. This represents the maximum current density the solar cell produces when the voltage across its terminals is zero, the short circuit condition. The magnitude of the J_{sc} reflects the cell's success in efficiently absorbing light and collecting the generated charge carriers. Similarly, the V_{oc} extracted from the JV curve dictates the maximum voltage the solar cell can generate under no current flow (open circuit condition). The V_{oc} is strongly influenced by the material's bandgap

and the overall quality of the semiconductor junction.

For practical applications, locating the maximum power point (MPP) on the JV curve is essential. The MPP marks the specific combination of current and voltage where the solar cell delivers its maximum power output. Solar cells are designed to operate as close to their MPP as possible for optimal efficiency. Further analysis of the JV curve reveals the fill factor (FF, Equation 2.1), a dimensionless quantity that expresses the "squareness" of the curve. Mathematically, it is the ratio between the maximum power produced by the solar cell and the theoretical maximum power calculated as the product of J_{sc} and V_{oc}. A high FF demonstrates minimal internal losses within the cell, maximizing power delivery. The overall efficiency of the solar cell (PCE, Equation 2.2), perhaps the most critical performance metric, is determined from the JV curve by dividing the maximum output power by the input light power. This percentage quantifies how effectively the solar cell transforms incident light energy into usable electricity.

$$FF = \frac{J_{MPP}\,V_{MPP}}{J_{sc}\,V_{oc}} \tag{2.1}$$

$$PCE = \frac{P_{out}}{P_{in}} = \frac{FF\,J_{sc}\,V_{oc}}{P_{in}} \tag{2.2}$$

Beyond these primary metrics, a close examination of the JV curve's shape uncovers insights about potential bottlenecks and losses within the solar cell. For example, significant deviations from the ideal curve with a reduced slope near the V_{oc} region could signify the presence of series resistances (Figure 2.1B). Conversely, a decreased slope of the JV curve near the J_{sc} region points to high R_{sh}, which act as bypass paths, diverting current away from its intended route. Furthermore, various non-idealities in the semiconductor materials or imperfections introduced during the fabrication process may express themselves as distortions or kinks within the JV curve. One notable example of this is the "S-kink," an s-shape curvilinear deformation in the shape of the curve, which is well-known to significantly lower the fill factor and thus the efficiency. By identifying these anomalies, researchers can pinpoint specific areas where improvements to the cell's structure and materials could yield enhanced performance.

In essence, the JV curve serves as a diagnostic tool for solar cell development. Careful extraction of key parameters and meticulous analysis of the curve's shape grants a profound understanding of the intricate processes governing solar cell behaviour.

2.1.2 The electrode-electrolyte interface and the need for pulsed neurostimulation

The electrode-electrolyte interface, formed where the surface of a stimulating electrode meets the ionic environment of biological tissue, dictates the efficiency and safety of neural signal transmission. Understanding its complexities is essential for designing effective and biocom-

patible neurostimulation devices[85]. The capacitance of this interface becomes particularly important under pulsed conditions, as it influences the time required to build up or dissipate charge. Additionally, both the resistance at the electrode-electrolyte interface and the resistance of the solution itself can change dynamically in response to the pulsed stimulation. This dynamic change impacts the efficiency of charge transfer and influences the overall effectiveness of the stimulation.

At the heart of this interface lies the charge transfer process. In neurostimulation, electrical current from the electrode must be translated into the flow of ions within the electrolyte (Figure 2.2A). This can occur through two primary mechanisms: faradaic reactions and non-faradaic reactions. Faradaic reactions involve the direct exchange of electrons between the electrode and solution species, leading to oxidation or reduction reactions at the electrode surface[86]. While potentially efficient in charge transfer, they can introduce harmful byproducts and lead to electrode wear, sometimes limiting their long-term suitability. Alternatively, capacitive charging relies on the formation of an electrical double layer at the interface. Ions within the electrolyte rearrange themselves in response to the surface charges on the electrode, forming a capacitor-like structure. Capacitive charging is generally considered safer and more reversible than faradaic processes.

The characteristics of the electrode-electrolyte interface are influenced by several factors. The surface chemistry, roughness, and conductivity of the electrode directly impact charge transfer mechanisms and the propensity for unwanted reactions. Biocompatible materials such as platinum, iridium oxide, and conductive polymers are often employed to minimize these risks[87]. Additionally, the ionic species present in the surrounding tissue fluid influence both faradaic and capacitive processes. Finally, the amplitude, waveform shape, and frequency of the applied electrical stimulation can alter charge transfer dynamics and influence the balance of faradaic and capacitive contributions.

A typical solar cell's performance is evaluated under continuous illumination, where measurements such as the JV curve provide insights into the steady-state behaviour of the device. In contrast, PV neurostimulation often utilizes short, high-intensity light pulses. These rapid changes in illumination induce different electrical responses at the electrode-electrolyte interface (Figure 2.2B). While a powerful measurement, JV curves miss these aspects.

A
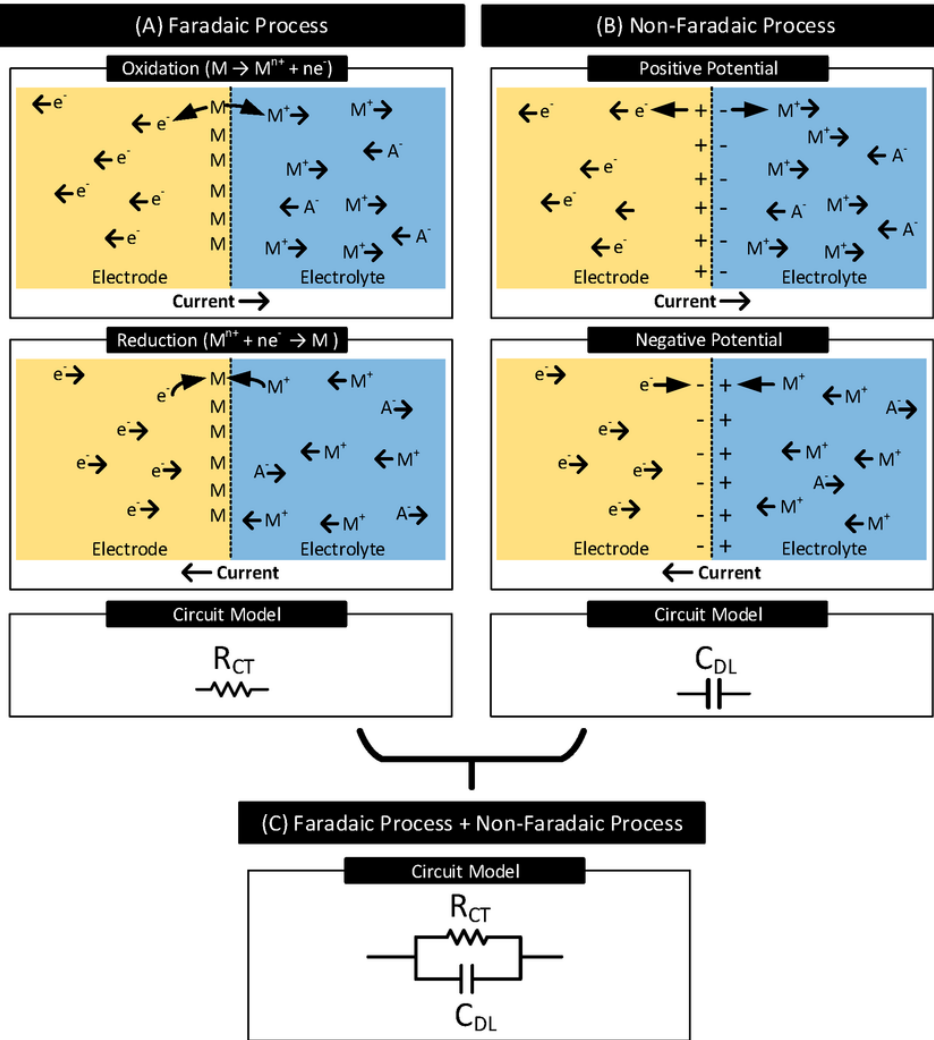
B
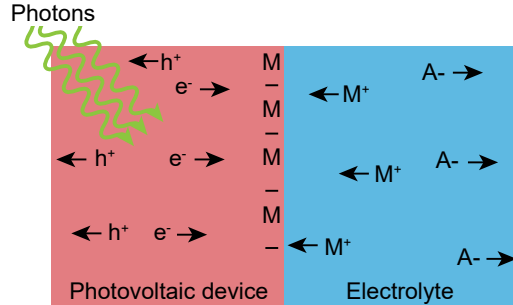
Figure 2.2: **Electrode-electrolyte interface** A) Right - the faradaic process with the direct exchange of charges, represented as a resistor in the circuit model. Left - the capacitive process with the double layer at the interface behaving as a capacitor in the circuit model. Adapted from Polachan et al.[88]. B) Schematic of the interface between the electrolyte and a PV device with photons entering the device, generating charges and affected ions in the electrolyte. Depending on the PV architecture, faradaic or capacitive processes can occur.

2.1.3   Capturing photovoltage and photocurrent

To assess the performance of photovoltaic pixels in a biological context, researchers employ various techniques that reflect their behaviour with the crucial electrode-electrolyte interface. These measurements, referred to as photocurrent and photovoltage output, are crucial for understanding device function within living tissue. A common approach involves exposing the photovoltaic device to an electrolyte solution, such as like PBS or saline, under light pulses[73,80]. A two-electrode set-up is often employed (Figure 2.3) where the electrolyte covers the pixel. This configuration allows for measuring photocurrent flowing through the bottom electrode and a larger reference electrode in the solution.

Such setups offer valuable insights into the influence of the electrode-electrolyte interface, particularly its time-dependent behavior. Understanding the charging and discharging processes of the pixel during pulsed light stimulation is critical. Furthermore, the capacitive and faradiac contributions of the interface can be understood and ensure safety limits are not exceeded.

Another method allows researchers to capture transient voltage changes by exposing both the top and bottom electrodes of the photovoltaic cell to the electrolyte. A separate recording electrode system can then measure the voltage shifts in the surrounding area helping to evaluate the device's spatial resolution for neural stimulation[80]. However, this relies on the placement of the recording electrode and takes the focus away from understanding the relative performance of photovoltaic pixels.
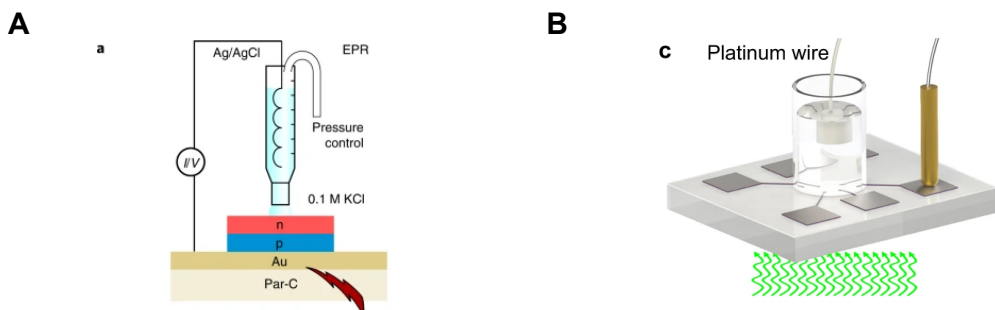
Figure 2.3: **Measuring photovoltage and photocurrent through the electrode-electrolyte interface** A) An experimental set-up with a pipette filled with 0.1 M KCl and an Ag/AgCl wire above a photocapacitive device. Current and voltage is measured as a function of time when light is delivered to the device. Adapted from[80]. B) An experimental set-up with a saline bath around photovoltaic pixels and a platinum wire. Contact is made with a gold pin to the pixel and current and voltage are measured between the pixel and the platinum wire. B) Adapted from[73].

2.1.4   Towards a photovoltaic implant for cortical stimulation

With these considerations in mind, several iterations were explored for the measurement of PV pixels in order for use in the biological setting. Inverted photovoltaic pixels, as described in Chapter 1, were fabricated and assessed with an evolving measurement parameters to explore the change while also optimizing the PV pixel itself. Building upon the POLYRETINA design[71], which utilizes P3HT:PCBM and PEDOT:PSS, this section will detail the necessary modifications to adapt this architecture for cortical stimulation. The green-sensitive P3HT:PCBM material was chosen due to its well studied properties in the solar cell community allowing a broad range of literature available for understanding and optimization. The primary aims were to fabricate photovoltaic pixels on glass substrates using materials not previously explored in the lab and establish techniques then used to assess the fabricated PV devices.

2.2   Methods

2.2.1   Semiconductor blend preparation

The photoactive materials were prepared under nitrogen atmosphere in the glovebox. Regioregular poly(3-hexylthiophene-2,5-diyl) (P3HT, M1011, Ossila) and [6,6]-Phenyl-C61-butyric acid methyl ester (PCBM, Ossila) were each dissolved in 1 mL of anhydrous chlorobenzene (99.85, Sigma Aldrich) at 20 mg/mL and stirred with a magnetic stirrer overnight at 70°C. These solutions were then filtered (0.5 μm PTFE filter) and blended in a 1:1 (v:v) ratio to form a P3HT:PCBM solution and stirred at 70°C for a minimum of 4 hours.

2.2.2   Chip microfabrication

The photovoltaic devices used for characterization were fabricated in an ISO5 to ISO 7 cleanroom (Neural Microsystems Platform, Campus Biotech, Geneva) on glass wafers as represented in Figure 2.4. The plain wafers were rinsed in acetone, isopropanol (IPA) and DI water then dried and treated with O_2 plasma (2 minutes, 600 W - PiNK V10-G, Germany) to clean and activate the surface for the subsequent photolithographic process. A 2.5 μm layer of photoresist (AZ1512, Microchemicals, Germany) was spin coated, baked (110°C, 90 seconds) and exposed (150 mJ/cm^2, 405 nm, MLA150, Heidelberg Instruments, Germany) and developed. Indium Tin Oxide (ITO) was sputtered using DC magnetron sputtering (nominal thickness 200 nm, 200 W, 2 sccm O_2, AC450CT, Alliance Concept, France). The wafer was then immersed in acetone, upside-down, in sonication (20 minutes, 80 kHz) to liftoff the ITO, rinsed in acetone, IPA and wafer then dried with nitrogen.

Following this, the photovoltaic pixel was layered upon this base ITO layer. The wafer was dehydrated for 10 minutes at 140°C then surface activated using O_2 plasma (30 s, 18 W, Diener Electronic, Germany) before being transferred to a nitrogen (N_2) atmosphere glovebox (MBraun, UNIlab pro).

Zinc oxide (ZnO) nanoparticles (H-SZ51029, Genesink, France) were redispersed through sonication (37 kHz, 3 minutes) then spin coated (nominal thickness 30 nm, 1 mL, 2000 rpm, 45 s), annealed (10 mins, 140°C) and vacuum dried (20 minutes). The P3HT:PCBM blend was spin coated (nominal thickness 110 nm, 400 μL) at 1000 rpm for 60s and annealed for 30 minutes at 115°C. Initial fabrication utilised PEDOT:PSS as the hole-transport layer. This involved filtering (1μm PTFE filter) the PEDOT:PSS solution (HTL Solar, Ossila) and spin coating at 3000 rpm (nominal thickness 90 nm). Tests replacing the hole-transport layer with a metal oxide (Nickel oxide (NiO), Tantalum Oxide doped Tungsten Oxide (TaWO$_3$), Tungsten Oxide (WO$_3$), Antimony-doped Tin Oxide (ATO), Avantama) were each carried out in the same way. The metal oxide nanoparticle solution was redispersed through sonication (37 kHz, 3 minutes) then spin coated (1 mL, 2000 rpm, 45 s) and annealed at 115°C for 30 minutes.

To deposit the top electrode, Au (nominal thickness 30 nm), Pt (nominal thickness 200 nm) and Iridium Oxide (IrOx, nominal thickness 200 nm) were sputtered at 100W, 100W and 150W respectively. The wafer was then dehydrated at 5 minutes at 80°C then coated with 1.5 μm of AZ1512 photoresist, patterned with the MLA150 and developed. A reflow at 2 minutes at 120°C was done prior to ion-beam etching (Veeco Nexus IBE350) which removed all unprotected material. The etching was tracked using Secondary Ions Mass Spectroscopy (SIMS) and stopped after ITO etching was detected. To remove the remaining photoresist, oxygen reactive ion etching (Corial 210IL ICP-RIE) was done leaving the pixels of the photovoltaic stack patterned.

Finally, the wafer was encapsulated in 5 μm Parylene C (Comelec C-30-S) using oxygen plasma and silanization (A174 silane) to improve adhesion. To expose the electrodes and contacts, a final photolithography step was completed using 8 μm of AZ10XT photoresist as the mask for oxygen RIE. The remaining photoresist was stripped using a brief sonication bath in acetone. The wafer was diced by hand using a diamond-tipped pen to obtain 19mm x 23 mm glass chips.

2.2.3 Measurement of photovoltaic and photocurrent in solution

To measure these fabricated devices, a plastic reservoir was placed around the pixels above the Parylene C encapsulation. It was adhered with clear silicone and cured for 1 hour at 60°C. The reservoir was then filled with 0.9% saline solution and a platinum wire was immersed as the counter electrode. Chips were placed in a holder with the 565 nm green LED (500 - 650 nm, M565L3-C5, Thorlabs) below and gold push pins used to connect to each individual pixel via the contacts.

A light pulse was controlled by a DAQ board (PCIe-6321, National Instruments) and the photovoltage and photocurrent were measured separately by connecting the appropriate amplifier (PV from DL Instruments Model 1201, PC from DL Instruments Model 1212). Data sampling was as 200 kHz to ensure the initial response of the PV was captured and light pulse trains were controlled by custom software.
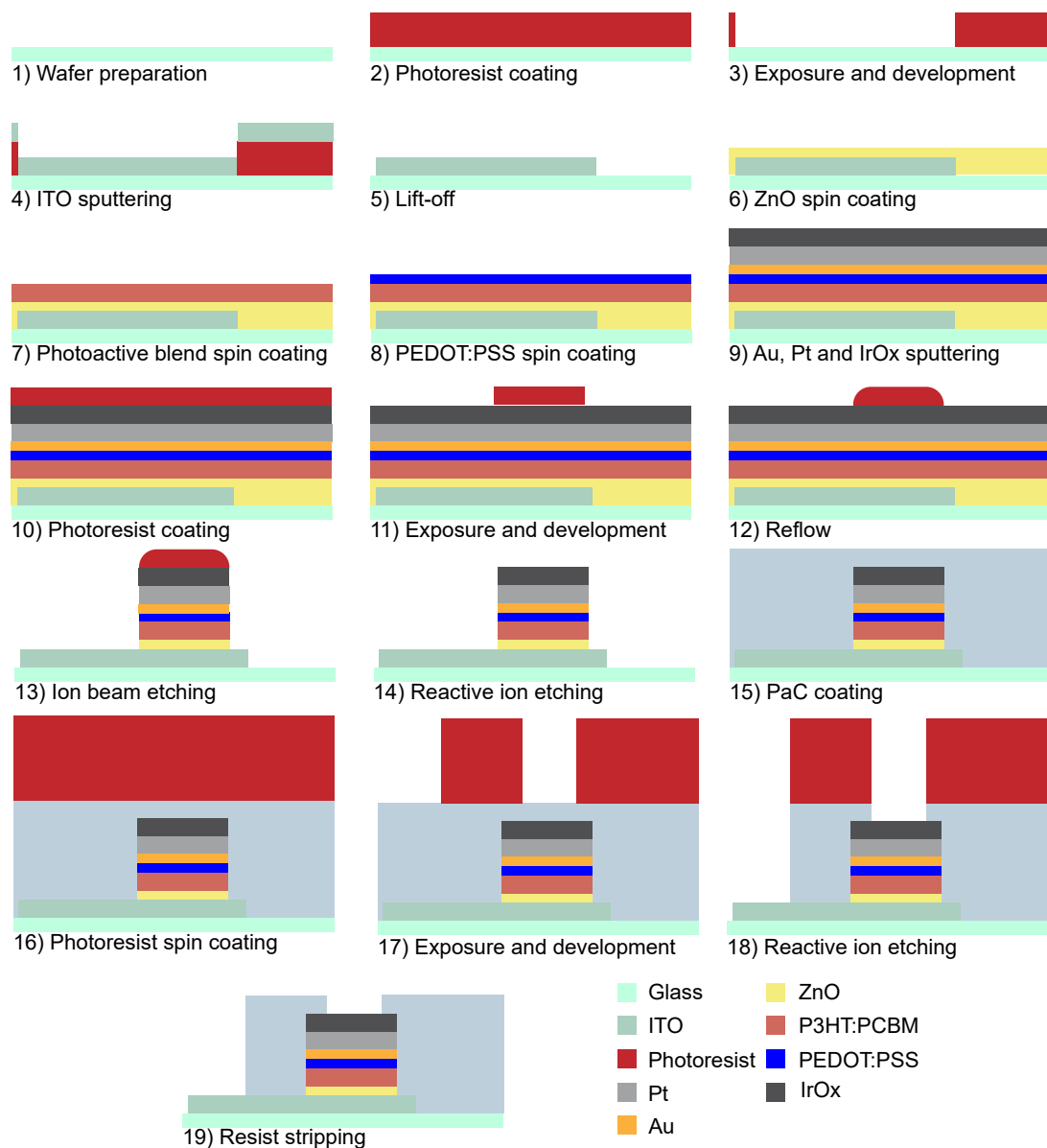
Figure 2.4: **Process flow for PV pixels on glass**

Initial tests had PV pixels that were circular with diameters of 1 mm and subsequent designs had diameters of 70 µm, 175 µm, 350 µm and 700 µm to investigate the impact of pixel diameter on performance. For every pixel, the electrode opening had a radius 10 µm less to account for alignment issues. Measurements were all normalized to the area of the pixel, not the opening unless stated otherwise.

2.2.4   Electrochemical characterization

In order to characterize the electrode coating, SIROF, and compare it to other feasible options in the lab several methods of characterization were used. A three-electrode set-up was used with a counter electrode of a large Pt wire and a reference Ag/AgCl electrode connected to a potentiostat (Compact Stat, Ivium Technologies) and taken in PBS (1x) at pH 7.2 at room temperature. To compare SIROF and Titanium Nitride (TiN), another material available for sputtering and used for electrode coatings, the charge-storage capacity (CSC) was determined using cyclic voltammetry.

The voltage was scanned between -0.6 and 0.8V at a slow scan rate of 50 mV/s for a total of 5 sweeps. The first sweep was discarded due to instability in the recording then the next 5 sweeps were averaged and the total CSC was calculated as the area within the curves on the current-voltage plots. Impedance spectroscopy was also performed between 1 Hz and 100 kHz using a 50 mV AC voltage.

2.2.5   Voltage Transients

For stimulation devices, the charge injection capacity (CIC) was critically important and was also calculated using the same three electrodes in the same conditions. Symmetric 0.4 ms current pulses were charge-balanced and cathodic first with a 400 µs interphase period. Stimulations were run at increasing current amplitudes until the E_{mc} or E_{ma} exceeded the water window of these electrodes (-0.6 to 0.8V for metallic electrodes). The E_{mc} and E_{ma} were defined as the voltage value 10 µs after the end of the cathodic or anodic pulse, respectively, to avoid the ohmic drop. An average of 10 pulses were used to determine the E_{mc} and E_{ma}. The maximum injection current was defined as the maximum current with which the electrodes could be stimulated without exceeding the water window. From this, the CIC was determined by the corresponding charge for this maximum injection current and divided by the geometric surface area of the electrode.

2.2.6   Kelvin probe force microscopy

KPFM measurements were utilised to investigate the surface electrical properties of the materials, namely determining the work function (Φ) of the materials. Due to the sensitivity of these measurements, samples had to be prepared on pure Si wafers instead of the standard glass wafers used for processing. Each sample was applied to the Si sample, by either sputtering or doctor-blading, and annealed as done during the standard fabrication process. Samples were measured with an atomic force microscopy set-up (Dimension Icon, Bruker) in KPFM mode. SCM-PIT-V2 (Bruker) tips, with an electrically conductive Pt-Ir tip, were used in a DAFMCH holder (Bruker) as recommended by the supplier. The Φ_{tip} was first determined by comparison to a reference Au (Φ_{Au} = 5.3 eV) and Al (Φ_{Al}= 4.2 eV) sample then measured against the experimental sample and calculated by equation 2.3.

$$\Phi_{sample} \quad = \quad \Phi_{tip} - \Delta_{Potential} \tag{2.3}$$

2.2.7 Measurement of JV curves

Current density-voltage (JV) behaviour, as common in solar cell performance evaluation, was used to further characterise the solar pixels. The fabrication process for JV chips followed the same steps as Figure 2.4 but stopped at step 14, without the final encapsulation step.

Pixels were measured kept at room temperature, in dry conditions in both dark and light (523 nm, 0.76 mW/mm$_2$, Modulight, Ivium Technologies). The potentiostat (Compactstat, Ivium Technologies) applied a linear voltage sweep between -0.2 and +0.8 V with a 1 mV step and measured the output current from each pixel. As with the measurements in saline, the current was normalized to the area of the PV pixel unless stated otherwise. The V_{oc} and J_{sc} were extracted from the JV curves, FF and PCE were calculated as per equation 2.1 and 2.2. The series resistance was calculated as the tangential slope at the point of V_{oc} and the shunt resistance was determined from the tangent at the J_{sc} point.

2.2.8 Hybrid Finite Element Analysis model and NEURON simulation

Simulations were performed using the model reporting previously in Gaillet et al.[89]. Briefly, an FEA model was built in COMSOL Multiphysics 5.3 using a stationary current study in the AC/DC module. The optic nerve was simulated with concentric layers of the nerve tissue, meningeal layers and surrounded by saline solution. A model device, the opticSELINE, was positioned transversally to the modelled optic nerve.

The resultant 3D voltage maps were used as input for the NEURON environment (v.7.4) where nodes of Ranvier are active segments and myelinated segments are perfect insulators. The voltage field was modulated based on the pulse width and for the PV-like pulses, a slow decay was modelled instead of an on-off voltage modelled for standard electrical stimulation. An axon was considered activated if an action potential was propagated to both ends of the axon. The probability of activation was calculated as the percentage of all possible axons, of different sizes and weighted by the frequency of occurrence and diameter, within the volume.

2.2.9 Data analysis

Data analysis and graphical representation were done in MATLAB (Mathworks). Normality was determined using the D'Agostino-Pearson's K2 test and a one-way ANOVA or Kruskal-Wallis test conducted between groups. In plots, p-values were reported as: *p < 0.05, **p < 0.01, ***p < 0.001, and ****p < 0.0001.

2.3   Results

2.3.1   Initial fabrication and characterization of inverted P3HT:PCBM photovoltaic pixels

Photovoltaic pixels for characterization were fabricated to test their performance and begin the process of optimization. A processed wafer is depicted in Figure 2.5A, taken at step 14 in Figure 2.4, where the ITO contacts and pixels are visible. Each pixel was built atop the ITO, composed of ZnO as the electron-transport layer, P3HT: PCBM as the photoactive layer, PEDOT:PSS as the hole-transport layer and a layer of Au above this. This was covered with a final top contact of Pt and iridium oxide (Figure 2.5B) defining the inverted photovoltaic pixel. After dicing, a plastic well was attached and placed in the experimental set-up (Figure 2.5C) with one contact on the ITO and a Pt wire in the 0.9% saline bath. This design was to capture the behaviour of the pixels in the in vivo environment due to the double layer capacitive charging seen as the electrode-electrolyte interface. In this set-up, a 1 s light pulse of 1 mW/mm^2 was exposed to the pixel and the photocurrent and photovoltage curves (Figure 2.5D) were extracted. The fabrication process was done with or without depositing an Au interlayer to compare the performance with different HTL-metal interfaces.

The representative trace depicts a cathodic photovoltage of 543 mV for the 1 mm diameter photovoltaic pixels not containing Au, compared to 403 mV with Au (Figure 2.5D). The potential was built up almost immediately at the beginning of the light pulse (Figure 2.5E) and remained stable over the 1 second pulse. When the light pulse was turned off (Figure 2.5F), the photovoltage showed a slow decay for both types of pixels. Concurrently, the representative trace for photocurrent depicted a clear cathodic peak reaching a magnitude of 121 μA. This peak was achieved at the light onset, when the change in voltage was most rapid, then followed by an exponential decay to close to zero as the light remained on, as expected from the electrode-electrolyte model with the capacitive interface. At the end of the light pulse, there was an anodic peak depicting the reversal of current as the pixel discharges. The pixels without Au had better performance than those also containing Au with a significantly higher peak photovoltage (Figure 2.5F, p = 0.0006), peak photocurrent density (Figure 2.5G, p = 0.0004) and charge density (Figure 2.5H, p = 0.0021).

The photovoltaic behaviour of the pixels without Au was further investigated with different light intensities and pulse durations. Pulses of 50 ms with increasing light intensity, from 0.05 to 2.5 mW/mm^2, were applied to the same pixel over the span of 15 s. The peak cathodic voltage had an initial sharp increase, sensitive to low irradiance intensities, which then stabilises as the light intensity reaches the maximum (Figure 2.6A) while the cathodic current density increases almost linearly with increasing power (Figure 2.6B). This was expected since solar cells produce a current proportional to the amount of absorbed light. Both peak current and peak voltage had a stable behaviour between pixels on the same batch while the charge was highly variable (Figure 2.6C). Each pixel followed a similar trend attributed to the dynamics occurring within the pixel and at the electrode-electrolyte interface. Defects in the films and
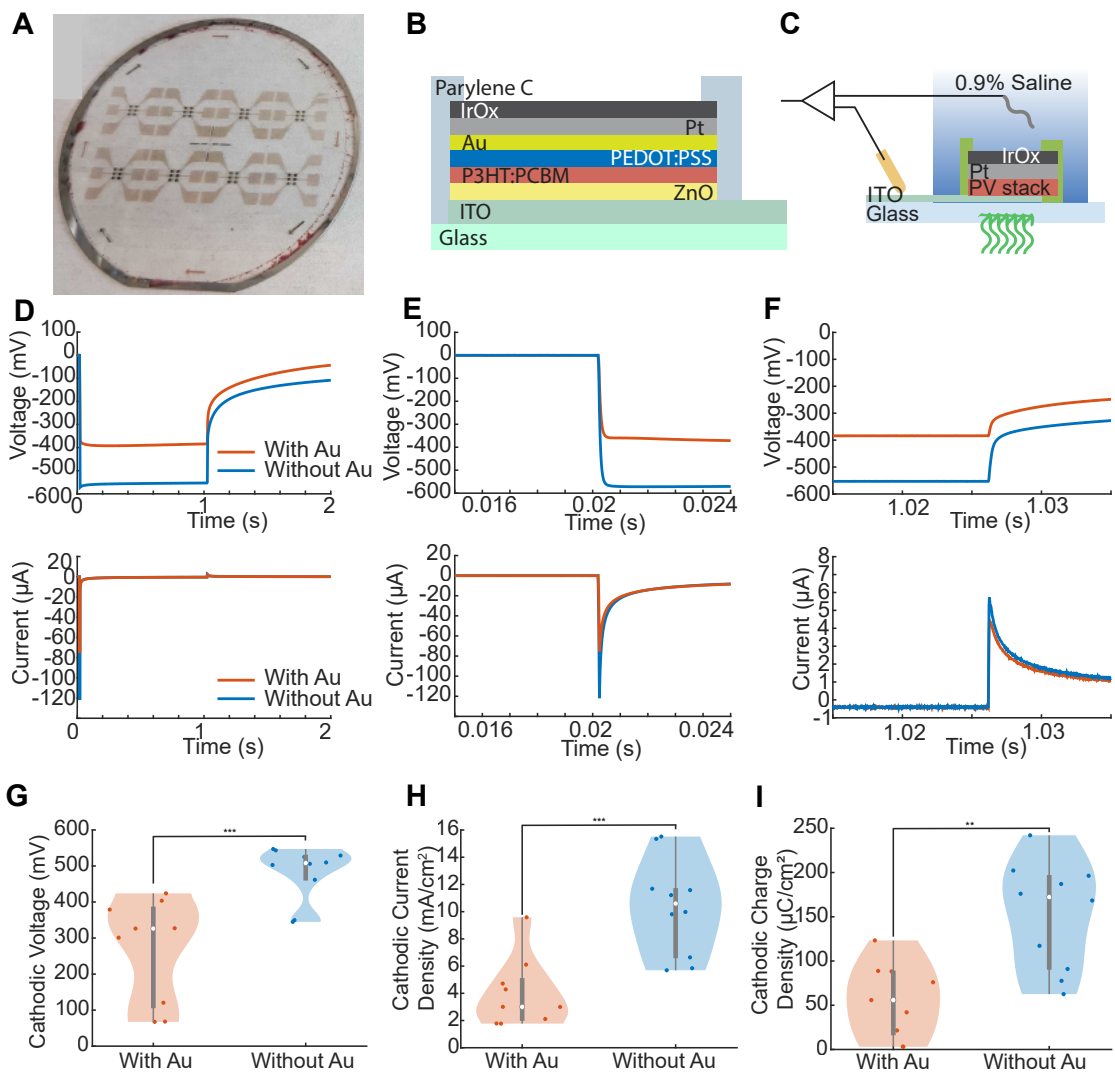
Figure 2.5: **Design and characterization of photovoltaic pixels** A) 4" glass wafer with patterned ITO contacts and PV pixels of 1 mm diameter B) Cross-section of the photovoltaic pixel including: base glass substrate, a layer of ITO (200 nm), a layer of ZnO (30 nm), a layer of P3HT:PCBM (110 nm), a layer of PEDOT:PSS (90 nm), a layer of Au (30 nm), a layer of Pt (200 nm) and a layer of IrOx (200 nm). C) Diagram of the experimental set-up with green (550 nm, 1 mW/mm^2) light coming through the glass into the PV pixel. The return electrode is a Pt wire in the 0.9% saline bath. D) Examples of the voltage vs time (top) and current vs time (bottom) measures with light pulses of 1 s for pixels with (orange) and without (blue) Au. E) A zoom-in of D at the light onset, at the start of the pulse. F) A zoom-in of D at light offset at the end of the pulse. G-I) Violin plots of peak cathodic voltage, peak current density and cathodic charge density with (blue) and without (blue) Au. Vertical lines indicate the interquartile range and medians are indicated by a white circle. n = 9 electrodes for each group.

slight differences at the electrode interface can greatly affect the final charge that is delivered over the 50 ms pulse.

To further explore the dynamic performance of the pixels, a 20 Hz pulse train of 10 ms light pulses was delivered. From Figure 2.6D, the voltage profile attained a maximum at -287 mV which did not change over 100 pulses (Figure 2.6G). It was noticeable that the cell never fully discharged, stabilising at a minimum of -68 mV. Conversely, the peak photocurrent diminished over the first 10 pulses and then maintained a lower peak current, between 20-30% of the initial current, over the pulse train (Figure 2.6E,I). This was more distinctly seen in the charge density of each pulse (Figure 2.6H) where, for most pulses, less than 20% of the initial pulse charge, could be delivered.

A combination of FEM and neuronal modelling was used to ensure that the slow discharge (Figure 2.5D) was still capable of stimulating neuronal tissue. The stimulation probability for the same current amplitude, 5 µA, was compared between a squared pulse seen in standard electrical stimulation (Figure 2.7B) and a PV-like pulse profile (Figure 2.7A). Minor differences in the stimulation probabilities were seen (Figure 2.7C) favouring the electrical pulse.
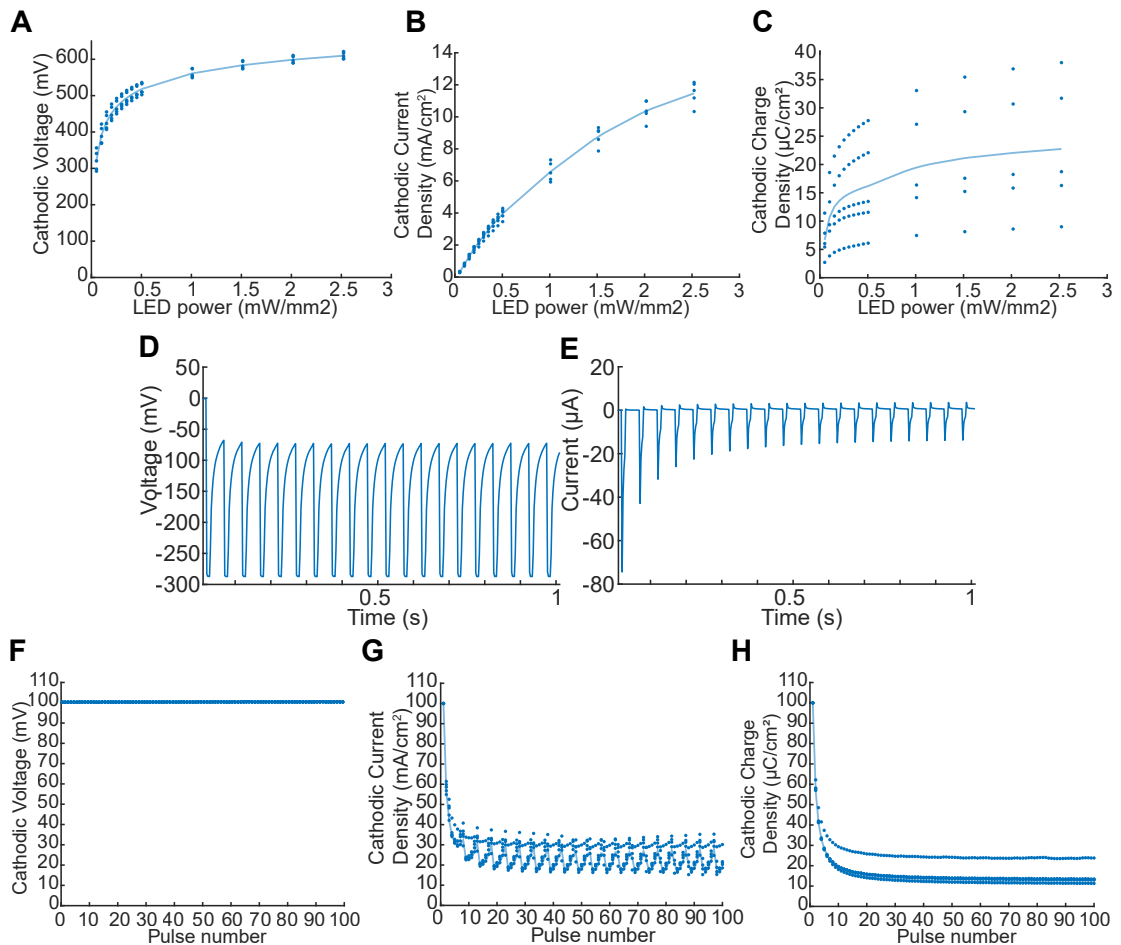
Figure 2.6: **PV pixel performance in variable conditions** A) Change in peak cathodic voltage with increasing light (550 nm) irradiance from 0.05 to 2.5 mW/mm^2. n = 5 pixels. B) Change in peak cathodic current density with increasing light (550 nm) irradiance from 0.05 to 2.5 mW/mm^2. n = 5 pixels. A) Change in peak cathodic charge density with increasing light (550 nm) irradiance from 0.05 to 2.5 mW/mm^2. n = 5 pixels. D) Representative trace of voltage vs time in response to 10 ms 2.5 mW/mm^2 pulses delivered at 20 Hz over 1 second. E) Representative trace of current vs time in response to 10 ms 2.5 mW/mm^2 pulses delivered at 20 Hz over 1 second. F) Relative change in peak voltage for 100 10 ms pulses at 20 Hz. G) Relative change in peak current density for 100 10 ms pulses at 20 Hz. H) Relative change in cathodic charge density for 100 10 ms pulses at 20 Hz. All values are normalized to the first pulse. n = 5 electrodes from 2 devices.
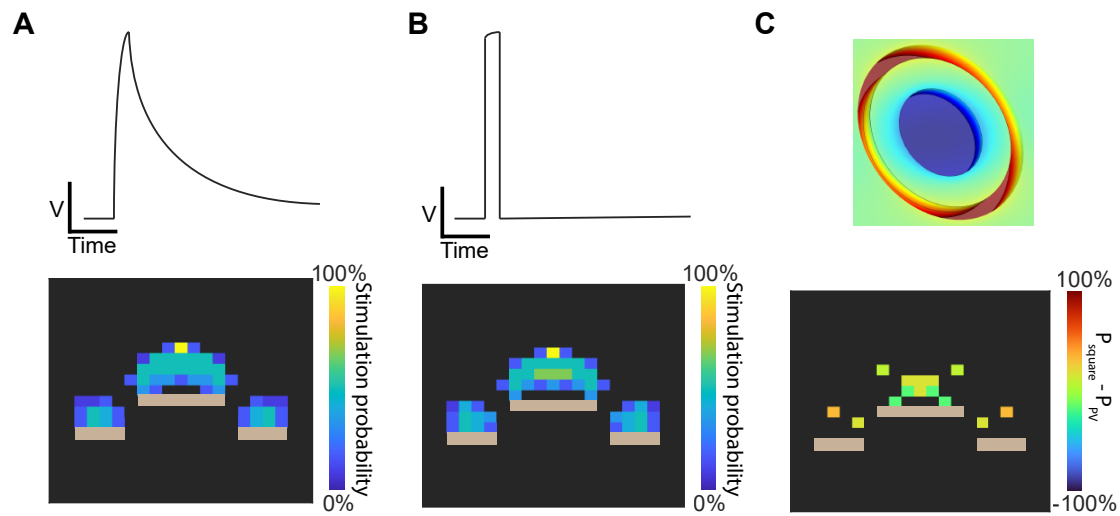
Figure 2.7: **Comparison of a PV-like pulse and a electrical pulse for neural stimulation** A) The stimulation probability (below) of a nerve using a photovoltaic-like pulse profile (above), with a slow decay. B) The stimulation probability (below) of a nerve using a standard current-controlled pulse (above) , with fast decay. A-B) Stimulation probability was from a 5 μA 5 ms pulse delivered to simulated optic nerve tissue. C) Above - the modelled stimulating and concentric return electrode. Below - Difference in stimulation probabilities of A and B. Electrodes are depicted in the probability map as the grey rectangles.

2.3.2 Replacement of PEDOT:PSS to improve fabrication yield

While efficient, weak bonding at the PEDOT:PSS - P3HT:PCBM interface (Figure 2.8A) led to many counts of failure during the microfabrication process (Figure 2.4) leading to a low (<20%) yield of intact and measurable devices. This failure was due to buckling seen in (Figure 2.8A (middle)) compared to a pixel not containing PEDOT:PSS (Figure 2.8A (left)). The subsequent delamination (Figure 2.8A (right)) resulted in many pixels being immeasurable or minimally functional due to a lack of the top interface. The issue at the PEDOT:PSS - photoactive layer interface can be explained by the lack of interfacial adhesion noted in literature[90].

In order to overcome this, metal oxide hole-transport layers reported in literature were explored as alternatives. These materials were NiO, Ta:WO_3 and WO_3 and, along with ZnO and ITO, were assessed for their work function via KPFM and depicted in an energy band diagram (Figure 2.8B) with the HOMO and LUMO of P3HT and PCBM from literature. ITO was assessed after sputtering on a Si wafer, while the metal oxides were in the form of a nanoparticle solution and were doctor-bladed on the Si wafer for electrical KPFM measurements. Figure 2.8C shows that after doctor blading, the material, NiO, had parallel grooves in the material however this did not affect the measured voltage from the AFM tip. The measured value is subtracted from the work function of the measurement tip, normalised to standards, to obtain the work function of the materials prepared. All metal oxides had comparable work functions, denoting their Fermi level, which is close to the valence band of hole-transport materials.

Chips were fabricated with each of the metal oxides available (NiO Φ = 5.34, Ta:WO_3 Φ = 5.24, WO_3 Φ = 5.55, ATO Φ = 5.43) and their tolerance of microfabrication and performance compared. All chips with metal oxides showed no buckling or delamination during the microfabrication process thus were completely intact for measurements. The remainder of the design and fabrication process was kept the same to compare the influence of the HTLs on the photovoltaic performance.

In terms of peak cathodic voltage, NiO had the highest with a median of 346 mV (n = 6, p = 0.00134) compared to ATO (214 mV, n = 4) and Ta:WO_3 (99 mV, n = 6). While the pixels were visually inspected for failure, a number of pixels produced very little response to the light, particularly true for multiple pixels with ATO and all pixels with WO_3, which was fabricated but did not produce any voltage or current in response to light thus was not plotted.

As seen in Figure 2.8F, NiO-containing pixels also produced the highest peak current density (2.88 mA/cm^2 vs ATO = 1.27 mA/cm^2, Ta:WO_3 = 0.65 mA/cm^2, p = 0.001337). This was not correlated with the cathodic charge produced by the pixels as NiO and ATO provided comparable amounts of charge (median = 0.15 μC/cm^2 vs 0.12 μC/cm^2) over the 10 ms pulses while Ta:WO_3 produced significantly less (median = 0.04 μC/cm^2, p = 0.0005021). The rate of capacitive decay had a large bearing on the total charge delivered, regardless of the peak current, with ATO having a slower rate than NiO.
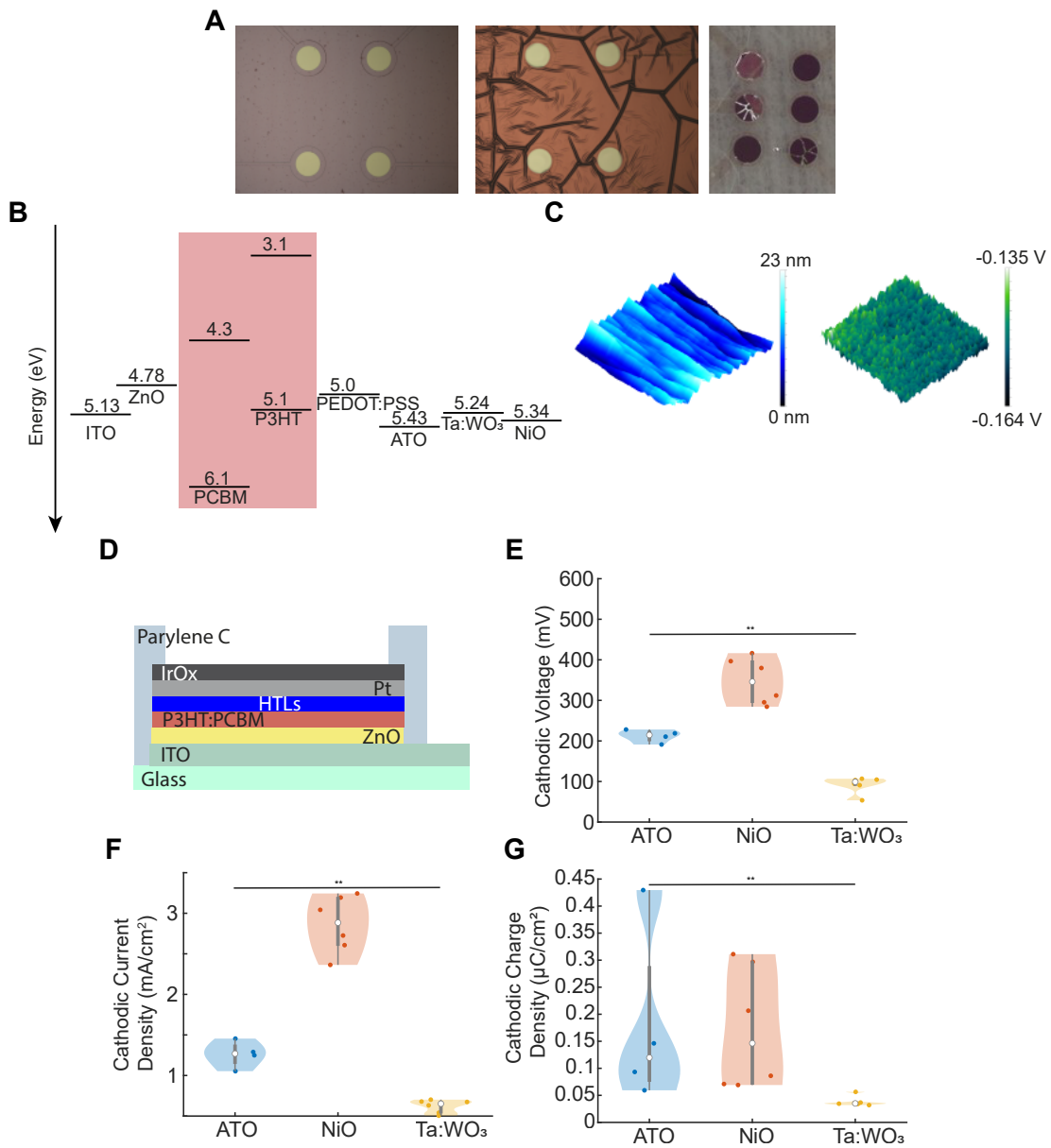
Figure 2.8: **Overcoming fabrication failures using metal oxide hole-transport layers** A) Intact pixels (left) compared to pixels containing PEDOT:PSS which have been buckled after exposure to solvents during photolithography (middle). Following fabrication, pixels that have buckled result in severe delamination (right). B) Energy diagram of the measured work function (Phi) of various metal oxides. This is compared with the HOMO (bottom) and LUMO (top) of P3HT and PCBM from literature. C) An example of KPFM with a measure of surface topology (left, blue) compared to the measure of contact potential difference (right, green) on NiO after doctor blading. D) The photovoltaic pixel structure tested with the HTL being changed for each group. E-G) Violin plots of peak cathodic voltage, peak current density and cathodic charge density for photovoltaic pixels with ATO (blue), NiO (orange) or Ta:WO$_3$ (yellow). Vertical lines indicate the interquartile range and medians are indicated by a white circle. n = 4, 6, 6 electrodes for each group respectively.

2.3.3   Updated reference electrode design and materials to replicate in vivo conditions

In order to more accurately reflect the performance of the pixel in vivo, the design used in Figure 2.8 was changed. The new design incorporated the reference electrode on the chip (Figure 2.9B-C) in a fixed position, to overcome the variability that comes from placing a large Pt wire in the saline bath (Figure 2.5B). This electrode was made from a semiconductive ITO layer with an IrOx coating to mimick standard implant electrode coatings and avoid degradation of the ITO material.

This design was used to compare the relative contributions that each transport layer, ZnO and NiO, made to the overall performance of the photovoltaic cell in an aqueous environment. To do this, the pixels from each group were fabricated in an identical manner (Figure 2.9A) but skipping the deposition step for the relevant material.

Most prominently (Figure 2.9D-F), the lack of ZnO showed a dramatic decrease in performance over all parameters which were all significantly lower than the performance of the complete pixel. In comparison, the removal of NiO from the design had no impact on peak voltage or current density but had a great impact on the total cathodic charge delivered to the pixel validating its inclusion in the pixel.

Neural interface incorporate an electrode coating through which charge is delivered to the neural tissue. In order to be compatible with the microfabrication process, the electrode coating must be able to be applied as a thin film through physical deposition techniques. Of the available materials, sputtered iridium oxide film (SIROF/IrOx) and titanium nitride (TiN) are commonly used in traditional electrodes and were available for processing. The films deposited via sputtering, both IrOx and TiN, were compared for their electrochemical properties for use in a neurostimulation device.

The CSC was assessed comparing the same thickness, 100 nm, and dimensions, 350 µm, of both materials. IrOx was capable of storing more charge (CSC = 60.6 mC/cm^2) compared to TiN (3.08 mC/cm^2) (Figure 2.9G,H) validating IrOx as use of the electrode coating of the available materials. IrOx as a coating was further probed to establish an appropriate layer thickness. Both 100 nm and 200 nm had the same CSC (59.7 vs 58.5 mC/cm^2) for the 340 µm openings meaning the thinner IrOx layer was still suitable as the electrode coating (Figure 2.9I). For this 100 nm thickness, different electrode opening sizes were assessed with the smaller 20 µm (104.2 mC/cm$^{2)}$ opening having a CSC larger than the larger 340 µm (Figure 2.9J). The CIC was assessed for the 20 µm diameter electrodes and found to be 1.46 mC/cm^2, in line with literature. While not as relevant for stimulation, the impedance of these films were compared with EIS (Figure 2.9K,L). As expected, larger openings have a much lower impedance magnitude than the smaller electrodes.
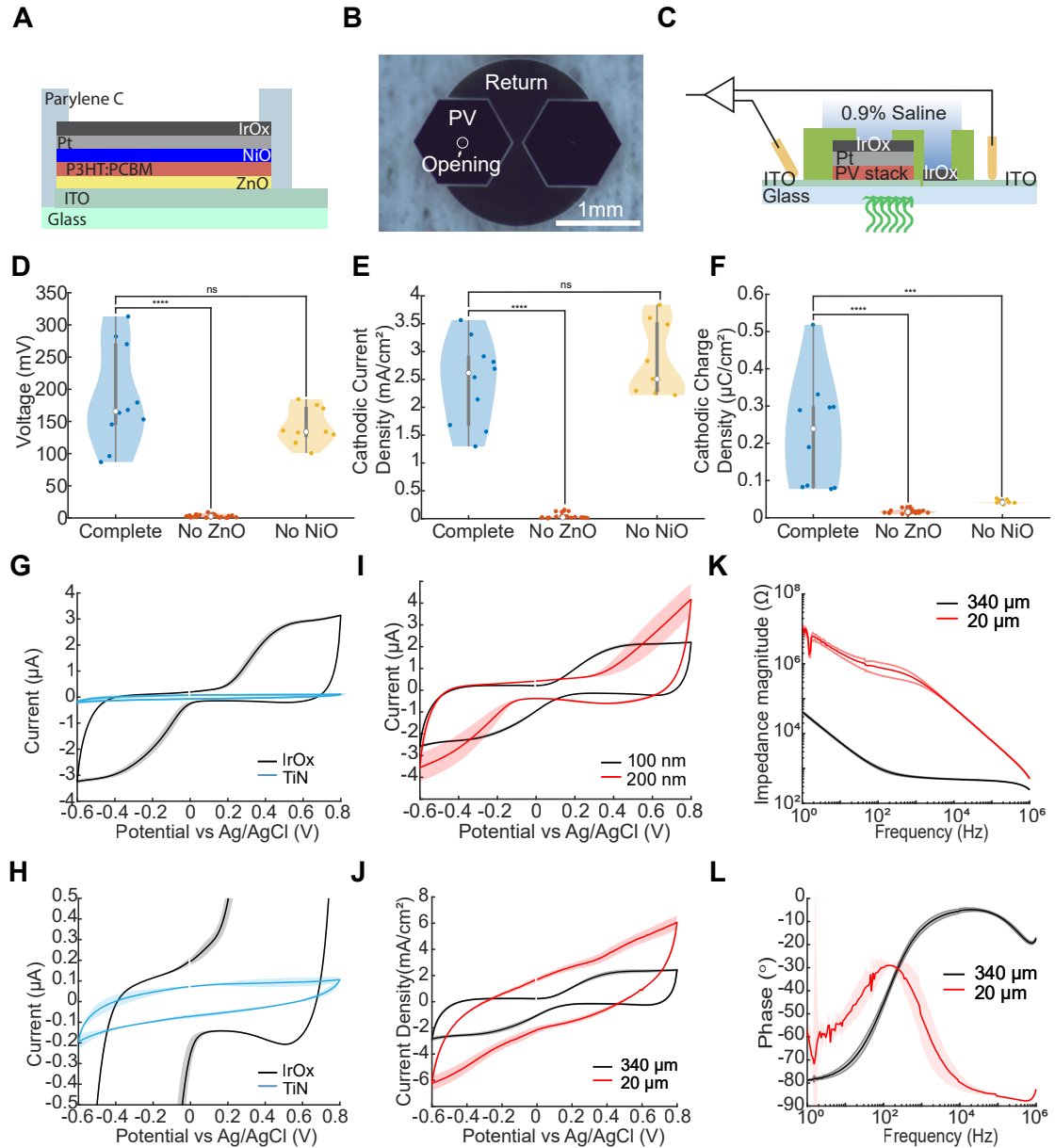
Figure 2.9: **Relative importance of pixel components to pixel performance** A) Cross-section of complete PV stack B) Image of the updated design with IrOx-coated PV and return electrodes. The opening is 20 μm in diameter, surrounded by the white circle. C) Experimental set-up with both the working and return electrode immersed in saline and exposed to 5 ms 2.5 mW/mm^2 light pulses. D) Peak Cathodic Voltage E) Peak Cathodic Current Density and F) Total Cathodic Charge Density for all 20 μm opening devices for complete (blue, n = 9), without ZnO (orange, n = 6) and without NiO (yellow, n = 9) pixels. The vertical grey lines indicate the interquartile range and medians are indicated by a white circle. G) CV curves (mean ± std) for IrOx (black, n = 3) and TiN (blue, n = 3) electrodes. H) Zoom of (G) to show the area of TiN I) CV curves (mean ± std) of IrOx electrodes with film thicknesses of 100 nm (black, n= 3) or 200 nm (red, n = 3) J) CV curves (mean ± std) for 100 nm IrOx electrodes with 340 μm openings (black, n = 3) and 20 μm openings (red, n = 3) electrodes. K) Impedance magnitude of 340 μm openings (black, n = 3) and 20 μm openings (red, n = 3) electrodes. K) Impedance phase of 340 μm openings (black, n = 3) and 20 μm openings (red, n = 3) electrodes.

2.3.4   JV behaviour of fabricated photovoltaic pixels

The photovoltaic behaviour in solution is critical for understanding the performance of the pixels in vivo however it lacks the ability to compare with standard solar cell literature. From the JV curve, the power conversion efficiency can be compared between different pixels though, unlike typical solar cells which are assessed under the equivalent of the full spectrum of sun illumination, the pixels were probed with a subset of this spectrum using a green LED. The efficiency of the fabricated pixels is also relevant to abstracting the performance of the interface from the pixel itself to make improvements. Thus, a new design (Figure 2.10A, B) was used to measure in a dry set-up by applying a potential difference between the top and bottom electrodes through a potentiostat. The overlap between the bottom ITO and top Pt determined the area of the photovoltaic pixel to which each measure was normalized.

Figure 2.10C shows the JV curve of pixels made with either a 120 nm or 170 nm thick layer of NiO while maintaining the same parameters for the rest of the device. From these curves, specific metrics were extracted. In Figure 2.10D, the J_{sc} of the thicker NiO was significantly more than the thinner NiO (median = 0.50 mA/cm^2 vs 0.28 mA/cm^2, p = 0.002165) while the V_{oc} (Figure 2.10E) were the same (median = 0.26 V vs 0.28 V, p = 0.132035). This means that the thicker NiO allowed better charge collection compared to the thinner layer but as the materials remained the same, the voltage did not different. The fill factor of both pixels was also the same (Figure 2.10F) meaning that no improvements in faults in the device were made. The thicker NiO had a lower series resistance (Figure 2.10G, median = 75 kΩ vs 57 kΩ, p = 0.015152) and same shunt resistance compared to the thinner NiO (Figure 2.10H, median = 150 kΩ vs 117 kΩ, p = 0.064935). This lower series resistance was likely the largest contributor to the higher J_{sc} that, in turn, led to higher efficiency (PCE) of the pixels with the 170 nm layer of NiO (Figure 2.10I, median = 0.28% vs 0.55%, p = 0.002165).
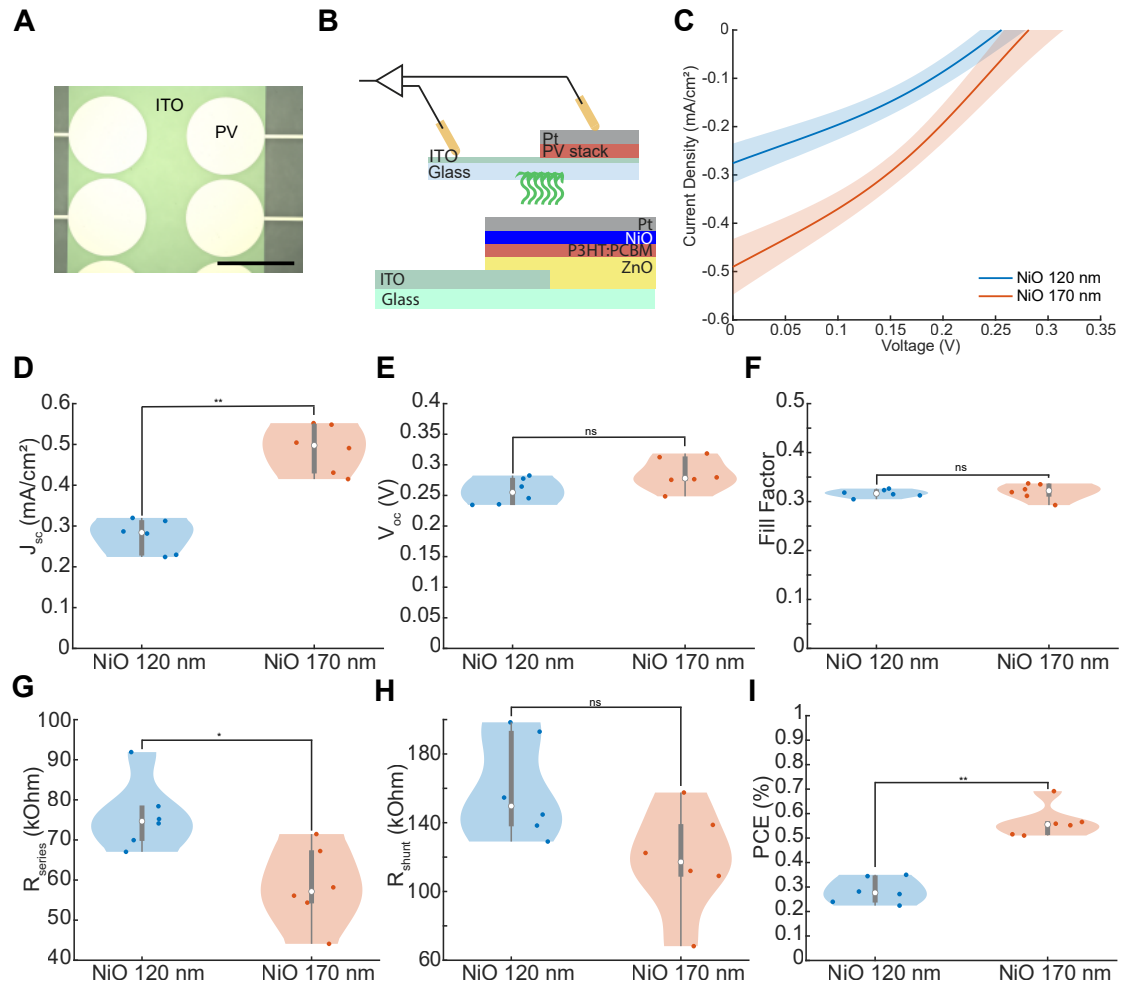
Figure 2.10: **Current density-voltage curves of photovoltaic pixels** A) A microscope image of the pixels atop the bottom ITO layer. B) The experimental set-up with 550 nm light (7.87 mW/cm^2) coming from bottom, through the ITO and onto the PV pixel. C) A JV curve (mean ± std) for NiO 120 nm (blue) and NiO 170 nm (orange). D-I) Violin plots of short-circuit current (J_{sc}), open-circuit voltage (V_{oc}), fill factor, series resistance (R_{series}), shunt resistance (R_{shunt}) and peak conversion efficiency (PCE) for photovoltaic pixels with thin 120 nm (blue) and thick 170 nm (orange) NiO hole-transport layers. Vertical lines indicate the interquartile range and medians are indicated by a white circle. n = 4, 6, 6 electrodes for each group respectively.

2.4 Summary and Discussion

Summary

This chapter demonstrated the successful fabrication of inverted P3HT:PCBM photovoltaic pixels on glass substrates, incorporating materials previously unexplored for use in microfabricating neural implants. The electron transport layer (ZnO) proved indispensable for device performance, while the replacement of PEDOT:PSS with NiO significantly improved fabrica-

tion robustness. Component analysis highlighted the role of NiO in enhancing charge delivery. IrOx was found to be a superior electrode coating compared to TiN. Design optimization with the updated reference electrode enables accurate performance characterization in vivo while the JV curves were essential for understanding device behaviour, determining power conversion efficiency and guiding improvements. These findings underscore the critical influence of material selection, interfaces, and component design on photovoltaic pixel performance within physiological environments.

Material selection for neural implants

P3HT:PCBM is a ubiquitous donor-acceptor combination that, while out of favour in recent years[91], holds an abundance of literature exploring its mechanisms, interfacial characterizations, and performances with different transport layers[92]. With the expansive literature and having already been applied to the microfabrication of retinal implants, P3HT:PCBM represented the natural starting point for neural stimulation at large. Starting from the POLYRETINA[71] design, which uses a PEDOT:PSS electrode, P3HT:PCBM, and a top Ti/TiN electrode, several steps had to be taken for application to cortical stimulation. Critically, the retina is a thin layer, allowing implanted devices to be very close to the target cells. This proximity meant that even low-efficiency devices were sufficient for stimulation. While not previously characterized for efficiency, the POLYRETINA device delivered a photocurrent of less than 0.2 mA/cm^2 with 0.94 mW/mm^2 irradiance. Assuming a linear relationship with light irradiance, although not seen experimentally, the photocurrent remains very low compared to the fabricated devices of this chapter. In combination with the low photovoltage of 120 mV with a slow voltage decay, this power would not be sufficient to activate tissue spatially separated from the device. The cortex is thicker with a greater distance between implant and target cells, necessitating higher efficiency from stimulatory pixels to achieve the required charge densities for neural activation.

To achieve this higher efficiency using P3HT:PCBM devices, typically with an efficiency of 4-5%, a deeper exploration of solar cell literature was done. Several critical aspects had to be investigated for use with neural implants. The first main change was the inversion of the pixel, to use an inverted pixel design, to allow a high work function and thus low reactivity material as the top contact. Solar cells often use aluminium as the top electrode for conventional pixels but implanted aluminium leads to degradation. For inverted pixels, silver is a typical top contact for solar cells but is not suitable for implantable due to leaching with gold and platinum being more common materials for neural implants due to their biological stability. For compatibility with microfabrication equipment and use for neurostimulation, platinum was the most suitable and showed promise with the gold interlayer hindering performance compared to Pt by itself.

After inversion, ZnO was exploited successfully as the ETL above the ITO layer however the PEDOT:PSS showed remarkably poor adhesion to the P3HT:PCBM interface. PEDOT:PSS is

currently widely explored for many uses in bioelectronic interfaces and solar cells as well as being an impressive material itself. However, in this layered design, it failed to achieve a critical aspect of microfabrication: reliability. If a process cannot be undertaken without catastrophic failure, it is as good as no process at all. Delving into literature, many transition metal oxides have been explored. As this section was not designed as an exercise in chemistry, commercially available HTLs were the most logical avenue to explore. With NiO as the HTL, yield improved greatly but performance decreased.

It can be noted between Figure 2.8 and Figure 2.9, there was a decrease in all measured metrics despite the complete pixel and the NiO devices having the same material components and fabrication steps. However, this decrease in performance was not only seen with NiO. It was seen across the board in terms of fabricated pixels as time went on, with PEDOT:PSS or even replicating the POLYRETINA device. This will be further explored in Chapter 4 and linked to the steps involved in patterning the PV pixels where, despite intuition about the impermeability of metal layers, photolithography was damaging the device itself.

Measurement framework

This work established two distinct measurement frameworks, along with their associated fabrication processes, to systematically assess the developed photovoltaic pixels. The JV setup provides insights into pixel efficiency, highlighting factors like interfacial resistance and potential defects affecting static performance. JV analysis underscores the potential of fine-tuning transport layer thicknesses (as demonstrated with NiO) and manipulating interfacial properties for overall device optimization. This wealth of information, standard in the solar cell community, represents an area where neural photovoltaic implants lack, making it difficult to compare between devices and their photovoltaic properties.

Conversely, the PV/PC setup is crucial for understanding the dynamic performance relevant to neural stimulation applications and is typically done for photovoltaic neural devices. The updated reference electrode design explored in this chapter, in particular, offers a more physiologically accurate assessment of pixel behaviour compared to what was done previously. By including both the cathodic and anodic electrodes, the design allows for a full embodiment of the implanted system. If the two electrode openings are connected and the contact pads removed, it becomes the implanted device. Indeed, the shape and spacing of the anode and cathode would be modified for implantation but the idea remains the same. There is no reference wire when doing photovoltaic stimulation of neural tissue as the charges flow back to itself, as opposed to typical electrical stimulation where the grounding metal wire or screw is part of the system. This enhanced understanding enables targeted improvements addressing the unique requirements of the in vivo environment.

Fabricating green-sensitive photovoltaics

P3HT:PCBM set the foundational photoactive component around which this chapter explored various parameters, namely fabrication techniques and measurement techniques. The final efficiency was an order of magnitude below that commonly found in literature and, despite not being the primary focus of this chapter, represents a concerning starting point for iteration with other materials. However, it should be noted that solar cells are typically made for large areas and without precise patterning, converse to what is needed for the fabrication of neural implants. A large amount of stress is placed upon the materials during microfabrication, such as thermal cycling during photolithography, exposure to oxygen and solvents, and high energy plasma interactions during etching. The rigorous microfabrication process likely explains the decreased performance observed in the fabricated P3HT:PCBM pixels.

While initial testing utilized green light – the peak absorption range for P3HT:PCBM – this visible light spectrum has limited applicability for neural implants due to poor penetration through biological tissue. Near-infrared (NIR) light offers a compelling alternative: it boasts deeper tissue penetration and adheres to safety regulations for irradiance. However, an unforeseen performance degradation in fabricated pixels over time added unexpected urgency to the development of NIR-sensitive pixels. This accelerated the transition to devices beyond the limitations of the visible spectrum. By developing NIR-sensitive pixels, the project could leverage NIR's superior tissue interaction while simultaneously addressing the challenges posed by the degradation observed in the earlier designs.

Conclusion

This chapter laid the groundwork for assessing microfabricated, light-powered neurostimulation devices, highlighting the complex relationships between device architecture, material choices, and measurement strategies. While P3HT:PCBM served as a starting point, the focus should be on absorption in the near-infrared (NIR) spectrum to penetrate biological tissue, and robustness against the stresses of microfabrication processes.

Refining microfabrication techniques is crucial. Observed material degradation emphasizes the need for techniques that minimize damage to delicate photovoltaic layers. Strategies may include low-temperature processes, protective encapsulation, and optimized patterning for the small pixel dimensions required for neural stimulation. In vivo implant studies will be the ultimate proof of success by demonstrating stimulation efficacy.

3 In vivo electrical neurostimulation: defining performance targets for photovoltaic devices

Outline

This section details the in vivo experiments using electrical stimulation to establish the threshold current required for cortical activation, providing benchmarks for photovoltaic device performance.

Personal contribution

I designed the study, designed and fabricated devices, performed rodent surgeries and manipulations, conducted the experiments and analysed the data.

Acknowledgements

I would like to acknowledge the contribution of Eleonora Borda who fabricated the PI Optic-SELINE and OSTEmer implants used for the experiment and took images.

3.1 Background

3.1.1 The motor cortex

In humans, the motor cortex is primarily located in the precentral gyrus, a prominent ridge along the frontal lobe of the brain. This region is responsible for planning, controlling, and executing voluntary movements[93]. While mice also possess a dedicated motor cortex, its location is slightly shifted towards the anterior portion of their brain[94]. Despite this anatomical variation, the fundamental function of the motor cortex remains conserved across species. Both human and mouse motor cortices contain organized maps of the body, enabling the precise control of specific muscle groups, and serve as the origin point for the neural signals that ultimately drive movement (Figure 3.1).

The cortex is organized into six distinct layers, each with specific cell types and connections. In humans, the motor cortex is relatively thick, ranging from 2 to 3 mm[96], while in mice, it is significantly thinner, typically less than 1 mm[94]. This difference in thickness reflects the greater complexity and specialization of the human motor cortex, which enables fine motor control and complex movements. The target neurons for stimulation within the motor cortex are primarily located in layer V, which is situated approximately 1 - 1.5 mm deep in humans[97] and around 0.5 mm deep in mice[98]. The depth of the target area poses a challenge for neural implants, as optimal stimulation requires electrodes that can effectively reach it, with surface electrodes offering a less invasive but spatially separated option while penetrating electrodes provide direct access.

The output from the motor cortex, regardless of species, travels along the corticospinal tract within the spinal cord[99]. These pathways contain upper motor neurons, whose long axons project from the cortex down to various levels of the spinal cord (Figure 3.1A). Here, they form a single synapse with lower motor neurons located within the ventral horn of the spinal cord. Lower motor neurons, in turn, extend their axons out of the spinal cord through the peripheral nervous system, directly innervating individual muscle fibres. When a lower motor neuron receives a signal from the upper motor neuron, it releases the neurotransmitter acetylcholine at the neuromuscular junction. This chemical signal triggers a cascade of events within the muscle fibre, ultimately leading to muscle contraction and movement.

3.1.2 Electrical stimulation of the motor cortex

Electrical stimulation of the motor cortex in humans has a storied history with both therapeutic and research applications. Early pioneering work demonstrated that direct stimulation of the exposed motor cortex during neurosurgery could elicit muscle contractions in specific body regions[100], providing evidence for the topographical organization of this brain area. Direct electrical stimulation of the motor cortex in humans with implanted electrodes also has the potential to treat a range of disorders. While still primarily an investigational approach, this technique has shown promise in managing chronic pain[101]. By delivering precisely targeted

electrical stimulation to specific areas of the motor cortex, it is thought to disrupt abnormal pain-related signals and provide relief. Additionally, implanted electrodes in the motor cortex are being explored for their potential use in restoring movement function in individuals with paralysis, such as those resulting from spinal cord injury[102] or stroke[103]. The aim is to use the stimulation to bypass damaged neural pathways and help re-establish control over paralyzed muscles.

Motor cortex stimulation in mice provides a powerful way to validate the functional link between this brain region and muscle control. By targeting specific areas of the motor cortex with implanted electrodes, researchers can experimentally trigger muscle contractions in corresponding body parts. Observation of this evoked muscle activity serves as direct evidence that the correct region of the motor cortex has been stimulated. This technique has been instrumental in mapping the motor cortex[94], refining the understanding of how movements are encoded[104], and studying the effects of stimulation on motor learning[105]. Typical stimulation currents used in mice are on the order of microamperes, delivered through microelectrodes penetrating directly into the cortical tissue[106].

Epicortical stimulation of the mouse motor cortex involves placing electrodes directly on the surface of the brain, over the motor cortical region. This approach offers several advantages compared to traditional penetrating electrodes. It is a less invasive technique, reducing the risk of damage to underlying brain tissue. Second, epicortical electrodes can cover a larger surface area of the motor cortex, potentially enabling the activation of broader muscle groups or providing more nuanced control of movement patterns.

3.1.3 Setting the benchmark through electrical stimulation

While epicortical stimulation offers a less invasive way to study the mouse motor cortex, there is considerable variability in the electrode sizes and current thresholds used across different studies. Electrodes may range from individual discs to flexible arrays, and current amplitudes typically fall in the tens to hundreds of microamperes range[107]. Much of the existing research has prioritized mapping the motor cortex and understanding the effects of different stimulation patterns on movement, for experimental purposes thus also not appropriate for a chronic setting. As a result, there has been less emphasis on systematically determining the absolute minimum current thresholds necessary to elicit muscle activity with epicortical stimulation in mice.

This section thus prioritizes finding the minimum current thresholds using electrodes of the same material and designs that would be feasible for a photovoltaic implant with the aim of setting reasonable targets of charge to elicit cortical stimulation.
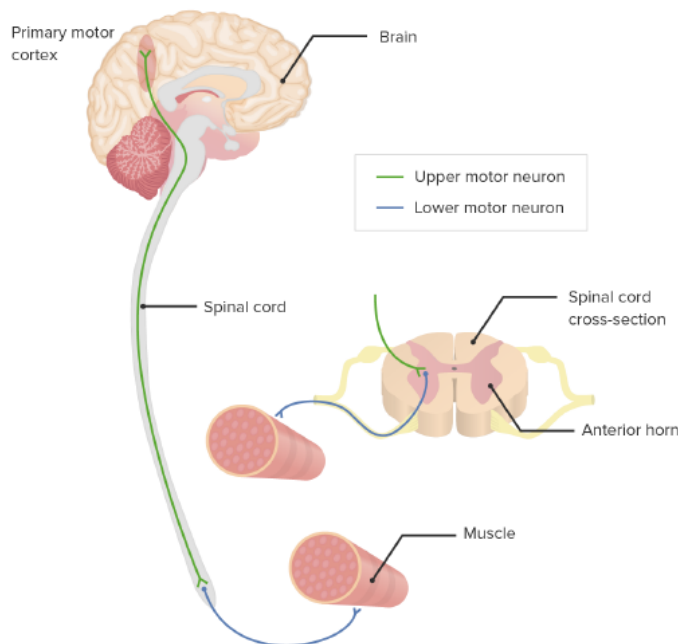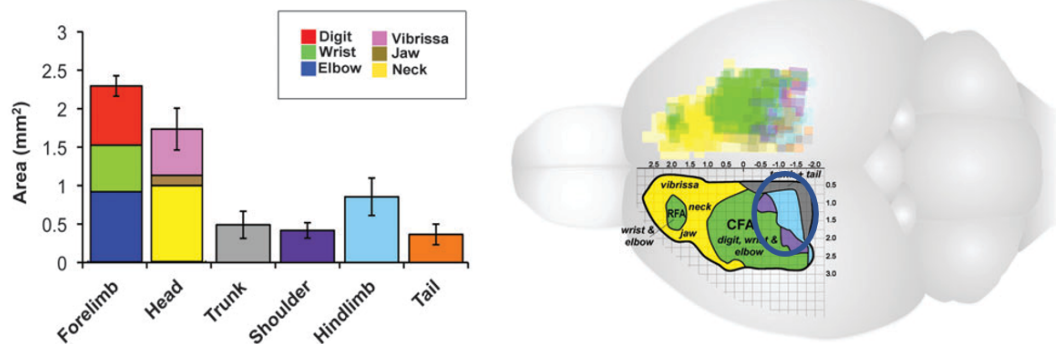
Figure 3.1: **Motor cortex organisation** A) The human motor cortex with the two neuron path from primary motor cortex to the muscle fibre. Adapted from the Lecturio website[95] B) Mouse motor cortex regions. Left - the area dedicated to different body parts. Right - localization of the regions on the mouse brain. The circle indicates the region for the hindlimb. Adapted from Tennant et al.[94]

3.2 Methods

3.2.1 OSTEmer μECoG array fabrication

Adapted from Borda, Medagoda et al.[108] OSTEMER 324 Flex (Mercene Labs) was prepared by mixing the two components in a 1.24:1 ratio. OSTEMER 324 Flex mix was spin-coated (nominal thickness = 30 μm, 1000 rpm, 60 s) onto 4-inch silicon (Si) wafers previously coated with a sacrificial layer in poly(4-styrene-sulfonic acid) (PSS; 561223, Sigma Aldrich). Thiol-ene photopolymerisation was performed under UV light in an exposure box (365 nm, 2 min; Gia-Tec). Photolithography was performed to pattern Pt as previously described. Electrodes (40 μm in diameter) and 30 μm wide feedlines with horseshoe shape (θ = 45°, W = 30 μm, R = 90 μm) were manufactured on the bottom layer. A 6 μm thick layer of OSTEMER 324 Flex was spin-coated for encapsulation onto the wafer treated with a short and low-power oxygen plasma (30 W, 30 s) and exposed to UV laser (375 nm, 800 mJ /cm^2) with a maskless aligner (MLA 150, Heidelberg). The OSTEMER 324 Flex layer was developed in ethyl l-lactate (77367, Sigma-Aldrich) for 210 s, rinsed in isopropanol and deionised water, dried with a nitrogen gun, and cured at 95 °C overnight. The metallization and OSTEMER 324 Flex encapsulation steps were repeated for the top layer. Multilayer OSTE+ μECoG arrays were then shaped by laser (10 J; WS Turret200, Optec Laser Systems) and released from the wafer by PSS dissolution in deionised water. After release, the multilayer OSTE+ μECoG arrays were inserted into a zero insertion force (ZIF) connector placed on a customised printed circuit board. Last, the electrodes were electroplated with platinum black (Pt-black), using a solution containing 1% of platinum chloride (H2PtCl6·6H2O), 0.01% of lead acetate (Pb(COOCH3)2·3H2O) and 0.0025% of hydrochloric acid (HCl). An LCR meter (4263 A, Hewlett Packard) was used for deposition at 800 mV and 100 Hz.

3.2.2 Flat opticSELINE fabrication

The Flat-OpticSELINE is a modified version of the OpticSELINE[89] without protruding wings. Therefore, it is equivalent to a transverse intrafascicular multichannel electrode (TIME) array. The Flat-OpticSELINE electrode array contains 8 CB electrode pairs fabricated with a 3D multilayer process. The detailed process flow is available in[109]. Briefly, a Ti/Al release layer (10/100 nm) was deposited using a magnetron sputter onto 4-inch Si wafers. The deposition of a PI layer (PI2611 HD MicroSystems GmbH) of 12 μm was obtained by spin-coating at 1000 rpm, soft-baking at 65 °C (5 min) and 95°C (5 min), as well as hard-baking at 200°C (1 hr) and 300°C (1 hr) both under nitrogen atmosphere.

The electrodes Ti/Pt (15/300 nm) were made by magnetron sputtering onto oxygen plasma-treated PI layers, followed by photolithography and chlorine-based dry etching. The central electrodes were 40 μm in diameter with 15-μm wide interconnects. After photoresist removal, the substrates were coated again with 6 μm of PI (2000 rpm), as just described. The metallisation and PI encapsulation were repeated for the top layer, with a PI thickness of 6 μm. A 14-μm

thick layer of positive photoresist was spin-coated and patterned by photolithography to open the electrodes and the pads for the connector in both layers. The PI layers were directionally dry-etched using oxygen plasma until the openings reached all the electrode layers (Pt was used as etch stop material). The remaining layer of photoresist was dissolved in acetone. The top layer electrodes had a 6-µm width ring shape, and 15 µm wide interconnects overlaid to the bottom ones. As before, the devices were then laser cut, released and electrodes coated in Pt-black.

3.2.3   PI µECoG array fabrication

For further investigation of motor cortex stimulation, tailored designs were then utilised. All designs followed the same process, differing only in electrode layout and laser shaping.

A Ti/Al (10nm, 100 nm) release layer was deposited on 4 -inch Si wafers. This was dehydrated and spin coated with a 4 µm PI layer (3000 rpm, 60 s) then soft-baked at 80°C for 5 mins and 100°C for 5 mins. After the soft bake, it was hard baked at 200°C for 1 hour and 300°C for 1 hour under nitrogen atmosphere. Photolithography was done with 2.5 µm AZ1512, baked at 110°C for 3 minutes then exposed with the maskless aligner (405 nm, 150 mJ/cm^2). The wafer was then coated with Ti/Pt (20 nm, 200 nm) deposited through magnetron sputtering (150 W, 100 W) and a lift off was done in acetone to define the electrodes, contacts and tracks (40 µm).

Another photolithography was done to define the area of a Ir-IrOx electrode coating (10 nm, 150 nm) deposited via magnetron sputtering (100 W, 150 W). Excess IrOx was removed via liftoff and a final encapsulation of 4 µm PI was spin coated atop the wafer and baked as before. A final photolithography step was done with 6 µm AZ10XT to define the electrode and contact opening sites and etched using RIE of oxygen plasma with the etch stop on Pt. A weak plasma (10 W) was required to avoid unwanted etching of the IrOx electrode coating. Finally, the devices were laser cut and released via anodic dissolution and placed in a ZIF connector for interface with the stimulator.

3.2.4   Animal handling

All experiments were conducted according to the animal authorisation GE132 approved by the Département de l'emploi, des affaires sociales et de la santé (DEAS), Direction générale de la santé de la République et Canton de Genève in Switzerland. All the experiments were carried out during the day cycle. Experiments were performed in adult (> 1 month) C57BL/6J mice (Charles River Laboratories). Mice were kept in a 12 h day/night cycle with access to food and water ad libitum. White light (300 ± 50 lux) was present from 7 a.m. to 7 p.m., and red light (650–720 nm, 80–100 lux) from 7 p.m. to 7 a.m.

3.2.5   Acute surgery

Mice were anaesthetized with an intraperitoneal injection of ketamine (50 - 90 mg/kg) and xylazine (5 - 10 mg/kg), diluted in sterile saline solution. Analgesia was performed with subcutaneous injections of lidocaine (6 mg/kg) prior to incisions and artificial tears were placed on the eyes to prevent drying. Temperature was maintained at 37°C by a heating pad and the depth of anaesthesia was assessed with the pedal withdrawal reflex. The skin of the head and hindlimb were shaved, mice were placed in a stereotaxic frame, and the skin was opened to expose the skull. A craniotomy was performed to expose the left motor cortex, with the craniotomy adjusted for the size of the implant used. The implant was then placed on the cortex.

3.2.6   Acute motor cortex stimulation and EMG recording

Two intramuscular needles (working and reference) were inserted into the right gastrocnemius muscle with a ground needle placed subcutaneously in the contralateral back. EMG signals were amplified (BM623, Biomedica Mangoni), filtered (1 - 1000 Hz with 50 Hz notch) and digitalized (16,384 Hz). Stimulation was delivered by the electrode on the motor cortex, at approximately 1 mm caudal and 1 mm lateral of bregma. The return electrode was varied as given by the experiment, but remained an electrode on the surface of the brain. Pulses of cathodic-first bipolar current pulses were delivered to the motor cortex at a variety of pulse widths, amplitudes and frequencies with ten trials per condition at a repetition rate of 1 Hz. Final tests established a stimulation protocol of six 1 ms cathodic then 1 ms anodic phase pulses with a 3.5 ms interpulse phase to avoid overlap with the EMG response, reliably between 30 and 40 ms after initiation of the pulse train.

3.2.7   Data analysis and graphical representation

Data was analysed in MATLAB with detrending and a bandpass filter (10 - 1000 Hz). To obtain the EMG envelope, the full wave was rectified and smoothed using a root-mean-square over a 20 ms window. The integral of the EMG envelope (iEMG) was computed, quantifying total muscle activity and used to compare different current amplitudes tested. Current thresholds were defined as the minimum current amplitude required to produce an iEMG level above 3 times the noise level. These thresholds were then graphically represented as a function of their position in space in MATLAB.

3.2.8   Finite Element Analysis modelling

Simulations were performed in COMSOL Multiphysics 6.1 using a time-dependent electric current study with the AC/DC module. Electrodes were designed on simulated PaC encapsulation with 40 μm diameter Pt electrodes and placed at the interface of brain tissue and cerebrospinal fluid (CSF), mimicking a surface electrode array. A thin film of 5 μm PaC was the

substrate and another was the top encapsulation. Openings for the electrodes were taken as the electrodes, made of Pt.

Tissue	Thickness (mm)	Radius (mm)
Brain	5	5
CSF	2	5
PaC	0.01	1
Electrodes	Boundary	0.02

Table 3.1: **Geometrical parameters**

Two terminal current sources were selected on the boundaries of Pt electrodes with the given current and assessed after 1 ms for the voltage field and current streamlines. A ground was placed on the back surface of the modelled brain tissue.

Tissue	Conductivity (S/m)	Relative permittivity
Brain	0.559	80.1
CSF	2.11	88.9
PaC	10^{-16}	3.15
Pt	8.9×10^6	Inf

Table 3.2: **Electrical parameters**

3.3 Results

3.3.1 Establishing EMG response from cortical stimulation

The initial tests were conducted as part of a validation of a μECog device utilising an OSTEmer substrate and encapsulation[108] as part of validation for its capability as a neural interface. A OSTEmer μECoG was fabricated with 40 μm electrode sites coated in platinum black (Figure 3.2A-C). To reduce the width of the device, a multilayer design was utilised with electrodes being at a depth of either 6 μm or 12 μm from the implant surface (Figure 3.2C). The μECoG array was placed on the cortex of an anaesthetised mouse (Figure 3.2D) showing clear conformability of the device to the surface of the cortex with one electrode within the area of the motor cortex. This electrode was used to deliver bipolar electrical stimulation to elicit muscle contract assessed via electromyography (EMG) recordings in the mouse hindlimb (Figure 3.2E). EMG responses, from intramuscular needles in the contralateral gastrocnemius muscle, had increasing amplitude with increasing current intensity (Figure 3.2F) seen from the raw result. The linear envelope of the EMG signal was extracted to encompass complex muscular activation (Figure 3.2G).

After validation that cortical stimulation of the motor cortex through microelectrodes reliably elicited an EMG response, further investigation probed the current thresholds required for EMG activity. For increasing pulse width, from 2.5 ms to 10 ms, there was a decrease in the

current thresholds where the longer 10 ms pulse had a current threshold of 18 μA while the 5 ms pulse needed 20 μA and the 2.5 ms pulse needed 40 μA (Figure 3.2H).

Multiple pulses, maintaining a burst width of 27 ms to ensure no overlap with the EMG signal, were investigated. For 2.5 ms pulses, an increase in pulse number led to a decrease in the current threshold with a minimum of 11 μA required to elicit a clear EMG using 3 pulses (Figure 3.2I). This was also seen with 5 ms pulses where with two pulses, 12 μA was the current threshold (Figure 3.2J). When pushed further and compared, multiple pulses with a shorter pulse width led to the lowest current threshold achievable being 11 μA.
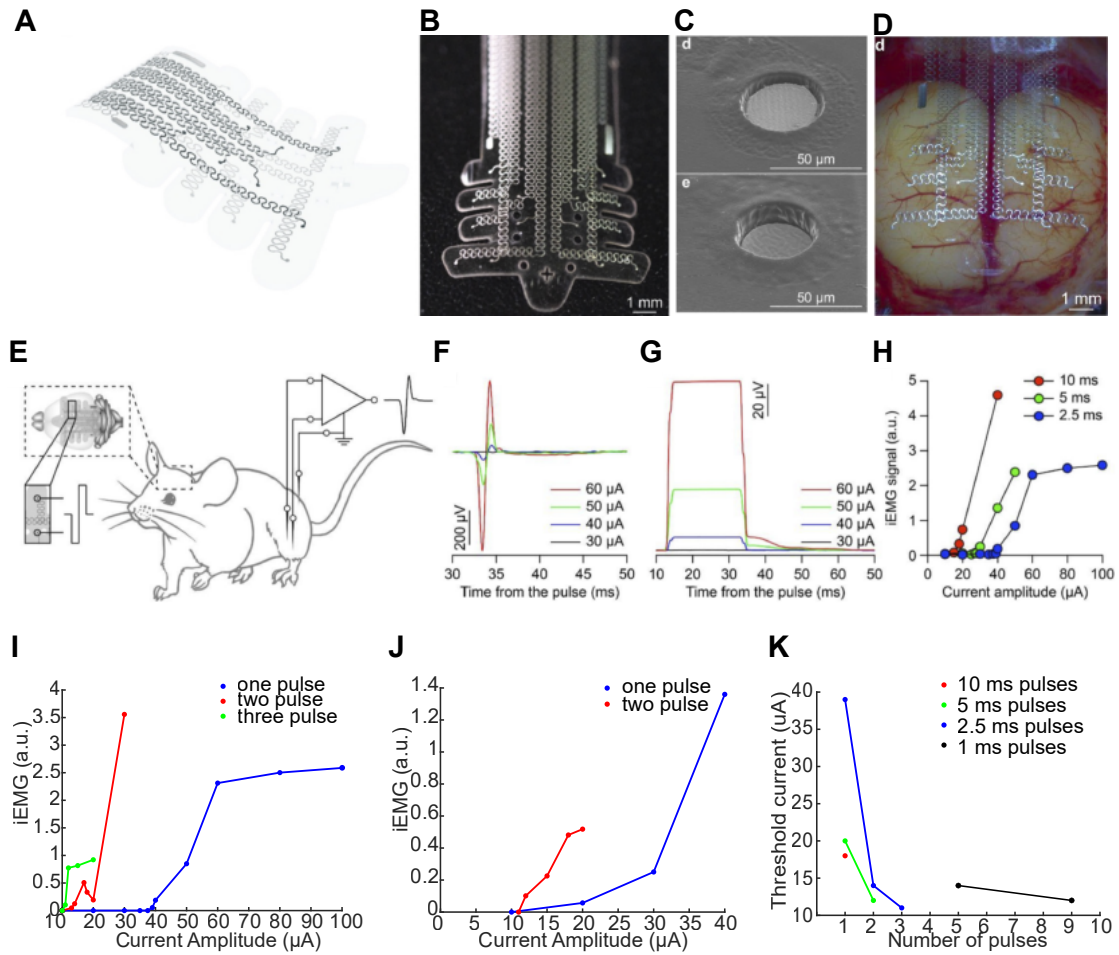
Figure 3.2: **Stimulation of the cortical hindlimb motor area with a OSTEmer µECoG** *(A) - (H) Adapted from Borda, Medagoda et al.*[108] A) Sketch of conformable multilayer OSTE+ µECoG array highlighting the bottom (black) and top (grey) electrode layers. B) Picture of the conformable multilayer OSTE+ µECoG array. C) Scanning electron microscopy images of 40 µm diameter top and bottom electrodes coated with Pt-black and encapsulated in OSTE+. D) Image of the array on the mouse cortex. E) Diagram of the stimulation set-up. A pair of electrodes in the µECoG array covering the cortical hindlimb motor area are selected for stimulation. Two needles are in the mouse hindlimb for EMG recordings. A third needle is the ground. F) EMG responses to increasing current amplitudes from 30 to 60 µA with a 2.5-ms long pulse. G) EMG envelope calculated using the root-mean square over a 20-ms sliding window from responses in (F). H) Quantification of the iEMG for 2.5 (blue), 5 (green) and 10 (red) ms pulses at increasing current amplitudes. I) Quantification of the iEMG from 2.5 ms pulses with one (blue), two (red) or three (green) pulses. J) Quantification of the iEMG from 5 ms pulses with one (blue) or two (red) pulses. K) Threshold current to elicit EMG activity for different pulse numbers for 1 ms (black), 2.5 ms (blue), 5 ms (green) and 10 ms (red).

3.3.2 Understanding the effect of a return electrode placement on threshold for cortical activation

With the establishment of this protocol in the mouse model, further investigation had to be done to determine an appropriate stimulation pattern, with defined stimulating and return electrodes. For a photovoltaic device, which is completely electrically isolated from any stimulation equipment, the placement of the electrodes can be freely defined but spatial resolution limits their spacing. Multiple configurations could be explored here with the return electrode closer or further from the working electrode, or having a local concentric return electrode surrounding. To investigate this, a device initially designed for optic nerve stimulation was adapted for use on the motor cortex.

The PI device (Figure 3.3A) was cut and placed on the mouse motor cortex (Figure 3.3B) as the OSTEmer µECoG. This device was a row of 40 µm electrodes with their own local concentric return electrode surrounding each electrode to limit current spreading. The first electrode was placed on the mouse motor cortex and the current threshold was investigated by comparing the local return and the most distant circular electrode, 1.12 mm away (Figure 3.3C). Delivering 40 µA with 3x 2.5 ms pulses produced a strong EMG response with the concentric return electrode (Figure 3.3D), producing a large iEMG envelope (Figure 3.3E). At lower currents, this response decreased resulting in a current threshold for the concentric return of 30 µA and the threshold for the distant return, similar to the layout with the OSTEmer µECoG, was 14 µA.

To investigate this further, several simulations were done to validate this result with different concentric configurations. In the case of two distinct and spaced electrodes, the current penetration is larger than the concentric return with the same dimensions as the in vivo experiments (Figure 3.3G, H), explaining the trend seen. When the centre electrode was maintained at the same size and the distance to the outer return was increased to 1 mm, the same spacing as the two circular electrodes, the current penetration was deeper into the tissue (Figure 3.3I) but still with less density than the two distant electrodes. This difference is further compounded by noting that the concentric return disperses the current across a larger 3-dimensional volume while the current is steered more directionally with the two electrodes.
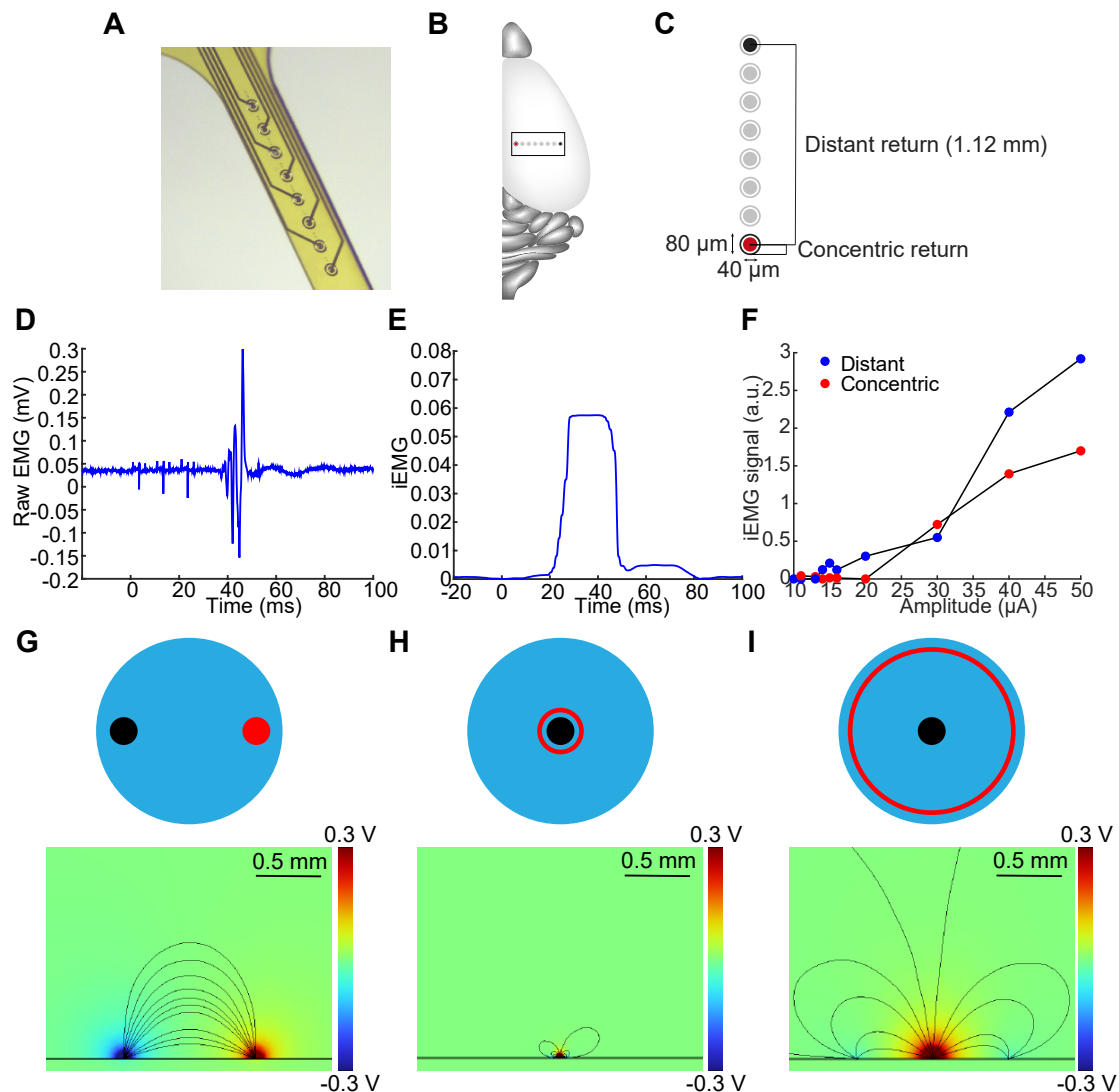
Figure 3.3: **Comparison of local concentric and distant return electrodes** A) The flat opticSE-LINE device used for stimulation.[110] B) Placement of the device on the mouse motor cortex. C) Electrodes tested with the stimulation electrode (red) and the local return and distant return (black). D) An EMG response from the local return electrode with 3 2.5 ms current pulses. E) The iEMG envelope extracted from (D). F) The iEMG signal for increasing current amplitudes. G) Simulation of current field lines in the brain from a 100 µA pulse with a 40 µm stimulating electrode and 40 µm return electrode with 1 mm pitch. wH) Simulation of current field lines in the brain with a 40 µm centre electrode and 10 µm-spaced, 10 µm wide concentric return. H) Simulation of current field lines in the brain with a 40 µm centre electrode and 1 mm-spaced, 10 µm wide concentric return.

3.3.3 Mimicking a PV-like device used for cortical stimulation

From here, more specialised investigation was done with designs more reminiscent of what was used in the photovoltaic pixel characterization and simulations. A smaller electrode, designed as the cathode and stimulating electrode, of 20 µm was used as stimulation and a larger 80 µm electrode as the return electrode, 1 mm away (Figure 3.4A). This was placed on the motor cortex then and each larger electrode was probed as the current threshold for EMG response (Figure 3.4B). Stimulation was with six 1 ms cathodic-first biphasic pulses with a 3.5 ms interpulse phase and the minimum current required to elicit an EMG response was determined.

With the first mouse (Figure 3.4C), a clear directional preference was seen with the lowest current threshold being 32 µA when the return electrode was caudal to the stimulation electrode. This was further probed on another animal where, for a similar current threshold, a dorsally and laterally located return electrode had the lowest current threshold. This was done by moving the µECoG to have different locations of the return electrode.
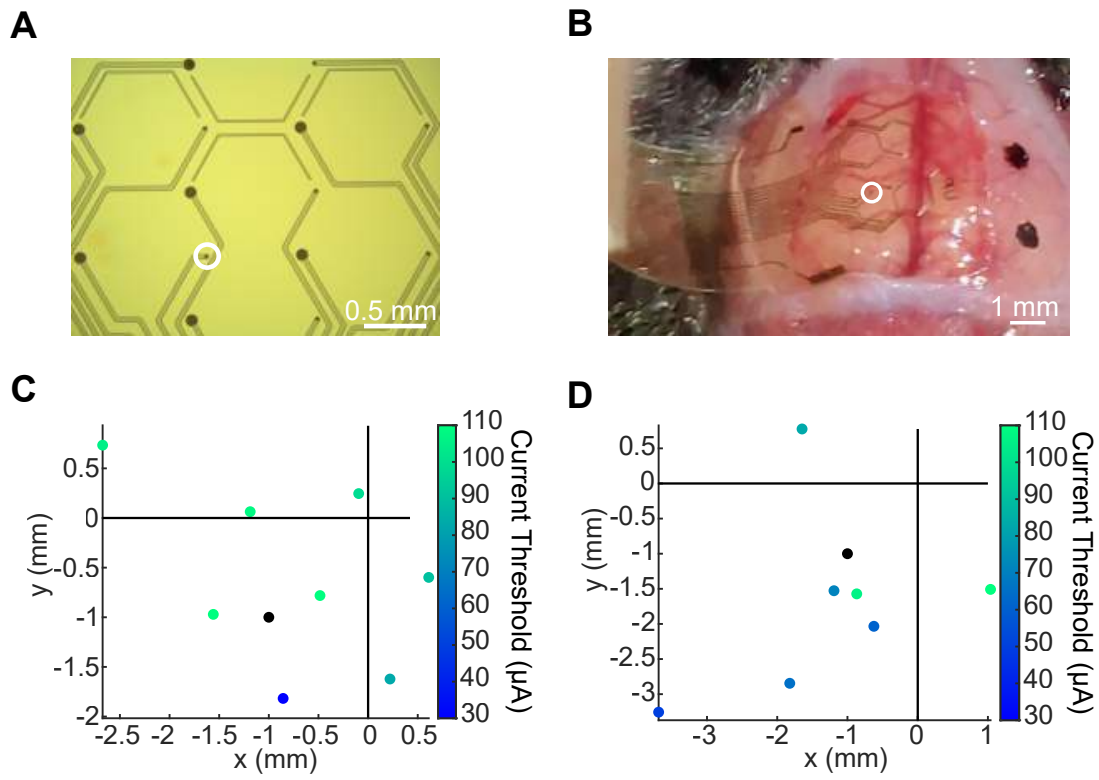
Figure 3.4: **Current thresholds for different return electrode placements** A) A PI ECoG with IrOx electrode coating. The circle shows the electrode used for stimulation. B) The ECoG on the mouse cortex with the white circle showing the same stimulating electrode. C) Current thresholds to elicit an EMG response for different return electrode locations with a fixed implant and stimulating electrode denoted by the black dot (n = 1). D) Current thresholds to elicit an EMG response for different return electrode locations with a moving implant for fixed stimulation electrode denoted as the black dot (n = 1).

3.3.4   Untangling the effect of distance and direction in motor cortex activation

This interesting behaviour led to a change in design to further define what dimensions the photovoltaic implant should take. Distance and direction of electrodes were separated by using a T-shaped design of return 80 μm electrodes and either a 20 μm or 40 μm stimulating electrode (Figure 3.5A). Electrodes were coated in IrOx, with Pt tracks and a PI substrate and their impedance was verified (Figure A.1). When placed on the mouse cortex, the stimulating electrode was placed at 1 mm left and 1 mm caudal from bregma and the long arm of the T parallel to the longitudinal fissure. As before, stimulation trains of six 1 ms cathodic-first biphasic pulses with a 3.5 ms interpulse phase were used to investigate the current thresholds for eliciting an EMG response.

When looking at the devices with a 20 μm stimulating electrode (Figure 3.5C), the minimum current threshold was 16 μA (median, n = 5) using the lateral return electrode 0.5 mm away

from the stimulation electrode. In general, the electrodes located laterally or caudally from the stimulation electrode had lower current thresholds than in the inverse direction. Closer electrodes also had the lowest current threshold compared to more distant however these were all below 35 µA. The trend, and the return electrode with the lowest current threshold, were maintained when looking at 40 µm stimulating electrodes (Figure 3.5D).

Despite a four-fold increase in electrode area, there was no difference in stimulation thresholds between the 20 and 40 µm centre electrodes. These were seen across all electrodes in the design (Figure 3.5E) where there was no significant difference in current threshold to elicit an EMG response between the 20 and 40 µm diameter electrodes. Thus, for these microelectrodes, current amplitude, not current density, was the dominating factor.

Platinum black was also investigated for its use in stimulating electrodes and, while the current threshold was low (Figure 3.5F), akin to that seen with the IrOx electrodes, this exceeded the charge injection threshold of these electrodes and delamination was seen on the electrodes after stimulation.
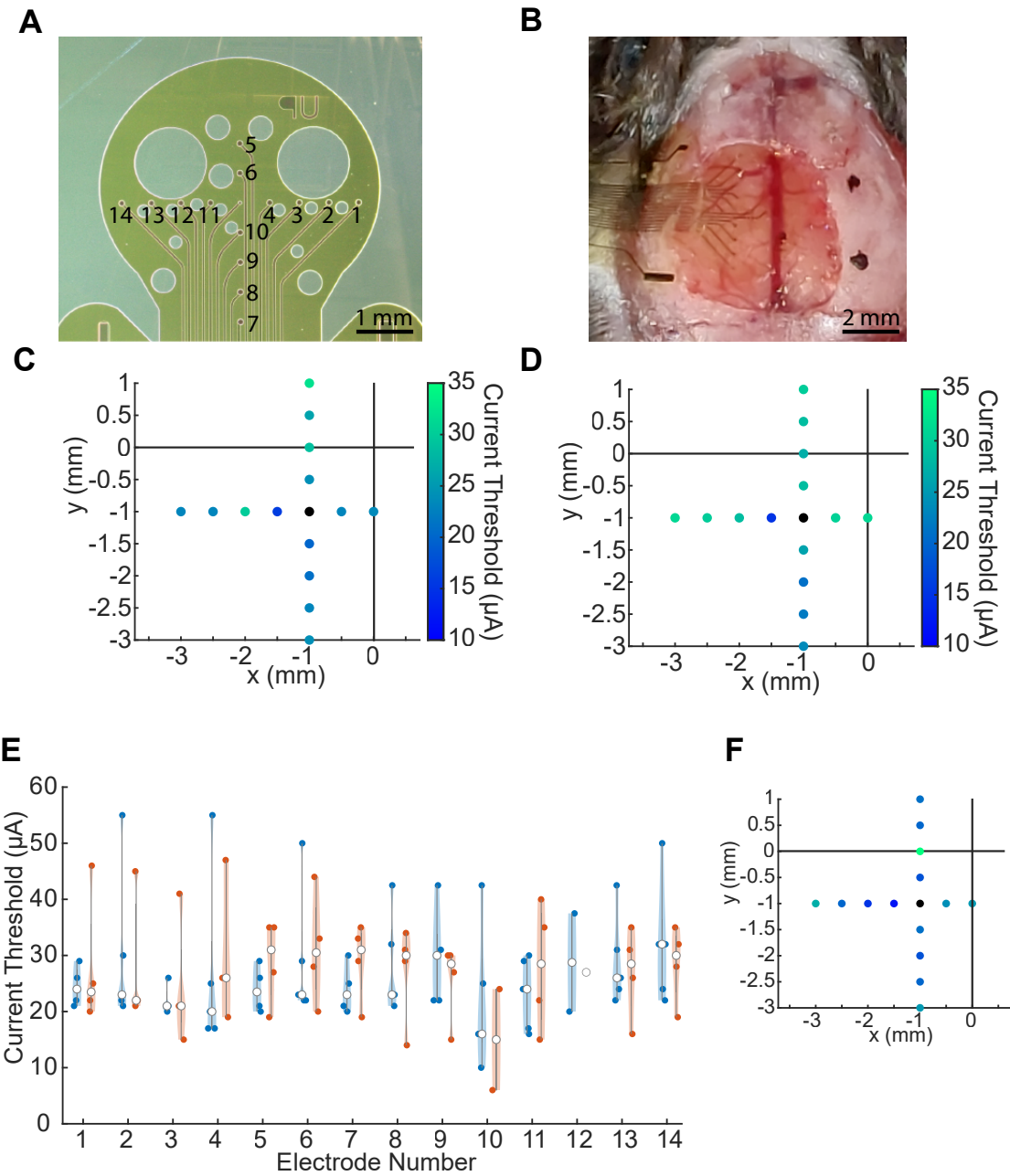
Figure 3.5: **Current thresholds for different distances and directions of return electrode** A) Image of the PI ECoG used for cortical stimulation. The centre electrode is the cathode and the outer electrodes (numbered 1 to 14) are the return electrodes. B) The ECoG on the surface of the mouse cortex. C) Median current threshold to elicit an EMG response from the 20 μm diameter centre electrode with IrOx electrode coating (n = 5). D) Median current threshold to elicit an EMG response from the 40 μm diameter centre electrode with IrOx electrode coating (n = 4) E) Current thresholds of all electrodes across all experiments for a 20 μm (blue) and 40 μm (orange) centre electrode. Vertical grey lines indicate the interquartile range and medians are indicated by a white circle. F) Median current threshold to elicit an EMG response from 20 μm diameter centre electrode with Pt black electrode coating (n = 1). The colour range is the same as C and D.

3.4   Summary and Discussion

Summary

These in vivo experiments provide essential insights for designing effective photovoltaic neural implants. Electrode configuration emerged as a crucial factor, with the placement and geometry of return electrodes profoundly influencing the efficiency of cortical stimulation.

Initial tests using an OSTEmer µECoG array demonstrated the ability to reliably elicit EMG responses in the mouse hindlimb via motor cortex stimulation. Shorter pulse widths (2.5 ms) required higher current thresholds compared to longer pulses and increasing the number of pulses within a burst further lowered the current threshold. To optimize electrode configuration, a modified optic nerve device with a local concentric return electrode was tested. A distant return configuration reduced the current threshold, compared to the concentric return, confirmed with simulations.

Further investigation with a specialized PV-like device revealed a directional preference for cortical stimulation. The return electrode's position relative to the stimulating electrode impacted the current threshold, with caudal or lateral placement consistently yielding lower thresholds. Finally, a T-shaped electrode array was used to systematically study the effects of distance and direction. Electrodes positioned laterally or caudally from the stimulating electrode generally required lower currents for activation. Proximity also played a role, with closer return electrodes achieving stimulation at lower thresholds. The lowest stimulation threshold of 16 µA was achieved using a 40 µm diameter centre electrode with the 80 µm return electrode positioned 0.5 mm away laterally. Surprisingly, a four-fold increase in the stimulating electrode's surface area did not significantly alter the current thresholds, suggesting that current amplitude, rather than density, was the primary factor for these microelectrodes.

Bipolar cortical stimulation

Consideration of the current path during stimulation of neural tissue is not a novel idea, with the placement of electrodes known to elicit varied responses. Cortical stimulation is typically achieved using a monopolar configuration, where the stimulating electrode is paired with a distant, large return electrode. To minimize the volume activated and stay within charge thresholds, penetrating electrodes are used to minimize the distance to the relevant area but come with increased tissue damage and foreign body response. While less common, bipolar stimulation, where the return electrode is placed in close proximity to the stimulating electrode, holds the potential to lower current thresholds and localised activation volume for neural activation[111]. This is fortunate for photovoltaic applications because the stimulation is naturally bipolar, as both the anode and cathode are defined by the PV itself.

With this in mind, this chapter focused exclusively on bipolar stimulation of the motor cortex to attain minimum current thresholds for activation to allow the best possible chances for

a PV for cortex activation. The directionality of the bipolar electrode placement was logical because, by maintaining both the stimulating and return electrode in the motor cortex, a large proportion of the delivered charge was maintained within the same cortical area. With an increase in charge delivered, the chances of activating the necessary neurons for an EMG response also increased. However, as seen with the higher threshold for the concentric return, this can be taken too far limiting the stimulation volume to such a degree that the charges are not capable of interacting with the necessary tissue.

This represents a trade-off between spatial selectivity and threshold current. Typically, this is not considered for exploratory electrically-controlled implants as stimulation systems can be tuned with ease with high voltage compliance. Conversely, photovoltaic implants, and single-junction implants as explored in this work, have a fixed voltage and the amount of current is proportional to the light intensity. Light is limited in terms of the source power and safety thresholds for tissue heating, so the PV implant needs to be placed and designed appropriately to activate cortical tissue within the irradiance limits available.

Current amplitude or density?

Perhaps the most interesting result was that between the 20 μm and 40 μm diameter electrodes, there was no change in current amplitude despite the current density being markedly different. This suggests that at this scale, for the tested stimulation parameters, total current delivery may be more important than spatially precise current density modulation. These insights could potentially simplify the design of photovoltaic pixels, where optimizing overall current output might take precedence over fine-tuning individual electrode geometries.

Alternatively, this finding could be related to the return electrode which was maintained at the same size, 80 μm in diameter, for both stimulating electrode sizes. This larger return electrode may effectively homogenize the current field, minimizing the influence of variations in the stimulating electrode's surface area. When taken together with the return electrode area, the ratio in total area is 0.85 between the smaller and larger stimulating electrodes. This difference may not have been detected from the relatively low number of in vivo experiments conducted.

Conclusion

These in vivo experiments lay a solid foundation for photovoltaic neural implants, highlighting the critical impact of electrode configuration, bipolar stimulation, and the relationship between current amplitude and density. This work emphasizes the unique advantages of bipolar stimulation for photovoltaic devices, given their inherent return electrode definition. The observed directional effects suggest that optimizing both electrode placement and geometry will be key to achieving localized and efficient stimulation within the constraints of photovoltaic pixels. Careful characterization under in vivo conditions will reveal how implant design influences realistic operation.

4 Fabrication and optimization of a near-infrared pixel for neurostimulation applications

Outline

Building upon the foundation of Chapter 2 and Chapter 3, this chapter sets about developing an implant appropriate for cortical stimulation sensitive in the near-infrared spectrum. It iterates several stages of optimization of the PV pixels, fabrication of a PV implant and preliminary testing with neural tissue.

Personal contribution

I designed the study, designed and fabricated devices, performed surgeries and rodent manipulations, conducted the experiments and conducted data analysis.

Acknowledgements

I acknowledge Martina Gini and Scott Erickson for their assistance in this section. MG fabricated and assessed the initial PDPP3T:PCBM and PDPP3T:ITIC pixels and modified the JV wafer design. SE developed, fabricated and handled the organoid system.

4.1 Background

Biological tissue is largely opaque to visible light, hindering the ability of light to enter and interact with photovoltaic devices. The near-infrared (NIR) window offers a unique opportunity for powering implanted photovoltaic devices (Figure 4.1). This window allows NIR light to penetrate deeper into biological tissues compared to visible wavelengths, potentially enabling the activation of photovoltaic implants beneath the skin[36]. Two windows exist dubbed NIR-I from 650 to 950 nm and NIR-II from 1000 to 1350 nm.
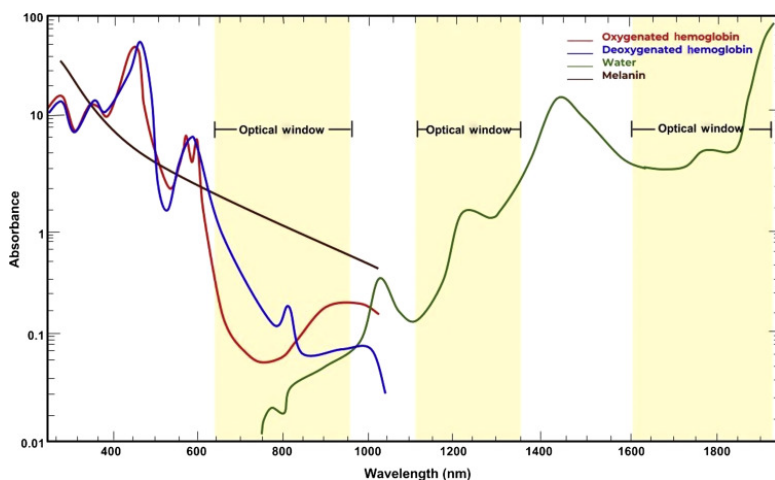
Figure 4.1: **Biological tissue window** Absorbance spectrum of blood, water and melanin. Adapted from[112]

4.1.1 NIR in tissues

The interaction of light with biological tissue depends on the wavelength of the light and the properties of the tissue itself. Two key factors influencing light penetration are absorption and scattering. Water, a major component of the body, strongly absorbs light across a wide range of wavelengths, particularly in the ultraviolet (UV) and infrared regions. However, within the NIR spectrum, between 650 and 1350 nm, water absorption is reduced significantly, creating a window where light can travel further into tissues[113]. Using a cadaveric model[114], light penetration into the skull was significantly higher for red 633 nm light transmission, with only 0.02% penetrating the skull, compared to near-infrared 830 nm light transmission, where 12% penetrated the skull.

The other major factor, scattering, refers to the deflection of light as it interacts with molecules and cellular structures within the tissue. While scattering reduces the overall intensity of light as it travels deeper, NIR light generally experiences less scattering compared to shorter wavelengths[113]. This combination of reduced absorption and scattering allows NIR light to penetrate tissues to depths of several centimetres, depending on the specific tissue type and

wavelength used.

The NIR window holds potential for various other medical applications. Techniques like near-infrared spectroscopy and functional near-infrared spectroscopy utilize NIR light to measure tissue oxygenation and blood flow. Furthermore, NIR light can be used for imaging applications. Techniques like photoacoustic imaging employ pulsed NIR light to generate sound waves within tissues. NIR light is also used in photobiomodulation and phototherapy for various purposes, including wound healing, pain reduction, inflammation management, and tissue regeneration[115].

4.1.2 Tissue safety limits

It is critical to consider light safety when working within the NIR window[112]. While NIR is less energetic than UV light, prolonged or high-intensity exposure can still cause thermal effects, so carefully calibrated power limits are essential for safe clinical applications.

Although not investigated for photovoltaic applications, NIR-I has been assessed for cancer treatment and photothermal therapy. In these use cases, a maximum permissible exposure of approximately 4 mW/mm^2 for 808 nm light per ANSI laser safety regulatory guidelines however this was applied for continuous exposures longer than 10 seconds. In the context of pulsed stimulation in the order of milliseconds, considerations have been made for duty cycle and pulse length with a correction factor allowing a change in this limit by an order of magnitude or more[116]. The subretinal PRIMA device, using 880 nm wavelength to restore artificial vision, considers a maximum of 8.25 mW/mm^2 for their ocular light source[117]. Due to the eye's sensitivity to light, safety limits for light exposure are stricter for the eyes compared to skin and other tissues so the safety limit for neural stimulation is likely higher.

4.1.3 NIR-sensitive organic solar cells

Solar cell engineering has focused, naturally, on achieving broad spectrum efficiency based on a standard irradiance of 1 mW/mm^2, known as AM1.5G (Figure 4.2). Various methods have resulted in single-junction organic solar cells achieving more than 20% efficiency[118]. The pursuit of NIR capabilities in organic solar cells stems from the desire to expand the range of harvestable solar energy, which extends significantly into the NIR region. By incorporating materials that absorb strongly in this range, NIR-sensitive OSCs have the potential to break traditional efficiency limits and achieve significantly higher performance[119].
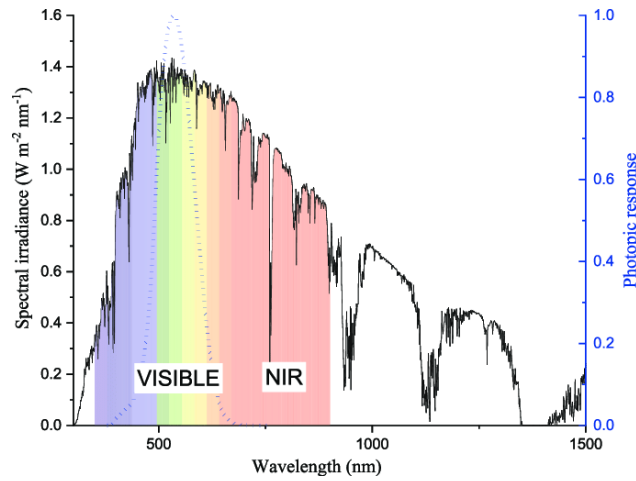
Figure 4.2: **AM1.5G Solar Spectrum** Standard irradiance used for solar cell characterization with the visible and NIR regions highlighted. The blue dotted line indicates the blue phototopic response. Adapted from[120]

4.1.4 Stability of organic PVs

Organic photovoltaics , with their promise of flexibility, processability, lightweight construction, and potential for low-cost manufacturing, hold significant potential for various applications. However, their operational stability remains a key challenge hindering widespread adoption[121]. Organic PVs are particularly sensitive to environmental factors including heat, oxygen, and water, which can significantly accelerate device degradation.

Elevated temperatures can induce morphological changes within the organic active layer. Semiconductors and polymers may undergo deformation or phase separation, affecting charge transport and exciton dissociation, ultimately reducing efficiency[122]. Additionally, thermal stress can lead to delamination at interfaces between different layers within the device structure. Many of the organic materials used in organic PVs are prone to oxidation[123]. The presence of oxygen can trigger photo-oxidation reactions, creating defects and altering the chemical structure of the active layer components. This oxidation process disrupts energy levels, hinders charge generation, and compromises overall device performance. Oxidative damage can also affect electrodes, impacting charge extraction. Water ingress into the device can be equally detrimental[124]. Moisture can interact with organic materials, causing swelling, hydrolysis, or promoting chemical reactions that degrade device components. Water can also accelerate the corrosion of electrodes, further reducing efficiency and durability.

Improving the stability of organic PVs is an active area of research. Encapsulation layers protect the device from oxygen and moisture. Materials like glass or specialized, flexible barrier films can significantly extend the device lifetime. Focus is placed on designing materials less susceptible to oxidation, hydrolysis, or thermally induced changes. Optimizing the arrangement of layers within the photovoltaic cell can also influence stability. For example,

incorporating protective layers or using more stable electrode materials can improve device resilience.

4.1.5   Encapsulating neural implants

Encapsulation materials for neural implants offer a tradeoff between water permeability and mechanical properties, with glass providing an ideal barrier at the cost of brittleness and rigidity, while polymers offer greater flexibility but weaker barrier properties. To improve the longevity of neural implants, sophisticated encapsulation techniques are crucial[125]. The integrity of the encapsulation layer is paramount, as even microscopic defects can serve as pathways for water ingress, accelerating device degradation. Researchers are continually refining deposition techniques and investigating new materials to create ultra-thin, biocompatible, and defect-free barrier layers that can withstand the mechanical stresses encountered within a biological environment.

For photovoltaic applications, the challenge of encapsulation is further compounded by the requirement for transparency to the specific wavelengths of light used for stimulation. This necessitates the use of specialized materials and deposition techniques that not only provide effective barrier properties but also maintain the optical properties essential for light transmission. Research into novel transparent encapsulation materials and techniques is ongoing, with the goal of developing robust, long-lasting solutions that can protect the delicate photovoltaic cells within neural implants from degradation while allowing for efficient light-induced stimulation.

4.1.6   Developing a photovoltaic pixel in the tissue transparency window

While traditional solar panels aim to maximize efficiency by absorbing the broadest possible range of the solar spectrum, photovoltaic stimulation of the cortex utilizes a specific, narrow range of light. This difference in approach stems from the distinct goals of each technology. Solar panels seek to convert as much solar energy as possible into electricity. In contrast, photovoltaic neurostimulation targets specific biological responses within neurons. Using a small range ensures precise control over the neural activation, minimizing unintended effects that could arise from stimulation with a broader spectrum of wavelengths. While near-infrared (NIR) photovoltaics have shown promise for retinal stimulation[74,126,127], advancements in their efficiency are necessary for the spatial and temporal requirements of cortical tissue.

This section focuses on using a NIR-absorbing organic donor layer, PDPP3T, to develop an efficient photovoltaic pixel for neural stimulation.

4.2 Methods

4.2.1 Semiconductor blend preparation

The photoactive materials were prepared under nitrogen atmosphere in the glovebox (MBraun, UNIlab pro). PDPP3T (M0991A1, Ossila), $PC_{71}BM$ (M114, Ossila), ITIC (M1011, Ossila) and Y6 (M2200A1, Ossila) were each dissolved in anhydrous chlorobenzene (99.85%, Sigma Aldrich) and stirred with a magnetic stirrer overnight at 70°C. When mixed with ITIC and $PC_{71}BM$, PDPP3T and the respective acceptor material was dissolved at 20 mg/mL. With Y6, this was reduced to 16 mg/mL after the Y6 ratio was adjusted. These solutions were then filtered (0.5 μm PTFE filter) and blended in at the given ratio to form a PDPP3T:acceptor solution and stirred at 70°C for a minimum of 4 hours.

4.2.2 Chip fabrication - Starting process

Slight modifications were made to the process used in Chapter 2 (Figure 4.3). These devices were specifically designed for current-voltage (JV) characterization to comprehensively assess the intra-pixel performance and the effectiveness of the chosen materials. The photovoltaic devices used for characterization were fabricated in a ISO5 to ISO 7 cleanroom (Neural Microsystems Platform, Campus Biotech, Geneva) on glass wafers. The plain wafers were rinsed in acetone, isopropanol (IPA) and DI water then dried and treated with O_2 plasma (2 minutes, 600 W - PiNK V10-G, Germany) to clean and activate the surface for the subsequent photolithographic process.

A 2.5 μm layer of photoresist (AZ1512, Microchemicals, Germany) was spin coated, baked (110°C, 90 seconds) and exposed (150 mJ/cm^2, 405 nm, MLA150, Heidelberg Instruments, Germany) and developed. Indium Tin Oxide (ITO) was sputtered using DC magnetron sputtering (nominal thickness 300 nm, 200 W, 2 sccm O_2, AC450CT, Alliance Concept, France). The wafer was then immersed in acetone, upside-down, in sonication (20 minutes, 80 kHz) to liftoff the ITO and rinsed in acetone, IPA and wafer then dried with nitrogen.

Following this, the photovoltaic pixel was layered upon this base ITO layer. The wafer was dehydrated for 10 minutes at 140°C then surface activated using O_2 plasma (30 s, 18 W, Diener Electronic, Germany) before being transferred to a nitrogen (N_2) atmosphere glovebox (MBraun, UNIlab pro). Zinc oxide (ZnO) nanoparticles (H-SZ51029, Genesink, France) were redispersed through sonication (37 kHz, 3 minutes) then spin coated (nominal thickness 30 nm, 1 mL, 2000 rpm, 45 s) and annealed (10 mins, 140°C). In an update to the previous process, the wafer was rinsed in IPA and DI water following annealing then briefly dried at 80°C and vacuum dried (20 minutes). The photoactive blend was spin coated (nominal thickness 90-100 nm, 360 μL) at 1000 rpm for 60s and annealed for 30 minutes at 115°C. The NiO nanoparticle solution was redispersed through sonication (37 kHz, 3 minutes) then spin coated (nominal thickness = 170 nm, 1 mL, 2000 rpm, 45 s) and annealed at 115°C for 30 minutes.

The top electrode of Pt (nominal thickness 200 nm) were sputtered at 100 W. The wafer was then dehydrated at 5 minutes at 80°C then coated with 1.5 μm of AZ1512 photoresist, patterned (100 mJ/cm^2) and developed. A reflow of 2 minutes at 120°C was done prior to ion-beam etching (IBE, Veeco Nexus IBE350) which removed all unprotected material. The etching was tracked using Secondary Ions Mass Spectroscopy (SIMS) and stopped after ITO etching was detected. To remove the remaining photoresist, oxygen reactive ion etching (Corial 210IL ICP-RIE) was done leaving the pixels of the photovoltaic stack patterned and exposed. The wafer was diced by hand using a diamond-tipped pen to obtain 19mm x 23 mm glass chips.
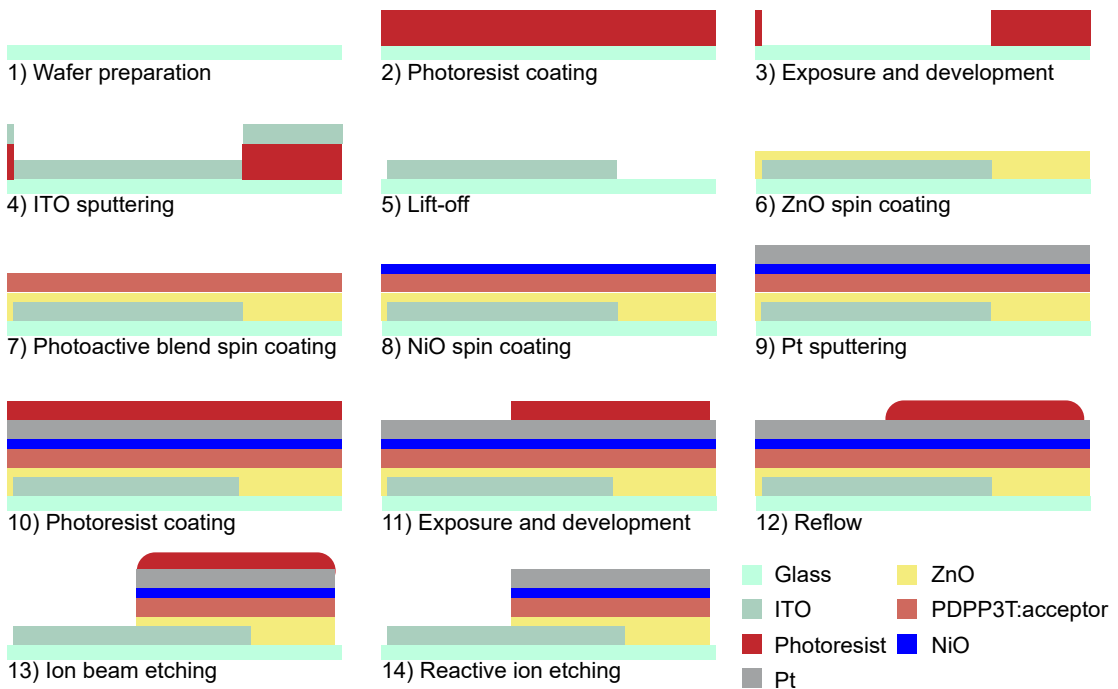
Figure 4.3: **Process flow - Original**

4.2.3   Chip fabrication - Pt contact update

In light of tests unveiling a variable ITO contact layer in the initial device architecture, the fabrication process was modified to incorporate platinum (Pt) as the new contact material (Figure 4.4). This change aimed to enhance batch uniformity and performance by leveraging the superior conductivity properties and reliable sputtering of Pt. The following sections detail the changes in the fabrication protocol, outlining the specific steps involved in depositing and patterning the Pt layer.

Wafer preparation was carried out as normal to clean the surface of the wafer. ITO was sputtered over the blank wafer (nominal thickness = 200 nm) and then photolithography was carried out. The wafer was dehydrated for 3 minutes at 110°C then coated with 1.5 μm of AZ1512 photoresist, patterned (100 mJ/cm^2) and developed. A reflow of 2 minutes at 120°C

was done prior to ion-beam etching (Veeco Nexuc IBE350) which removed all unprotected ITO leaving the window pattern. The remaining photoresist was stripped with acetone in sonication (5 minutes, 37 kHz) and the wafer was rinsed in acetone, IPA and DI water.

A 2.5 μm layer of photoresist was spin coated, baked, exposed (150 mJ/cm^2) and developed. A Ti adhesion layer then a Pt conductive layer was sputtered on the wafer (Ti = 15 nm, 150W and Pt = 150 nm, 100 W) after a brief Ar activation within the sputter chamber. The excess metal was removed through a lift-off process as done previously to leave a Pt border around each ITO window.

The photoactive layers, ZnO, PDPP3T:acceptor and NiO, were deposited as the standard process. The top Pt electrode was deposited and the whole PV pixel was patterned as before, with the IBE then oxygen reactive ion etching.
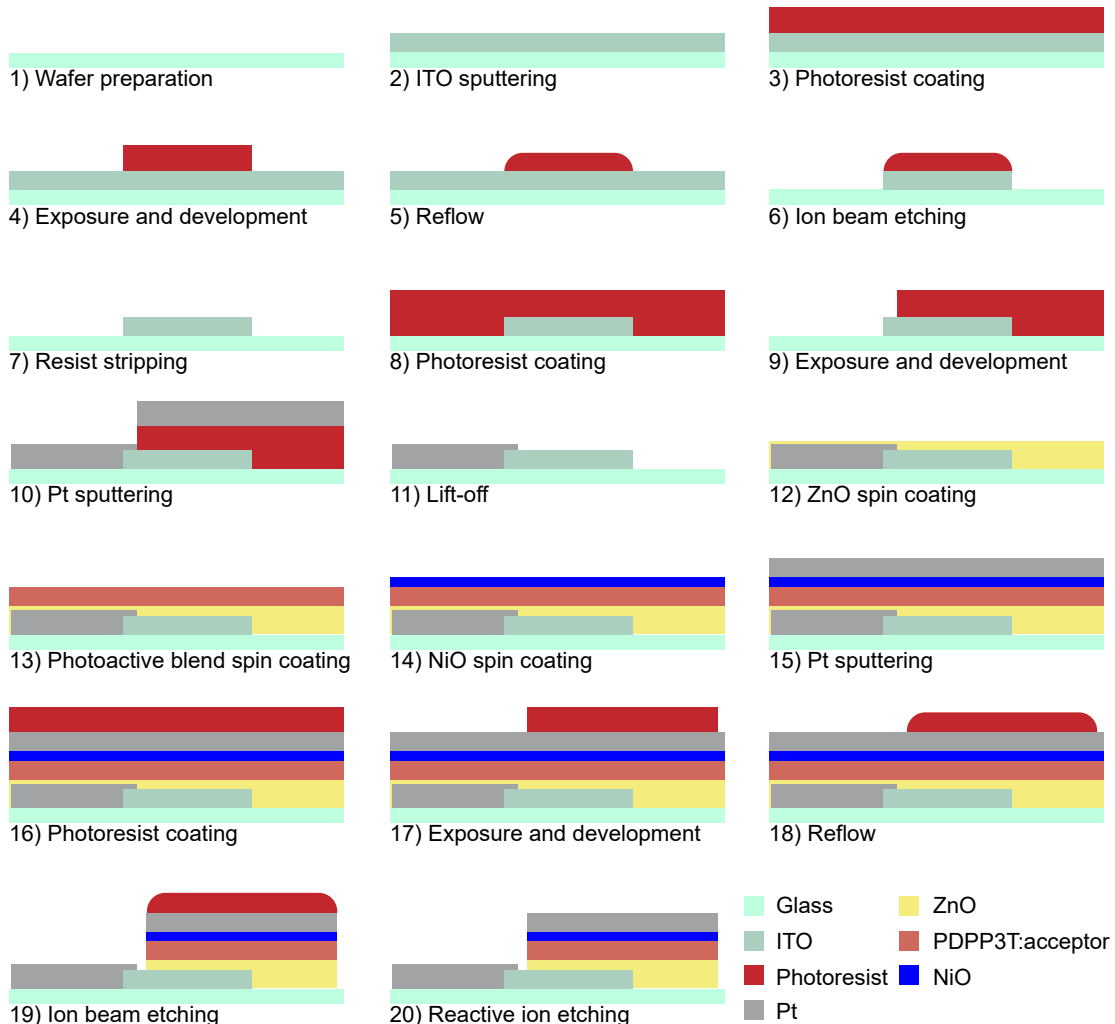
Figure 4.4: **Process flow - ITO window with Pt contact**

4.2.4   Chip fabrication - PaC protection update

To enhance the robustness and stability of the photovoltaic pixels during subsequent fabrication steps, a protective layer of Parylene C (PaC) was introduced prior to patterning the PV layer (Figure 4.5). The PaC layer serves as a conformal coating, providing chemical resistance and protecting the underlying layers from potential damage during photolithography steps.

All steps were as previously until the final photolithography step. After top Pt deposition, 5 µm of PaC encapsulated the wafer (Comelec C-30-S) using oxygen plasma and silanization (A174 silane) to improve adhesion. The wafer was dehydrated for 5 minutes at 80°C then coated with 1.5 µm of AZ1512 photoresist, patterned (100 mJ/cm^2), developed and underwent a reflow step. Using oxygen plasma RIE and the photoresist as a mask, the PaC was etched until the Pt layer. As both the photoresist and PaC etch at the same rate, this left a 1.5 µm layer of PaC as the mask for PV cell patterning. This was then etched using the IBE and the remaining PaC was removed with RIE leaving the contacts exposed.

4.2.5   MoO$_3$ deposition

MoO$_3$ was assessed as an improved HTL, replacing NiO$_2$ due to its detrimental effect on the series resistance, through deposition by sputtering or evaporation. MoO$_3$ was sputtered via RF magnetron (nominal thickness 20 nm, 150 W, AC450CT, Alliance Concept, France) In the case when MoO$_3$ (Kurt J, Lesker Company) was evaporated, 1 g pellets were placed in an evaporation boat (EVS31A005MO, Kurt J, Lesker Company) and evaporated (MBraun) to a thickness of 20 nm.

4.2.6   Measurement of JV behaviour

Pixels were measured kept at room temperature, in dry conditions in both dark and continuous light (peak emission = 860 nm, range = 800 - 900 nm, M850LP1 ThorLabs). The potentiostat (Compactstat, Ivium Technologies) applied a linear voltage sweep between -0.1 and +0.7 V with a 1 mV step and measured the output current from each pixel. The current was normalized to the area of the PV pixel. The V$_{oc}$ and J$_{sc}$ were extracted from the JV curves, FF and PCE were calculated as per equation 2.1 and 2.2. The series resistance was calculated as the tangential slope at the point of V$_{oc}$ and the shunt resistance was determined from the tangent at the J$_{sc}$ point.

1) Wafer preparation
2) ITO sputtering
3) Photoresist coating
4) Exposure and development
5) Reflow
6) Ion beam etching
7) Resist stripping
8) Photoresist coating
9) Exposure and development
10) Ti - Pt sputtering
11) Lift-off
12) ZnO spin coating
13) Photoactive blend spin coating
14) MoO₃ evaporation
15) Ti - Pt sputtering
16) PaC coating
17) Photoresist coating
18) Exposure and development
19) Reflow
20) Reactive ion etching
21) Ion beam etching
22) Reactive ion etching

Glass
ITO
Photoresist
Pt
ZnO
PDPP3T:acceptor
MoO₃
PaC
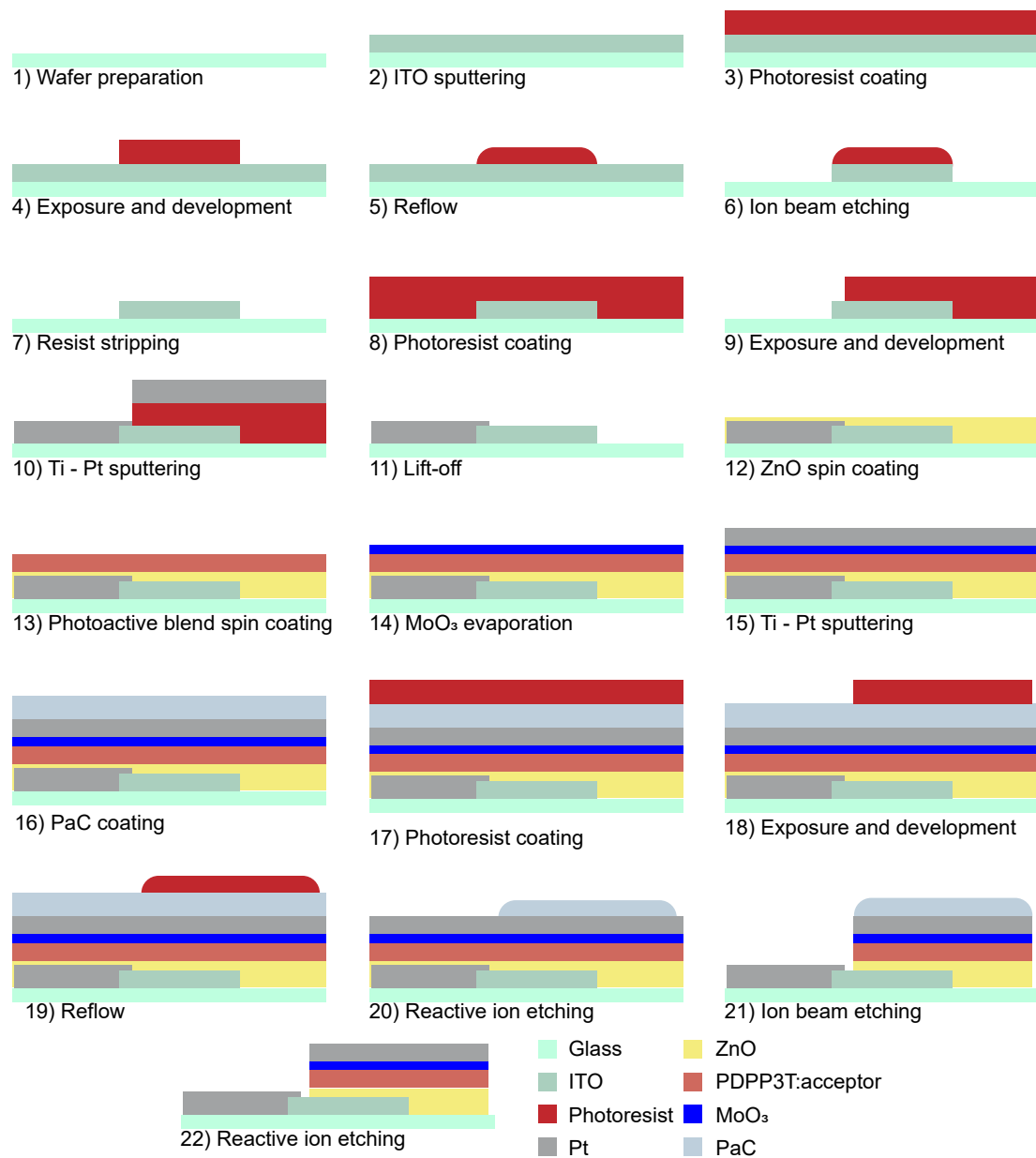
Figure 4.5: **Process flow - PaC protection**

4.2.7   Chip fabrication - PVPC with Pt support and PaC

These steps were incorporated into the process for fabrication of devices to measure pulsed behaviour (Figure 4.6). As explored in Chapter 2, the dynamic nature of the electrode-electrolyte interface is crucial for neural implants. To fabricate this, IrOx electrode coatings were included as well as a final encapsulation in PaC to define electrode openings that interact with the electrolyte solution.

As before, an ITO window and Pt support were patterned. To define the return electrode, Pt was also designed in the centre of each chip. A 2.5 µm layer of photoresist was spin coated, baked, exposed (150 mJ/cm^2) and developed. An Ir adhesion layer and an IrOx electrode coating were sputtered on the wafer (Ir = 10 nm, 100 W and IrOx = 150 nm, 100 W) after a brief Ar activation within the sputter chamber. The excess metal was removed through a lift-off process as done previously to an IrOx electrode coating on top of the return electrode.

The photoactive layers were deposited as before. A top electrode coating layer of Ir and IrOx was sputtered on top of the Pt (Ir = 10 nm, 100 W and IrOx = 150 nm, 100 W). The PaC layer was deposited, patterned, the PV etched then the excess PaC was removed to leave the PV pixels as hexagons atop the ITO windows.

Finally, the wafer was encapsulated in 5 µm PaC using oxygen plasma and silanization (A174 silane) to improve adhesion. To expose the electrodes and contacts, a final photolithography step was completed using 6 µm of AZ10XT photoresist as the mask for oxygen RIE. Remaining photoresist was stripped with further RIE. The wafer was diced by hand using a diamond-tipped pen to obtain glass chips and soaked in UV for 3 hours at 27.5 mW/cm^2. Devices were stored in nitrogen atmosphere when not in use.

4.2.8 Measurement of PVPC in solution

To measure these fabricated devices, a plastic reservoir was placed around the pixels above the encapsulation. It was adhered with clear silicone and cured for 1 hour at 60°C. The reservoir was then filled with 0.9% saline solution. Chips were placed in a holder and gold push pins were used to connect to each individual pixel via the contacts. An 850 nm light pulse from the LED (peak emission = 860 nm, range = 800 - 900 nm, M850LP1 ThorLabs) was controlled by a DAQ board (PCIe-6321, National Instruments) and the photovoltage and photocurrent were measured separately by connecting the appropriate amplifier (PV from DL Instruments Model 1201, PC from DL Instruments Model 1212). Data sampling was as 200 kHz to ensure the initial response of the PV was captured and light pulse trains were controlled by custom-made software. Data analysis was performed in MATLAB. Pixels were 1 mm hexagons with an electrode opening through the PaC. Measurements were all normalized to the area of the opening.

4.2.9 Roughness

The surface morphology was captured with Atomic Force Microscopy (AFM) (Dimension icon, Bruker, USA) using Scanasyst-Air silicon tip (k = 0.4 N/m, f_0 = 70 kHz, Bruker, USA). The process was interrupted at each layer deposition to allow the scan. The images obtained were analysed with Gwyddion software.
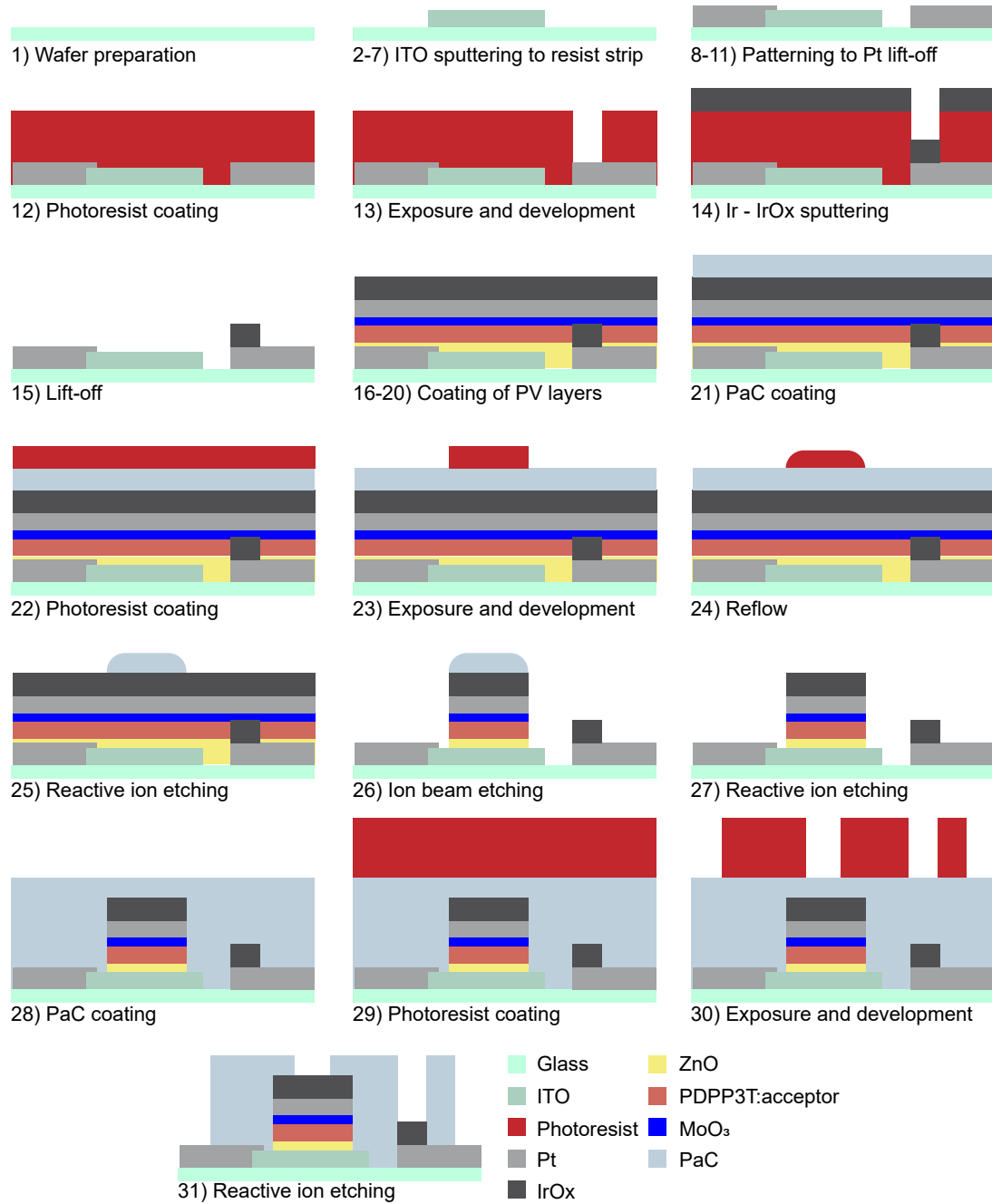
Figure 4.6: **Process flow - PVPC measurements**

4.2.10   Sheet resistance

Sheet resistance was measured using a four-point probe (R50 – 200 – 4PP, Filmetrics). Thirteen points around the wafer were measured and then averaged to obtain the sheet resistance of the thin film layer.

4.2.11   Transmittance

A transmittance spectrum was measured in the air between 300 and 1000 nm (F20-UV, Filmetics). Transparency was taken at 850 nm, the same wavelength as the available light source for all samples of sputtered ITO on glass.

4.2.12   Stability assessment

Modifications were carried out at a single step in the fabrication process for the PVPC devices. For plasma-activation, this was immediately before evaporation of MoO_3 using O_2-plasma (MBraun, 30 W, 30 s). For SiOx layer, this was the sputtering (150 W) 20 nm of SiOx prior to PaC encapsulation and was patterned using reactive ion etching in the same chamber as PaC etching using a CHF_3 chemistry for 45 seconds.

Measurements were conducted as in Section 4 at each relevant time point. For JV samples, chip was fully immersed in 37°C PBS then removed and dried before measurement. For pulsed light samples, the electrodes remained in 0.9% saline at RT for the duration of the experiment.

4.2.13   Implant fabrication

Previous characterization devices were fabricated on glass so for use as an in vivo implant, the process (Figure 4.7) had to include several adjustments compared to the PV/PC device fabrication. In Figure 4.7, the adhesion layers are also displayed.

The implant was built atop a Si carrier wafer where poly(4-styrenesulfonate) (PSS) was spin coated (2000 rpm, 45 secs) then baked for 10 minutes at 120°C. After cooling to room temperature, the 1 cm of outer edge of PSS was removed using DI water. The substrate layer of 5 μm PaC was deposited as usual then the surface was dehydrated for 5 minutes and O_2-plasma activated for 30 seconds prior to sputtering SiOx (20 nm, 100 W) and ITO (150 nm). This was then patterned via photolithography and ion beam etching as the previous processes. The same steps were followed as the previous process until the etching of the PV layers.

SiOx (20 nm, 150 W) was sputtered as an adhesion layer for PaC. After this, 5 μm PaC was deposited as usual. The electrode openings were made with reactive ion etching with O_2 chemistry for PaC and CHF_3 chemistry for SiOx. This was laser cut (WS Turret200, Optec Laser Systems) and released in DI water to dissolve the PSS. The release was done carefully to avoid the exposure of the top electrodes to DI water and avoid bending of the PV pixel.

1) Wafer preparation	2) PSS spin-coating and bake	3) PaC coating
4-9) Patterning SiOx-ITO via dry etch	10-13) Patterning Ti-Pt via lift off	14-17) Patterning Ir-IrOx via lift off
18-22) Coating PV layers	23-27) Protective PaC patterning	28-29) Etching
30-33) Patterning SiOx-PaC via etch	34) Laser cut	35) Release in DI water

Si wafer	Ti	ZnO
PSS	Pt	PDPP3T:acceptor
SiOx	Ir	MoO₃
ITO	IrOx	PaC
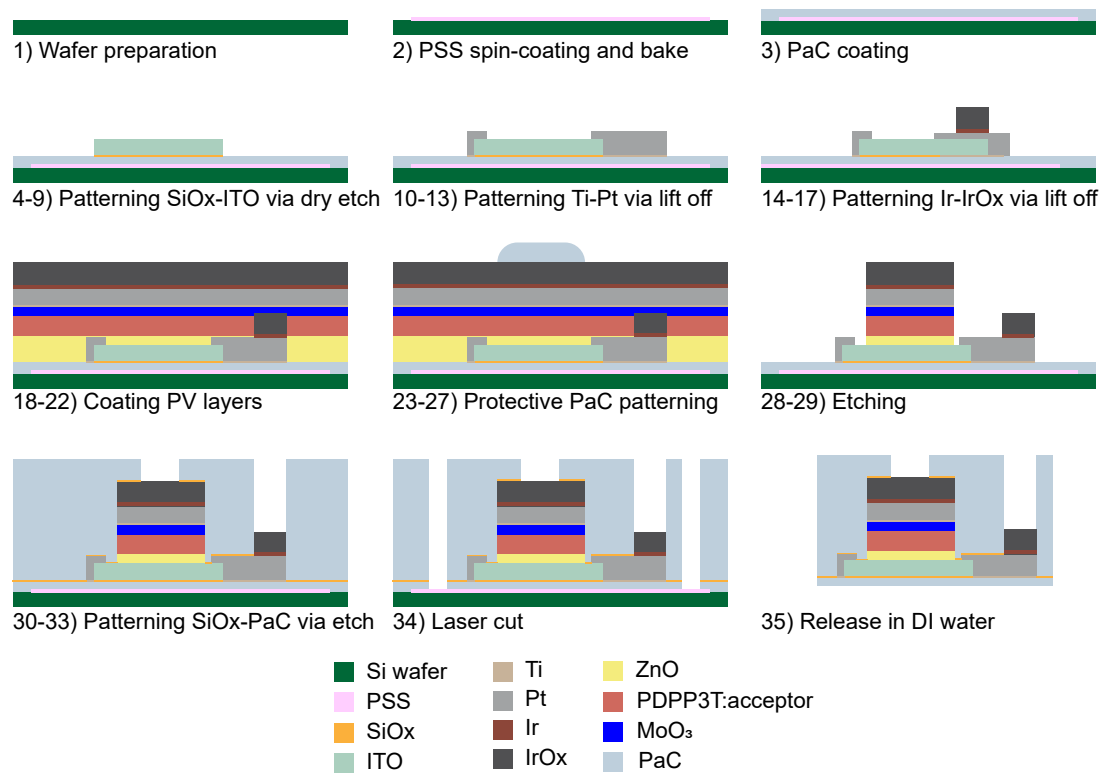
Figure 4.7: **Process flow - In vivo implants**

4.2.14   In vitro experiments on neural organoids

Initial experiments involved the model system using neural organoids[128] available from the Human Cellular Neuroscience Platform at Campus Biotech, Geneva. This model system allows for the study of neural activity in a controlled environment that mimics the complexity of brain tissue, providing a bridge between bench-top testing and in vivo experiments.

Seven-month old organoids were placed on a sterilized microelectrode array (MEA) specifically designed for the dimensions of the provided organoids. This was a 12 μm polyimide-based device with 30 μm diameter Pt electrodes. The MEA was placed in a custom-made holder for simultaneous organoid culture and electrical connection.

Organoids were cultured for 3 months prior to use with the PV implants and were adhered to the MEA at the time of use. A PV implant was placed atop a cultured organoid and set-up was placed in the incubator to maintain homeostatic conditions. Baseline recordings were taken without light to confirm recording quality. Light was delivered as 1 ms pulses at 5 Hz through a 600 μm inner diameter optical fibre (M53L01, ThorLabs) connected to NIR LED (peak emission = 860 nm, range = 800 - 875 nm, M850F2 ThorLabs). One end of the optical fibre was placed approximately 1-2 cm above the organoid at a direction 10-20° from vertical.

Following confirmation of the signal, increasing intensities of light were delivered to the maxi-

mum of 30.4 mW. Given the variability of placement and angle, a precise power density was not calculated and is reported as the full field power. Recordings were made through connection to a 32-channel recording head stage (RHD2132, Intan Technologies) in combination with the Intan field-programmable gate array (FPGA) and RHX software.

4.2.15   In vivo experiments

The fabrication process of the PI implant, animal handling and surgeries were carried out in an identical manner to Chapter 3. For PV experiments, the PV implant was placed with the cathode at 1 mm caudal and 1 mm lateral of bregma and the anode was positioned more laterally. A 600 μm diameter optical fibre connected to a NIR LED delivered light pulses (1 ms at 250 Hz for 6 pulses) directly above the PV pixel, 1 mm from the surface. These pulses were controlled via a PulsePal unit (Sanworks), and recordings were obtained as described in Chapter 3. When testing on muscle tissue, the leg muscle was exposed, the implant placed on top, and a single 1 ms light pulse was delivered while recording the EMG signal.

4.2.16   Statistical analysis and graphical representation

Data analysis and graphical representation were done in MATLAB. Normality was determined using the D'Agostino-Pearson's K2 test and a one-way ANOVA or Kruskal-Wallis test conducted between groups. In plots, p-values were reported as: $*p < 0.05$, $**p < 0.01$, $***p < 0.001$, and $****p < 0.0001$.

4.3   Results

4.3.1   Initial fabrication and acceptor layer optimization of a NIR-sensitive photovoltaic cell

With a peak absorption around 850 nm and a shoulder peak around 780 nm, PDPP3T was chosen as the candidate donor material for the NIR-sensitive photovoltaic cell (Figure 4.8A, C). This donor is commonly mixed with the gold-standard fullerene acceptor material $PC_{71}BM$, comparable to the $PC_{61}BM$ used with P3HT, to form a bulk heterojunction of PDPP3T:$PC_{71}BM$. To further explore the NIR capabilities of the pixel, newer non-fullerene acceptors (NFA) were also explored starting with ITIC as a pioneer NFA (Figure 4.8B). The absorption spectrum of the acceptor materials, $PC_{71}BM$ and ITIC, have peak absorption outside the NIR (Figure 4.8C,D) considered inconsequential given the minor contribution of acceptors to photocurrent generation.

As a baseline, the device configuration established with the green-sensitive pixel (Chaper 2) was maintained for the NIR pixel while changing the bulk heterojunction materials. This kept the ETL as ZnO, HTL as NiO (Figure 4.8E) and the electrodes as ITO and Pt and deemed reasonable given the comparable HOMO and LUMO levels of PDPP3T, $PC_{71}BM$ and ITIC

compared to P3HT and $PC_{61}BM$. A key design modification involved incorporating multiple pixel diameters on the same chip, with eight chips per wafer, to account for potential variability arising from the spin coating process (Figure 4.8F).
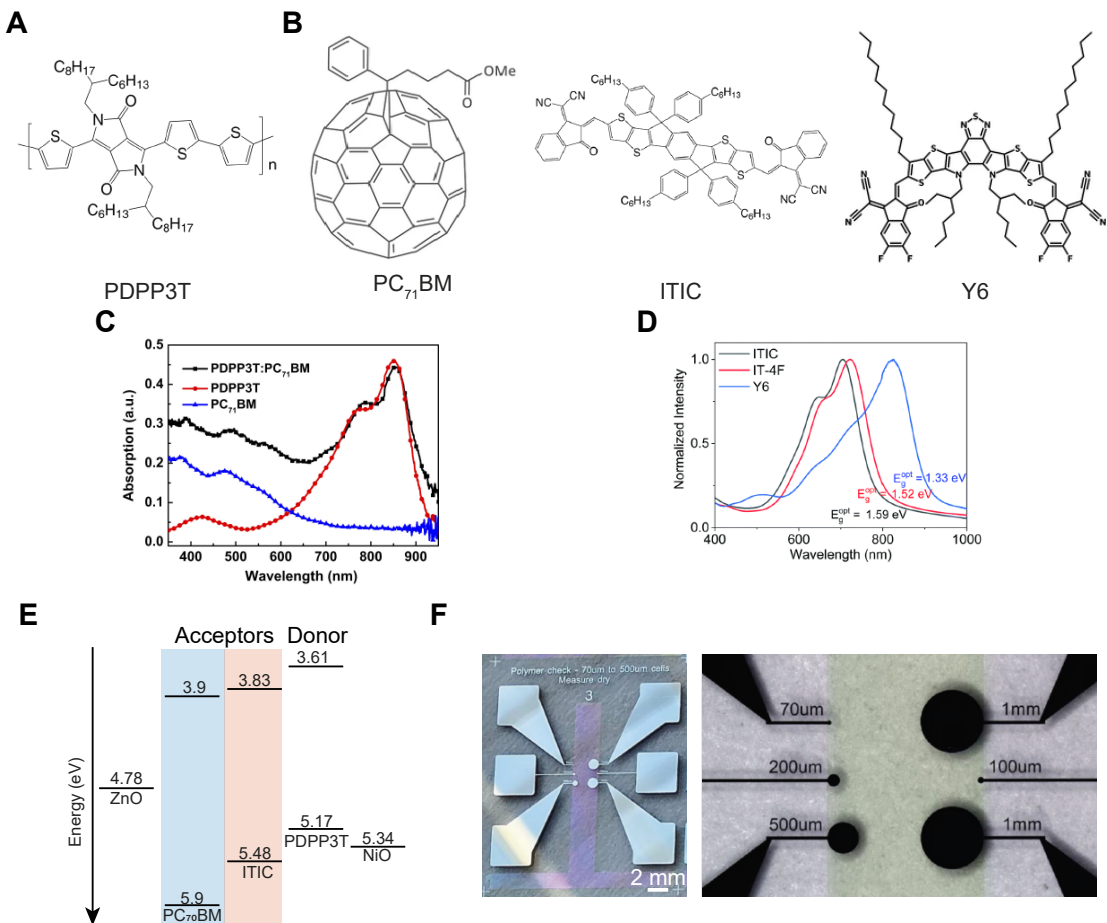
Figure 4.8: **Materials and design of a NIR-sensitive pixel** A) Chemical structure of the electron donor, PDPP3T B) Chemical structures of possible electron acceptors; $PC_{71}BM$, ITIC and Y6 C) Absorption spectrum of PDPP3T, $PC_{71}BM$ and their blend. Adapted from ([129]). D) Absorption spectrum of ITIC and Y6. Adapted from([130]). E) Energy band diagram of the electron-transport layer Zinc Oxide (ZnO),$PC_{71}BM$ (blue), ITIC (red), PDPP3T and the hole-transport layer Nickel Oxide (NiO). F) Left - Example of a fabricated chip with Pt top contacts and ITO bottom contacts with a 23 x 19 mm glass chip. Right - Photovoltaic pixels, where the top and bottom electrodes overlap, define the effective area of the pixels. Pixel diameters are next to their respective pixels.

These chips were designed to compare the performance of photovoltaic cells based on PDPP3T with either $PC_{71}BM$ or ITIC as the acceptor material. To assess performance, JV curves were measured from all devices while exposed to continuous light with 1 mm pixels being the main focus to judge performance between devices. With numerous unknowns in regard to handling and fabrication with these materials, a series of donor-to-acceptor ratios were tested based

on literature. For $PC_{71}BM$, these ratios were 1:2, 1:1 and 2:1 with the 1:1 ratio having the highest J_{sc} (median = 0.86 mA/cm^2), V_{oc} (median = 0.23 V) and PCE (median = 0.006%) (Figure 4.9B,D,E,I). When the acceptor was ITIC, the ratios were 1:1, 1:2 and 1:3 and the 1:2 and 1:3 ratios performed comparably and were both higher than the lower ratio of 1:1. For the 1:2, which provided the highest PCE, the J_{sc} was 2.67 mA/cm^2, V_{oc} was 0.63 V and PCE was 0.04% (Figure 4.9C,D,E,I).

While performing better overall, the fill factor of the ITIC-containing samples was significantly lower than those with $PC_{71}BM$ (Figure 4.9F). When seen in combination with the similar series and shunt resistances (Figure 4.9G,H), there were clear defects in the pixel design or fabrication leading to this shape of the curve (Figure 4.9C) and thus the low overall efficiency (Figure 4.9I).
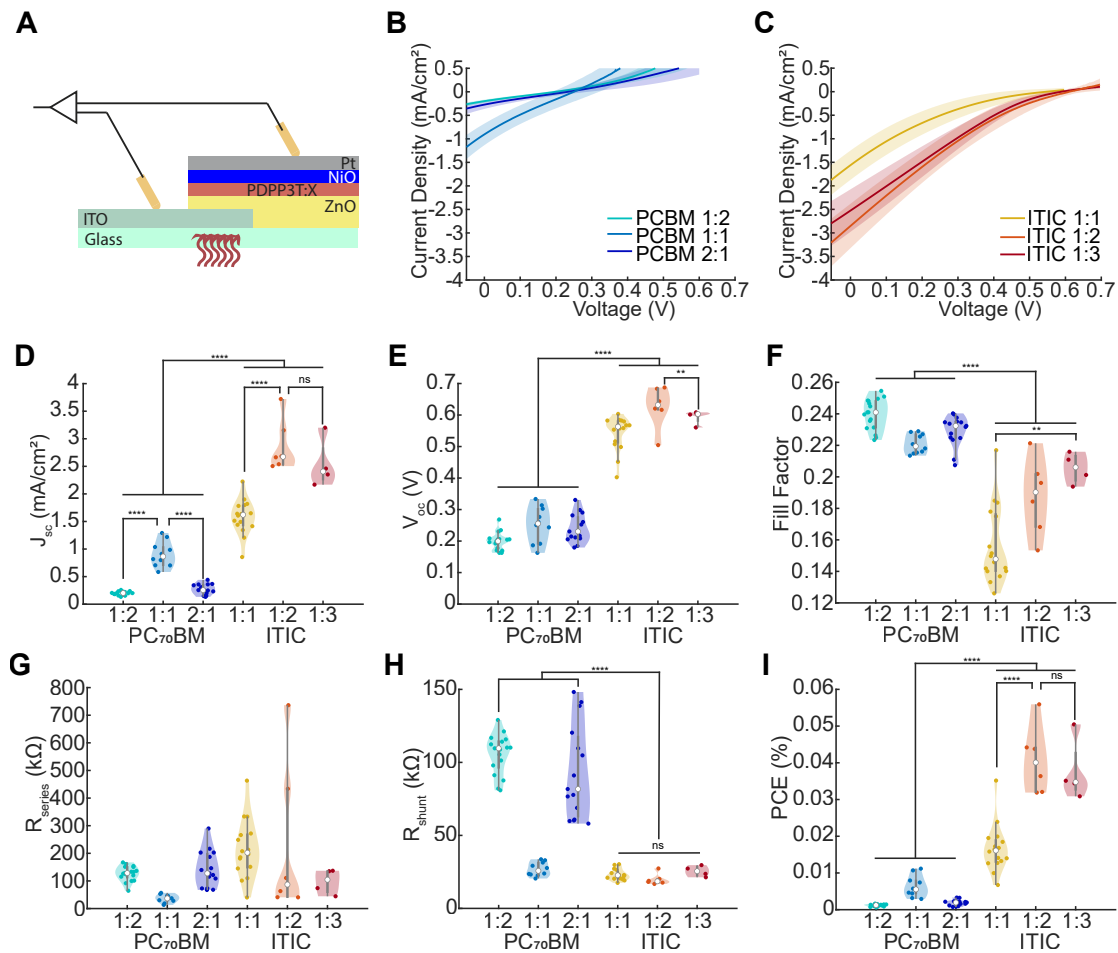
Figure 4.9: **Comparison of PDPP3T:PC$_{71}$BM and PCPP3T:ITIC photovoltaic pixels** A) Pixel configuration, with top Pt and bottom ITO electrodes, and varied electron acceptor layer. Pixels were exposed to continuous light (8.28 mW/mm^2), voltage was varied between -0.1 and 0.7 V and the resulting current measured. B) JV curves (mean ± std) of 1mm diameter PDPP3T:PC$_{71}$BM pixels with a donor:acceptor ratio of 1:2 (light blue, n = 17), 1:1 (steel blue, n = 10) and 2:1 (dark blue, n = 15). C) JV curves (mean ± std) of 1mm diameter PDPP3T:ITIC pixels with a donor:acceptor ratio of 1:1 (yellow, n = 16), 1:2 (orange, n = 7) and 1:3 (red, n = 4). D) J$_{sc}$ E) V$_{oc}$ F) Fill Factor G) R$_{series}$ H) R$_{shunt}$ and I) Power Conversion Efficiency for all 1 mm devices for both PDPP3T:PC$_{71}$BM and PDPP3T:ITIC pixels as violin plots. Vertical grey lines indicate the interquartile range and medians are indicated by a white circle.

4.3.2 Observation and adjustments due to low efficiency

To investigate this further, the morphology of the films was taken after deposition and annealing of each layer from ITO up to the HTL layer of NiO (Figure 4.10). ITO was sputtered on glass wafers and showed a uniform roughness of 1.39 nm (RMS) (Figure 4.10A). ZnO was then spin coated from a nanoparticle dispersion and annealed for a roughness of 4.27 nm, with recognisable nanoparticles in the film (Figure 4.10B). After spin coating of the PDPP3T:ITIC layer,

the roughness reduced to 1.79 nm as expected as spin coating planarized the wafer (Figure 4.10C). The uniformity and rigorous mixing of the bulk heterojunction were also confirmed by the low roughness of the layer with donor-acceptor domains in the tens of nanometers given by the darker and lighter regions. The spin coating of NiO from another nanoparticle solution increases the roughness to 4.275 nm with again small nanoparticles seen (Figure 4.10D). Small pinholes were present in the film in the range of the nanoparticle size (5 - 15 nm) however not at the scale that would suggest large parasitic pathways contributing to a poor series and shunt resistance and hindering PCE.
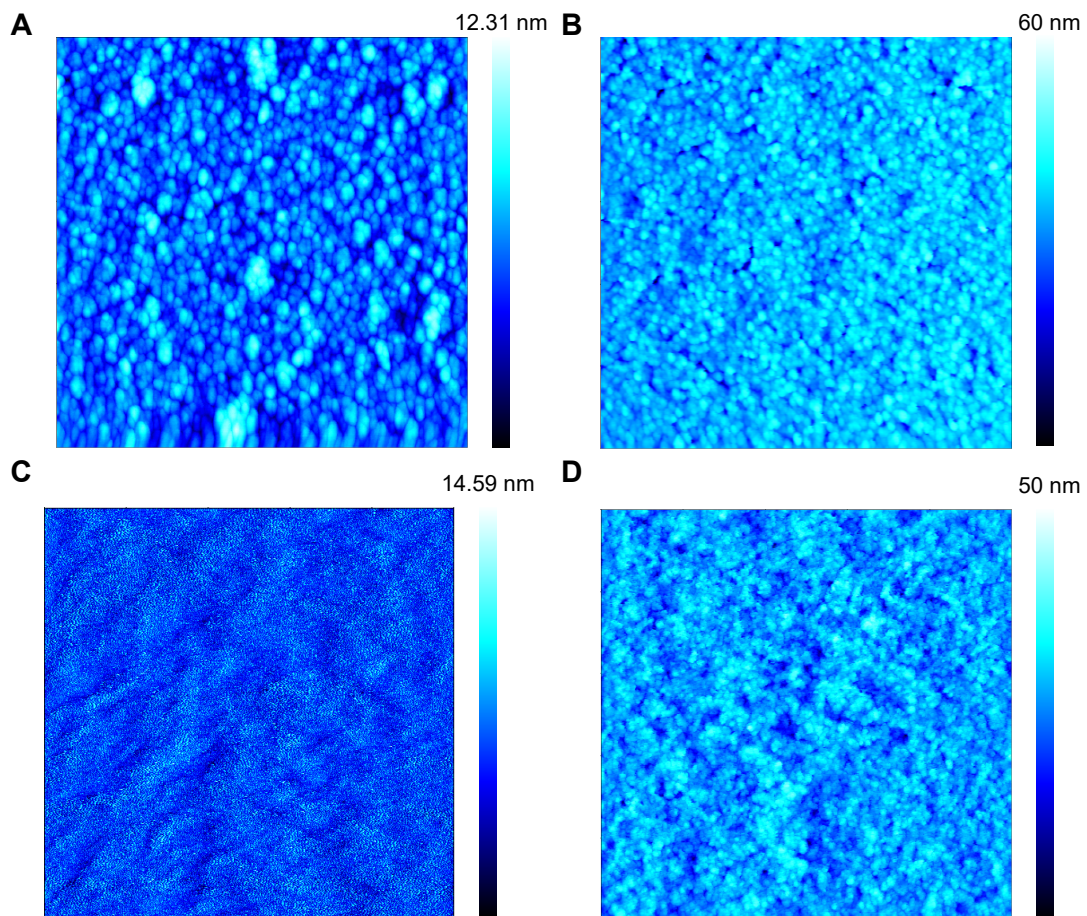
Figure 4.10: **Height scan by atomic force microscopy of relevant PV layers** A) Indium Tin Oxide B) Zinc Oxide C) PDPP3T:ITIC (1:2 ratio) D) Nickel Oxide. Colour bars indicate height at each point of the image with 0 being the minimum. All images are a 1 μm^2.

Further investigation into the source of this low efficiency brought the semiconductor ITO to the forefront. It was not only the transparent cathode, through which light can pass to activate the photovoltaic cell, but also the conductor that is interfaced with to measure the JV characteristics of the pixel (Figure 4.9F). During fabrication, it was commonly seen that wafers would have different colour hues (Figure 4.11A) so several wafers were discarded at this initial step due to poor transmittance of the film, even within the same batch of sputtered

wafers (Figure 4.11A (right)). This variability was further investigated over several months where reference wafers were measured for sheet resistance and transmittance to 850 nm light (Figure 4.11B). Despite coming from the same machine and sometimes on the same day, the sheet resistance varied wildly between 25 and 55 Ohm/square. This was after a filtering step that discarded wafers that had an unwanted colour hue. To mitigate the effects of these variabilities, a sputter recipe that maintained transparency for ITO was chosen as this could be easily judged. The resistive changes of the ITO were minimized by making the main conductor Pt for both the anode and cathode (Figure 4.11C) and only having an ITO window underneath the photovoltaic pixel (Figure 4.11D). As a metal with a high conductivity, Pt ensured that minimal series resistance was coming from the contacts.

To verify that this process did not negatively affect the pixels, a JV study was done between the two configurations. These wafers were inspected by eye for transparency. No adverse effects were seen on performance with the series resistance always lower and PCE slightly higher for wafers with the ITO window and Pt contacts (Figure 4.11E-J). This design allowed for higher resistance of ITO to contribute a fraction of the series resistance with 0.5 mm being the longest path that charges had to travel in ITO, compared to 14 mm in the previous design.
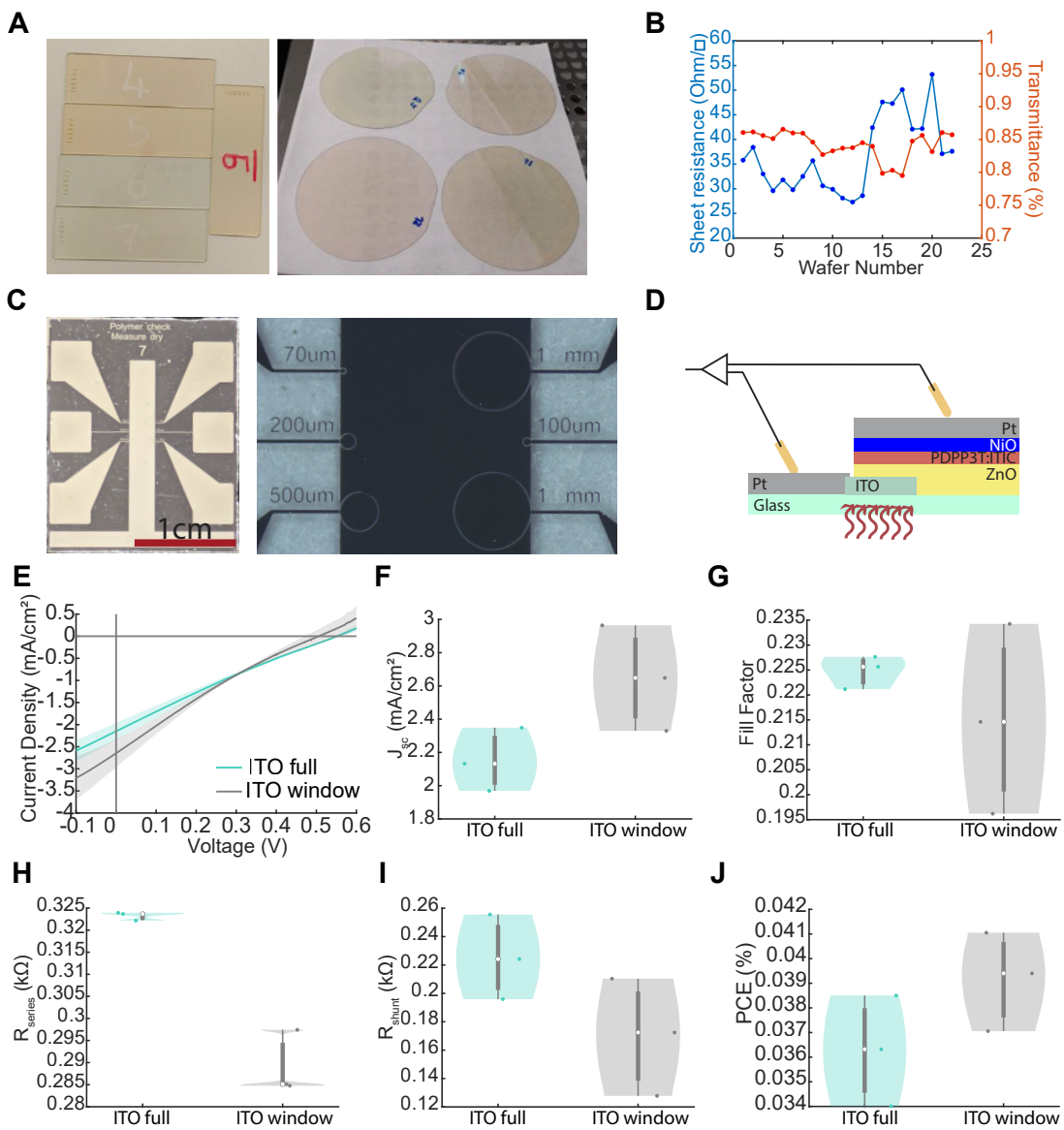
Figure 4.11: **Updated design of JV chips to account for ITO variability** A) Left - Glass slides sputtered with ITO with different chamber pressures and oxygen flows. Right - Glass wafers sputtered consecutively with the same chamber conditions. B) Sheet resistance (blue, left) and Transmittance to 850 nm (red, right) of 22 glass wafers sputtered with same chamber conditions over 3 months. C) Left - Example of a fabricated chip with Pt as both contacts. Right - Zoom onto PV pixels with sizes written on the chip. The outline of each chip is a 10 µm gap between the pixel and the Pt-ITO overlap. D) Pixel configuration, with an ITO window beneath the PV pixel and both contacts being Pt. Pixels were exposed to continuous light (7.36 mW/mm^2), voltage was varied between -0.1 and 0.7 V and the resulting current was measured. E) JV curves (mean ± std) of 1 mm pixels made with a full ITO bottom contact (blue, n = 3) or ITO window with Pt support (grey, n = 3). F) J_{sc} G) Fill Factor H) R_{series} I) R_{shunt} and J) Power Conversion Efficiency for all 1 mm devices for both ITO full and ITO window pixels as violin plots. Vertical grey lines indicate the interquartile range and medians are indicated by a white circle.

4.3.3   Further optimization of the acceptor layer

With this improved configuration, ITIC was compared to a newer NFA, Y6, which has a peak absorption in the NIR for more light harvesting from the applied LED. The BHJ of the PDPP3T:acceptor was maintained at the same ratio due to their similar molecular weights. As before, the 1 mm pixels have been chosen for comparison.

The pixels containing Y6 pixels had a significantly larger J_{sc} (Figure 4.12C, median = 2.47 mA/cm^2, n = 13 vs ITIC = 0.86 mA/cm^2, n = 13) while a marginally, but significantly, lower V_{oc} (Figure 4.12D, median = 0.47 V vs 0.40 V). The fill factor and series resistance also greatly improved although the shunt resistance was better for ITIC-containing cells (Figure 4.12E-G). In combination, this led to a larger efficiency with Y6 of 0.04% compared to 0.01% for ITIC (Figure 4.12H).

Notably, during fabrication, there were sporadic instances of catastrophic failure following development during photolithography to pattern the PV cells (Figure 4.13A). This penetration of the developer into the layers resulting in complete delamination indicated defects in the top sputtered Pt and IrOx allowing a strongly basic solution in contact with the organic layers themselves. In an effect to overcome this, an intermediate step was introduced to ensure the harsh solvents used during photolithographic patterning did not damage the PV itself. A layer of PaC was deposited over the entire wafer, this was patterned using a standard photoresist and developer, dry etched using oxygen plasma and the patterned PaC was used as a mask (Figure 4.13B)for the following steps to dry etch the PV cell with an ion beam.

With the inclusion of this step, both ITIC- and Y6-containing pixels improved in terms of J_{sc}, V_{oc}, R_{series} and PCE (Figure 4.13E,F,H,J). This represented a marked improvement in the fabrication of the pixels and allowed for analysis of the PV cell itself unhindered by the degradation caused by patterning. Hence, it was possible to accurately compare the ITIC and Y6 groups, considering only the protected (P) devices.

The J_{sc} for the Y6 group was more than three times larger than the ITIC group (Figure 4.13E), the V_{oc} was lower by 32 mV (Figure 4.13F)and the fill factor was the same (Figure 4.13G). The series resistance and shunt resistance of the Y6 pixels were significantly lower (Figure 4.13H,I) compared to the protected ITIC pixels. These relative changes resulted in an efficiency of 0.16% for the protected Y6 group (Figure 4.13J).
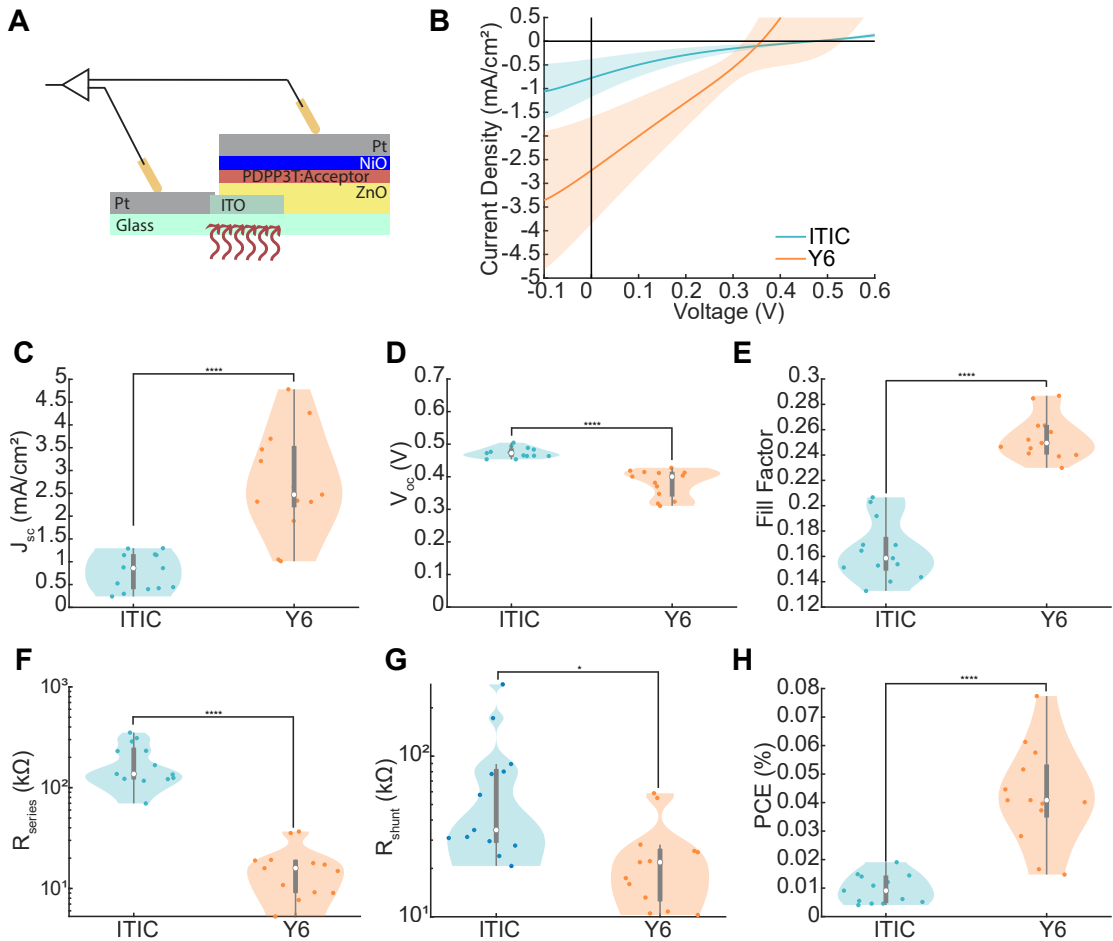
Figure 4.12: **Comparison of PDPP3T:ITIC and PCPP3T:Y6 photovoltaic pixels** A) Pixel configuration, with the updated design, and a test of acceptor layers. Pixels were exposed to continuous light (6.15 mW/mm^2), voltage was varied between -0.1 and 0.7 V and the resulting current measured. B) JV curves (mean ± std) of 1 mm pixels made with PDPP3T:ITIC (1:2 ratio) (blue, n = 13) or PDPP3T:Y6 (1:2 ratio) (orange, n = 8). C) J_{sc} D) V_{oc} E) Fill Factor F) R_{series} G) R_{shunt} and H) Power Conversion Efficiency for all 1 mm devices for both PDPP3T:ITIC and PDPP3T:Y6 pixels as violin plots. Vertical grey lines indicate the interquartile range and medians are indicated by a white circle.
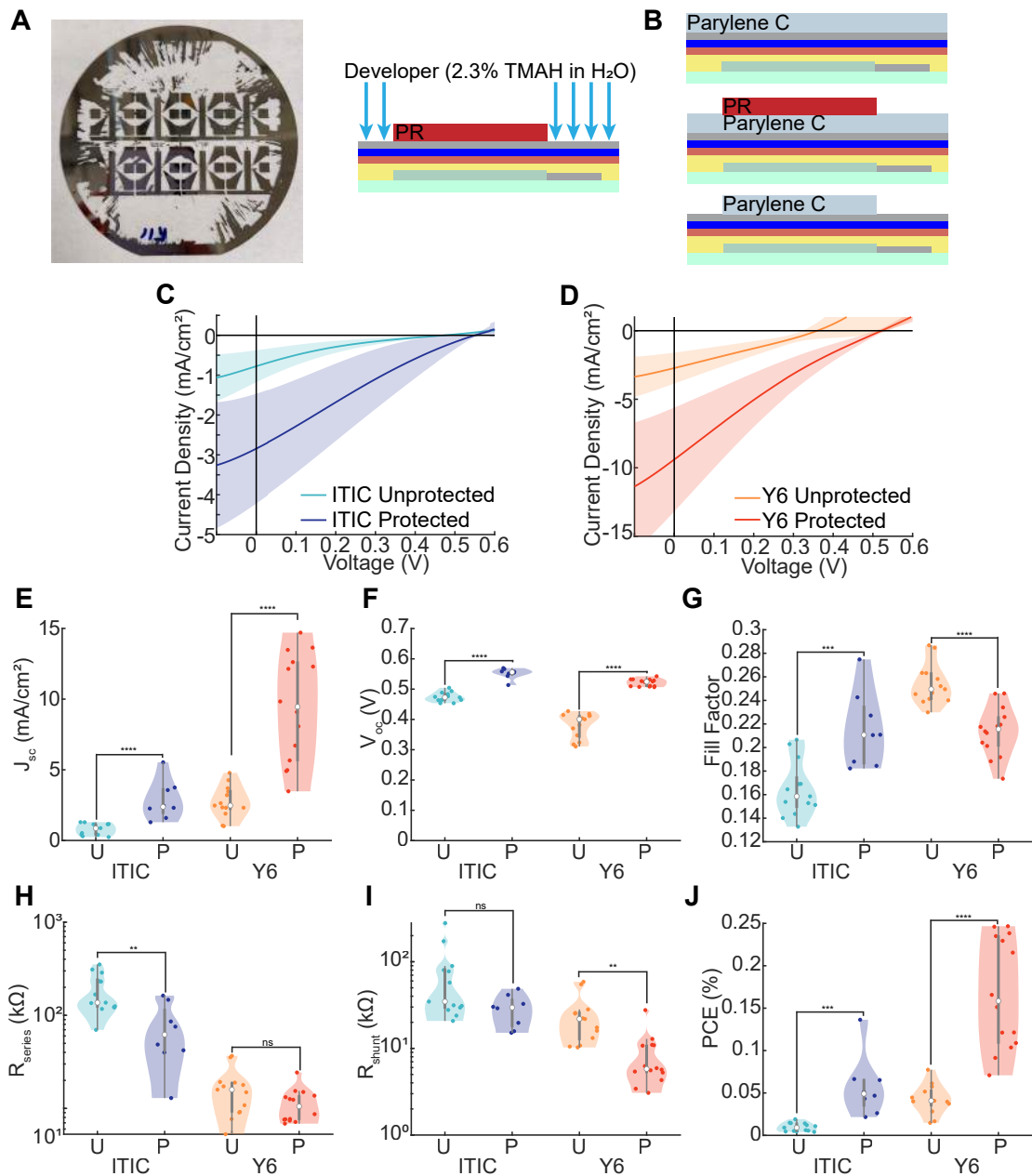
Figure 4.13: **Implementation of solvent protection during fabrication and its effect of PV performance** A) Left - Example wafer after delamination following development. Right - Process of developer entering pixel and delaminating areas not covered by photoresist. B) Process flow steps incorporated to avoid solvents interacting with the PV materials. C) JV curves (mean ± std) of 1 mm pixels made with PDPP3T:ITIC (1:2 ratio) when unprotected (light blue, n = 13) or protected by PaC (dark blue, n = 13) . D) JV curves (mean ± std) of 1 mm pixels made with PDPP3T:Y6 (1:2 ratio) when unprotected (orange, n = 8) or protected by PaC (red, n = 14). E) J_{sc} F) V_{oc} G) Fill Factor H) R_{series} I) R_{shunt} and J) Power Conversion Efficiency for all 1 mm devices for both PDPP3T:ITIC and PDPP3T:Y6 pixels as violin plots. Vertical grey lines indicate the interquartile range and medians are indicated by a white circle.

4.3.4 Tackling the S-kink

This was indeed an improvement however the noticeable S-kink with both materials was concerning (Figure 4.13C,D). The reasons for this could be numerous so one avenue of investigation was the transport layers, useful for charge separation, however possibly contributing to defects and unfavourable resistances. As the thickest layer, the semiconductive NiO held the potential for improvement. Previously, there was a decrease in efficiency when this layer was made thinner (Figure 2.10) so this avenue was considered exhausted. Thus a change in material and, consequently, in the deposition method was explored.

MoO_x is a common HTL for solar cells and was available for coating through sputtering and evaporation. Both methods allow for precise nm-range control of the layer thickness and were tested. The sputtered MoO_x resulted in a complete loss of function of the photovoltaic pixels, likely due to high energy collisions with the organic layer, so was not further explored. Evaporation of MoO_3 allowed for lower energy deposition of the organic layer surface without destroying the material itself so produced viable pixels. Devices containing either spin coated NiO or evaporated MoO_3 as the HTL were fabricated and compared for devices with either a PDPP3T:ITIC or PDPP3T:Y6 photoactive layer.

The MoO_3 group consistently outperformed the NiO group for both acceptor layers (Figure 4.14). In the case of ITIC, all parameters were improved while R_{shunt} remained the same resulting in a PCE of 0.27% compared to 0.04% for the NiO group. The S-kink seen in the NiO group with ITIC (Figure 4.14B) was removed leading to a significantly higher fill factor of 0.37 (Figure 4.14G).

The most dramatic increase was in the J_{sc} of the PDPP3T:Y6 pixels with MoO_3 which had a more than 4-fold increase to 84.4 mA/cm^2 compared to the NiO group(Figure 4.14E). This was matched with an equivalent, approximately 4-fold decrease in series resistance and shunt resistance (Figure 4.14H,I). The decrease in series resistance for both configurations indicates that indeed NiO was contributing to a higher resistive pathway. While the PCE was once again dramatically improved to 1.18% compared to the previous, the Y6-containing devices still contained a low fill factor and the S-kink demonstrated that defects within the pixel remained.

As it was not the HTL layer contributing to the S-kink for Y6 pixels, the next avenue of exploration was the organic layer itself. While a 1:2 ratio was maintained to be comparable to ITIC, other ratios were utilised within literature such as the reduced ratio of 1:1.2. During fabrication of the 1:2 ratio, the surface of the wafer after Pt sputtering appeared rough compared to the ITIC pixels. When the ratio was reduced to 1:1.2, the Pt regained its mirror-like quality and after AFM analysis, the roughness of the higher ratio was 49.7 nm and was almost halved to 25.3 nm with the reduced 1.1:2 ratio (Figure 4.15B,C).

With these smoother wafers, full pixels were fabricated and their JV curves were characterized. The J_{sc} was more than doubled to 210 mA/cm^2, V_{oc} increased by 60 mV to 521 mV and series resistance reduced by 700 Ohm to 211 Ohm while the shunt resistance did not change

(Figure 4.15H,I,K,L). Importantly, and the primary aim of this optimization, the fill factor was significantly improved to 0.31 (Figure 4.15J) leading to a PCE of 5.56% (Figure 4.15M).

The 1 mm pixels have been used for comparison throughout this section as a uniform way to compare different configurations. When considering the different sizes available, the rougher samples demonstrated a trend of increasing series resistance and a more pronounced S-kink as the sizes reduced from 1mm to 100 μm (Figure 4.15F). With a smoother layer and a lower series resistance, all sizes of pixels behaved the same when normalized to their size (Figure 4.15G).
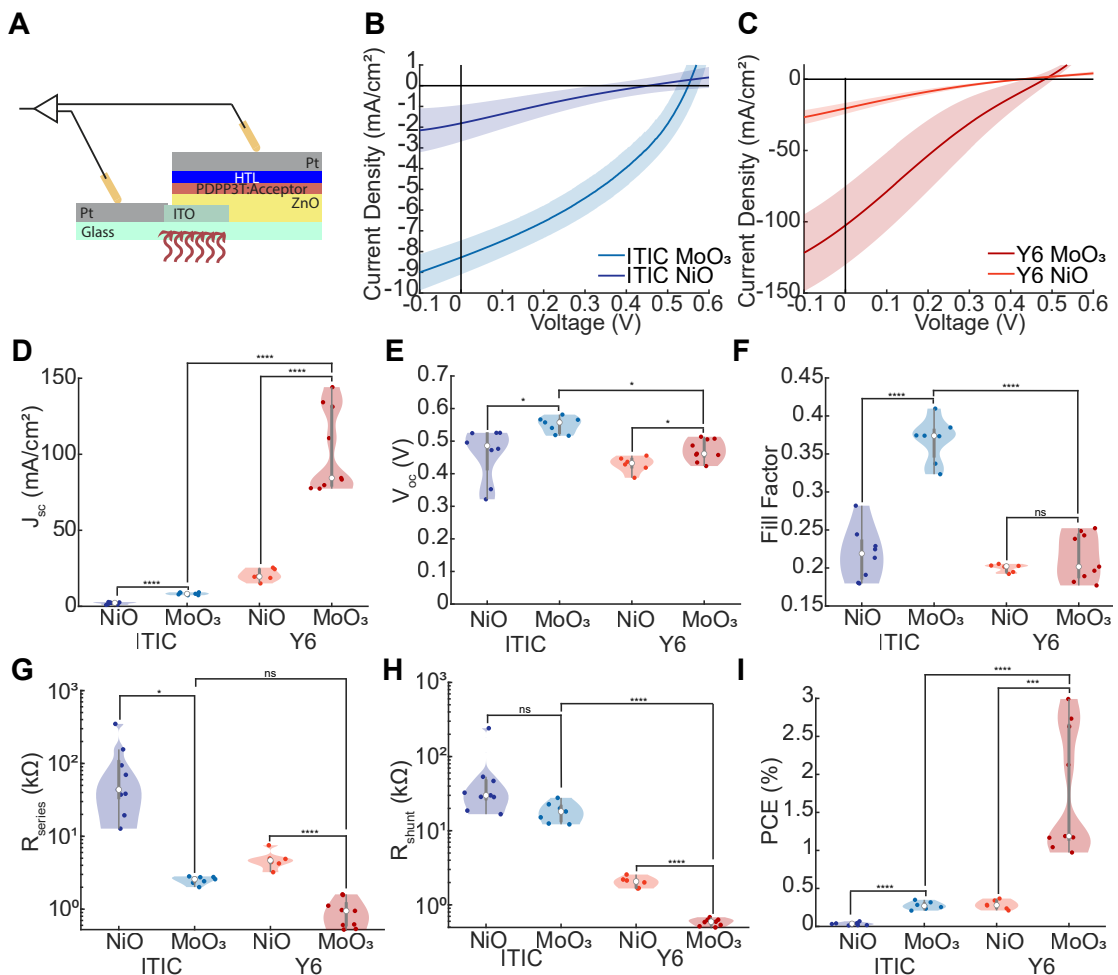
Figure 4.14: **Comparison of NiO and MoO₃ hole-transport layers on photovoltaic pixels** A) Experimental set-up with the HTL and acceptor layer varying. Pixels were exposed to continuous light (6.15 mW/mm^2), voltage was varied between -0.1 and 0.7 V and the resulting current measured. B) JV curves (mean ± std) of 1 mm pixels made with PDPP3T:ITIC (1:2 ratio) with NiO (dark blue, n = 8) or MoO₃ (light blue, n = 7). C) JV curves (mean ± std) of 1 mm pixels made with PDPP3T:Y6 (1:2 ratio) with NiO (orange, n = 6) or MoO₃ (red, n = 9). D) J_{sc} E) V_{oc} F) Fill Factor G) R_{series} H) R_{shunt} and I) Power Conversion Efficiency for all 1 mm devices for both PDPP3T:ITIC and PDPP3T:Y6 pixels as violin plots. Vertical grey lines indicate the interquartile range and medians are indicated by a white circle.
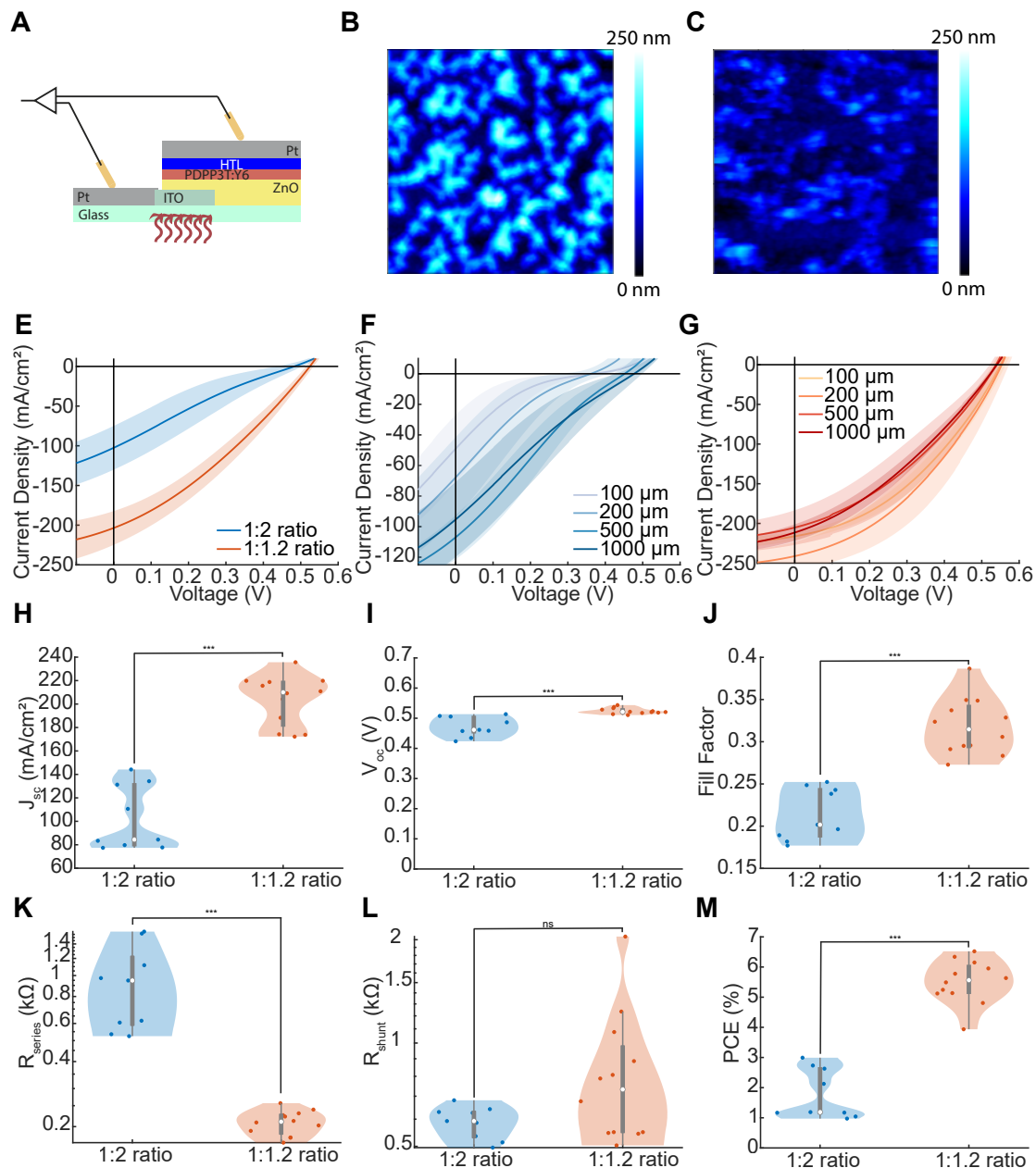
Figure 4.15: **Effect of smoother, 1:1.2 ratio of PDPP3T:Y6** A) Experimental set-up with only the ratio of PDPP3T to Y6 changing. Pixels were exposed to continuous light (6.15 mW/mm²), voltage was varied between -0.1 and 0.7 V and the resulting current measured. B) AFM Height image of 1:2 ratio of PDPP3T:Y6 for 5 x 5 μm area. C) AFM Height image of 1:1.2 ratio of PDPP3T:Y6 for 5 x 5 μm area. E) JV curves (mean ± std) of 1 mm pixels made with PDPP3T:ITIC (1:2 ratio) (blue, n = 9) or PDPP3T:ITIC (1:1.2 ratio) (orange, n = 12). F) JV curves (mean ± std) of different pixel diameters (100, 200, 500 and 1000 μm; n = 4,4,5 and 9 respectively) made with PDPP3T:Y6 (1:2 ratio). G) JV curves (mean ± std) of different pixel diameters (100, 200, 500 and 1000 μm; n = 5,4,3 and 12 respectively) made with PDPP3T:Y6 (1:1.2 ratio). H) J_{sc} I) V_{oc} J) Fill Factor K) R_{series} L) R_{shunt} and M) Power Conversion Efficiency for all 1 mm devices for both ratios as violin plots. Vertical grey lines indicate the interquartile range and medians are indicated by a white circle.

4.3.5   Performance in the aqueous environment

Mimicking the characterization done in Chapter 2, the pulsed performance in saline solution was required to assess these pixels' function in an environment akin to biological tissue. The design for these chips was also updated to account for the ITO variability, replacing the ITO contact with Pt while solely maintaining the ITO window beneath the PV pixels (Figure 4.16A). Both ratios of PDPP3T to Y6 were compared to correlate the JV performance with the pulsed aqueous performance.

Representative traces for voltage and current show the capacitive cathodic peak of current, when the light is turned on and the rate of voltage change is at its highest (Figure 4.16C). When the light is turned off, there is a smaller peak in the opposite direction as the charges return to their resting state and the voltage returns to the baseline value after 4 ms (Figure 4.16B). The peak cathodic voltage, current and total charge were significantly higher for the smoother 1:1.2 ratio chips (Figure 4.16E-G). A doubling in the performance of these pixels with the smoother ratio achieved 1.023 A/cm^2 when normalized to the size of the pixel opening of 100 μm (Figure 4.16F).

On all chips, four opening diameters were considered: 50 μm, 100 μm, 200 μm and 400 μm (Figure 4.17A). These pixels were each interrogated with different light pulse widths of 0.1 ms to 5 ms. For the 1mm hexagonal pixels with 100 μm opening diameter, the pulse width did not affect the peak current amplitude of 219 μA (Figure 4.17B) while the peak voltage steadily increased with the longer pulse widths (Figure 4.17C). For the longest pulse width of 5 ms, the voltage saturated at 481 mV, 40 mV lower than the V_{oc} reported previously (Figure 4.17C). As the pulse width increased, the charge expectantly increased with duration (Figure 4.17D). The time to reach baseline affects the frequency at which pulses can be delivered, with a shorter decay time allowing a higher frequency of stimulation. The decay time was linearly correlated with the pulse length (Figure 4.17E, Equation 4.1,R^2 = 0.997).

$$DecayTime = PulseLength + 2.8 \qquad\qquad (4.1)$$

This limits the maximum pulse frequency to approximately 350 Hz, above the standard electrical stimulation frequency for neural tissue.

With the same pulse length, all opening diameters achieved the same peak cathodic voltage (Figure 4.17F) with increasing peak current and charge (Figure 4.17G,J). The increase in peak current was closer to linear (R^2 = 0.973) rather than proportional to the square of the opening diameter, as expected as it is an exposed area. This relationship was also seen for the total cathodic charge having a linear relationship with the opening diameter. The decay time did not change with the opening area of the electrode indicating the electrode-electrolyte interface was not limiting the return to the baseline voltage level. When normalised to the area of the electrode opening, the current density of the smallest opening was the highest reaching 2 A/cm^2 and a charge density of 659 μC/cm^2.
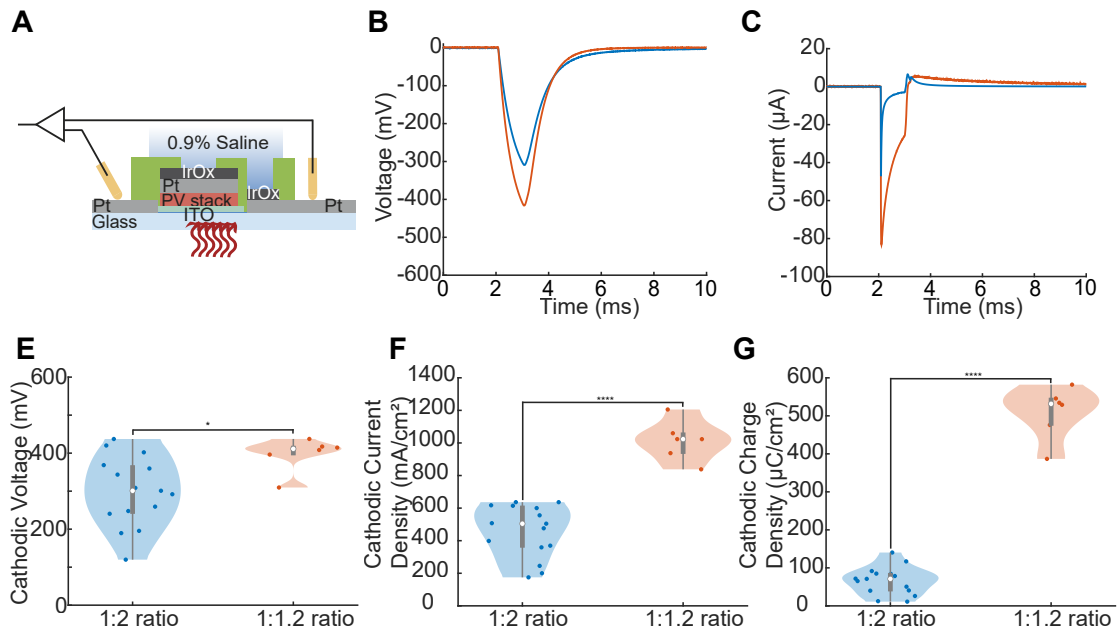
Figure 4.16: **Comparison of different PDPP3T:Y6 ratios under pulsed light and aqueous conditions** A) Experimental set-up with the pixels immersed in saline and a Pt contact for both the PV electrode and the return electrode. Pulsed NIR light (850 nm, 7.69 mW/mm²) was shone on pixels for 1 ms and voltage and current over time were recorded. Current values were normalized to the size of the opening. B) Representative voltage over time for the 1:2 ratio (blue) and 1:1.2 ratio (orange) of PDPP3T:Y6. C) Representative current over time for the 1:2 ratio (blue) and 1:1.2 ratio (orange) of PDPP3T:Y6. E) Peak Cathodic Voltage F) Peak Cathodic Current Density and G) Total Cathodic Charge Density for all 100 μm opening devices for both ratios as violin plots. The Vertical grey lines indicate the interquartile range and medians are indicated by a white circle.
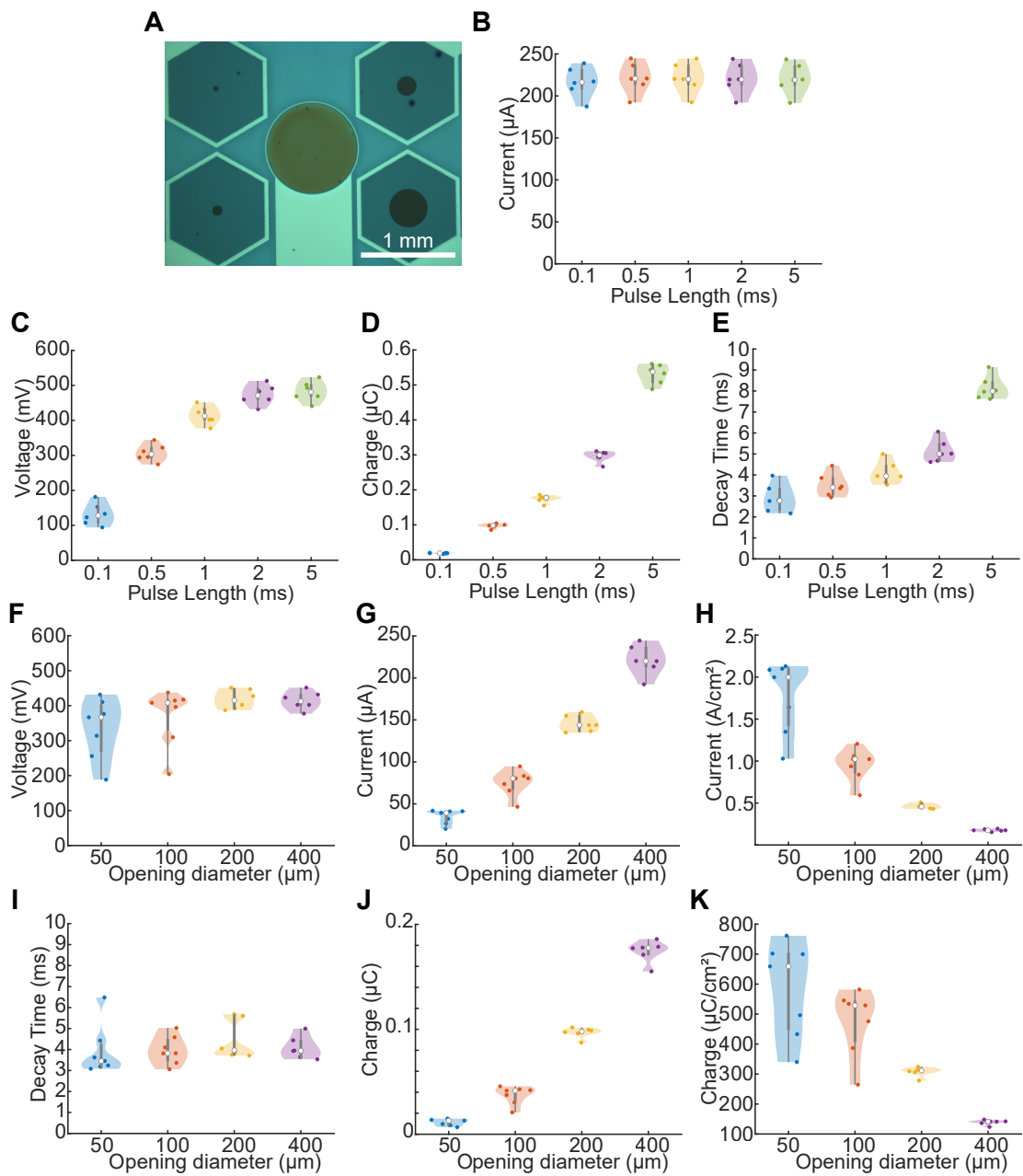
Figure 4.17: **Comparison of different pulse lengths and opening sizes on PV output** A) Chip design with four 1 mm hexagonal PV pixels, with opening diameters of 50, 100, 200 and 400 µm. The centre electrode is the return electrode with a diameter of 950 µm. B) Peak current, C) Peak voltage, D) Total charge and E) Time to voltage decay as violin plots for 400 µm electrode openings for pulse lengths of 0.1, 0.5, 1, 2 and 5 ms (n = 6 per pulse length). F) Peak voltage, G) Peak current H) Peak current density, I) Time to voltage decay, J) Total charge and K) Total charge density as violin plots for all opening diameters with a 1 ms pulse. (n = 7, 7, 6 and 6).

4.3.6 Stability of NIR-sensitive pixels in the aqueous environment

The performance of these pixels was probed over time with three various conditions. These were the standard fabrication process with no change (N), an O_2-plasma activation step between the annealing of the PDPP3T:Y6 and evaporation of MoO_3 (P) or the standard process with a layer of SiOx sputtered before deposition of the final PaC layer (S) (Figure 4.18). In all cases, there was a 5 µm layer of PaC on the device.

The standard process had a sharp drop in peak voltage, current and charge after 2 hours and was completely abolished after 21 hours (Figure 4.18A-C). In comparison to the standard process, both the addition of plasma-activation or SiOx encapsulation slowed the degradation rate of performance. They had similar effects on the peak voltage with it remaining at 50% of the original value after almost 1 day at room temperature (Figure 4.18A). Both techniques slowed the reduction of peak current and total charge with the SiOx-coated pixels performing for longer (Figure 4.18B,C). The current of pixels coated with SiOx did not change until 2 hours after immersion in aqueous solution and remained at 45% after 21 hours compared to 18% for the plasma-activated samples. The performance of the SiOx-coated pixels was abolished after 41 hours. This eventual failure can be linked to the sputtered 20 nm SiOx film likely containing pinholes thus not completely protecting the PV. Similarly, other methods of encapsulation were investigated using atomic-layer deposited materials however did not extend the lifespan of the device likely due to defects (Figure A.4).

While promising, it was important to check the effect of treatments to the absolute performance of the pixels. The plasma-treatment reduced the peak current of the pixels by approximately half from a median of 220 µA to 109 µA for the largest opening size and this trend was maintained across opening diameters (Figure 4.18D). The peak voltage was also constantly reduced by 150 - 200 mV (Figure 4.18A-E) hence the plasma-treatment was negatively affecting the performance likely as it put oxidative stress on the photoactive layer. Due to complications with processing equipment, a different etcher was used for patterning of the photovoltaic pixel during the SiOx test hence the control (Figure 4.18F,G) had different performance compared to (Figure 4.18D,E). In comparison, it also had a reduced peak current and voltage although the difference was proportionally less than that of the plasma-activated devices. This reduction in performance can be attributed to the high energy deposition of SiOx through sputtering.

In this experimental procedure, the top of the electrode was directly interfacing with the electrolyte solution meaning there was the possibility that the degradation effects were occurring due to direct diffusion through the top metal and metal oxide layers to deteriorate the pixel. To assess this, the previous data, which averaged all electrode sizes, was segregated by the size of the electrode opening.

There was no difference in the rate of degradation between the different sizes when encapsulated in PaC (Figure 4.19A,B) or with an additional layer of SiOx (Figure 4.19C,D). It is then possible to postulate that diffusion of the solution is directly through the encapsulation layer itself (Figure 4.19E) as was also seen in (Figure A.4).
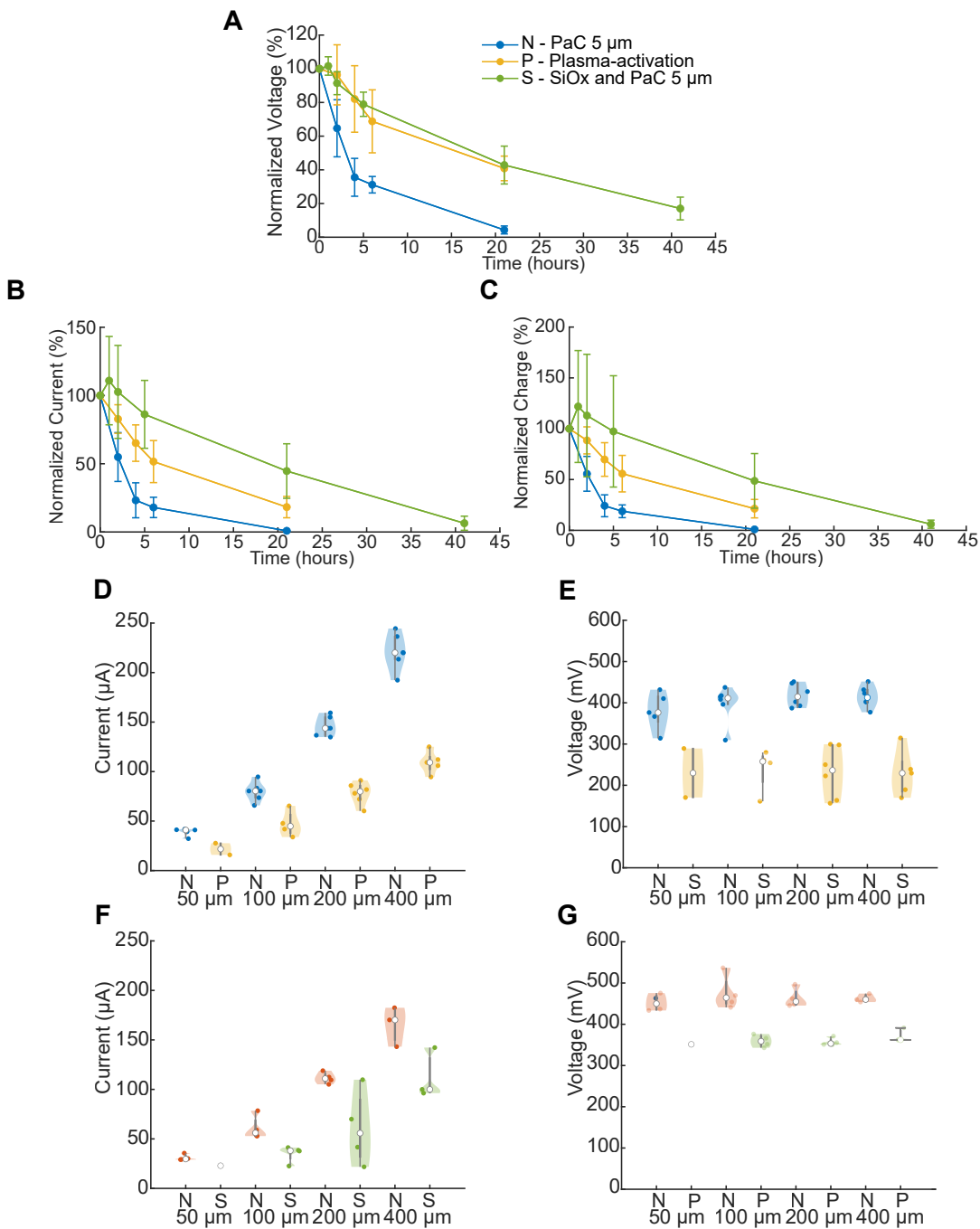
Figure 4.18: **Degradation of PV pixels in PBS with electrode openings** A) Normalized peak voltage B) peak current C) total cathodic charge for pixels encapsulated with 5 μm of PaC with (yellow, n = 17) or without (blue, n = 23) a plasma activation step before MoO_3 deposition or with an additional SiOx (30 nm) layer (green, n = 12) from single 1 ms pulses with an irradiance of 7.60 mW/mm². Mean ± std is shown for each time point. D) Peak current and E) Peak voltage for the standard process with the Veeco Nexus IBE350 etcher (N, blue) compared to with plasma activation (P, yellow) for different sizes of electrode opening diameters. F) Peak current and G) peak voltage for the standard process using the Corial 120IL etcher (N, red) compared to with SiOx encapsulation (S, green) for different electrode opening diameters.
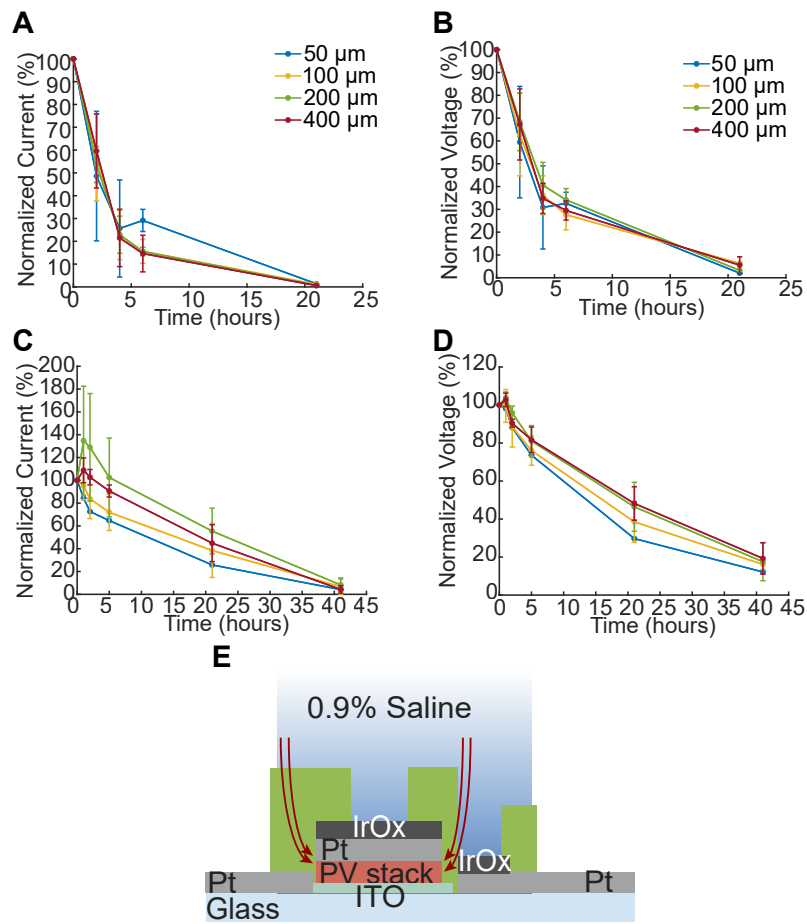
Figure 4.19: **Relationship between opening diameter and degradation time** A) Normalized current and B) voltage for the standard process with the Veeco Nexus IBE150 etcher for 50 µm (blue n = 3), 100 µm (yellow, n = 6), 200 µm (green, n = 5) and 400 µm (red, n = 5). C) Normalized current and D) voltage for PaC with SiOx encapsulation for 50 µm (blue, n = 1), 100 µm (yellow, n = 4), 200 µm (green, n = 4) and 400 µm (red, n = 3). Mean ± std is shown for each time point. E) Proposed path of ingress for water into the photovoltaic stack causing degradation.

4.3.7   Fabrication of PV implants

Based on the optimization, understanding of stability and the previous work of Chapter 3, the output currents were deemed sufficient for the activation of neural tissue in an acute setting. To test this, photovoltaic implants on 5 μm PaC were fabricated as per Figure 4.7. Other substrate materials (Figure A.2) were considered however the mechanical and barrier properties of PaC were considered a more suitable option (Figure A.3). Several modifications had to be implemented for this fabrication to be feasible. Devices were made on Si wafers instead of glass wafers, as for the characterization chips, the glass wafers were more fragile so steps were taken to avoid fractures which would result in the wafer being discarded. An initial release layer of PSS, which dissolves in water, was deposited on the wafer prior to the deposition of the substrate PaC layer. Initial fabrication tests used PaC without a release layer, which releases after one round of photolithography, however with the numerous baking steps involved in fabrication, the release was not possible for wafers without an additional release layer.

After PaC substrate deposition, SiOx was used to maintain adhesion between this PaC and the ITO window of the PV pixel. Fabrication then continued as was done for the PV/PC devices. No delamination was seen for the Ti-Pt or Ir-IrOx layers. Finally, prior to the deposition of the top PaC layer, an encapsulation and adhesion layer of SiOx (20 nm) was sputtered on the wafer. This was removed at the electrode opening sites with dry etching along with the excess PaC to define electrode openings of various sizes on one wafer (Figure 4.20A). Cathode, stimulating, electrode openings were varied between 50 μm and 400 μm with paired anode openings from 100 μm to 800 μm. Each combination where the cathode was smaller than the anode was fabricated. This totaled to 180 implants and 18 per group.

Devices were inspected for short circuit paths between the inner hexagonal PV pixel and the outer Pt support that connected to the cathode opening. A thin line of ITO was seen (Figure 4.20B) between these designs validating that alignment was sufficient and no avoidable shunt paths were available. These devices were observed under SEM following focused ion beam etching (Figure 4.20C) where the top layers of the PV pixel are clearly visible. Surprisingly, the ZnO and layers beneath were not visible via SEM.

On the same wafer, a test PVPC device was included in the design (Figure 4.20D) to assess performance as the implants themselves could not be probed. As with previous tests, 1 ms pulses of light were delivered to the pixel and the photovoltage and photocurrent were measured. The photovoltage of each pixel was different, with the highest voltage from the 200 μm opening being 350 mV and a very low voltage from the 100 μm opening suggesting defects in the device. This was further confirmed with the photocurrent, where the largest magnitude was 128 μA and there was no linear relationship between current and opening diameter. Most pronounced was the 100 μm opening producing less than 20 μA of peak cathodic current.
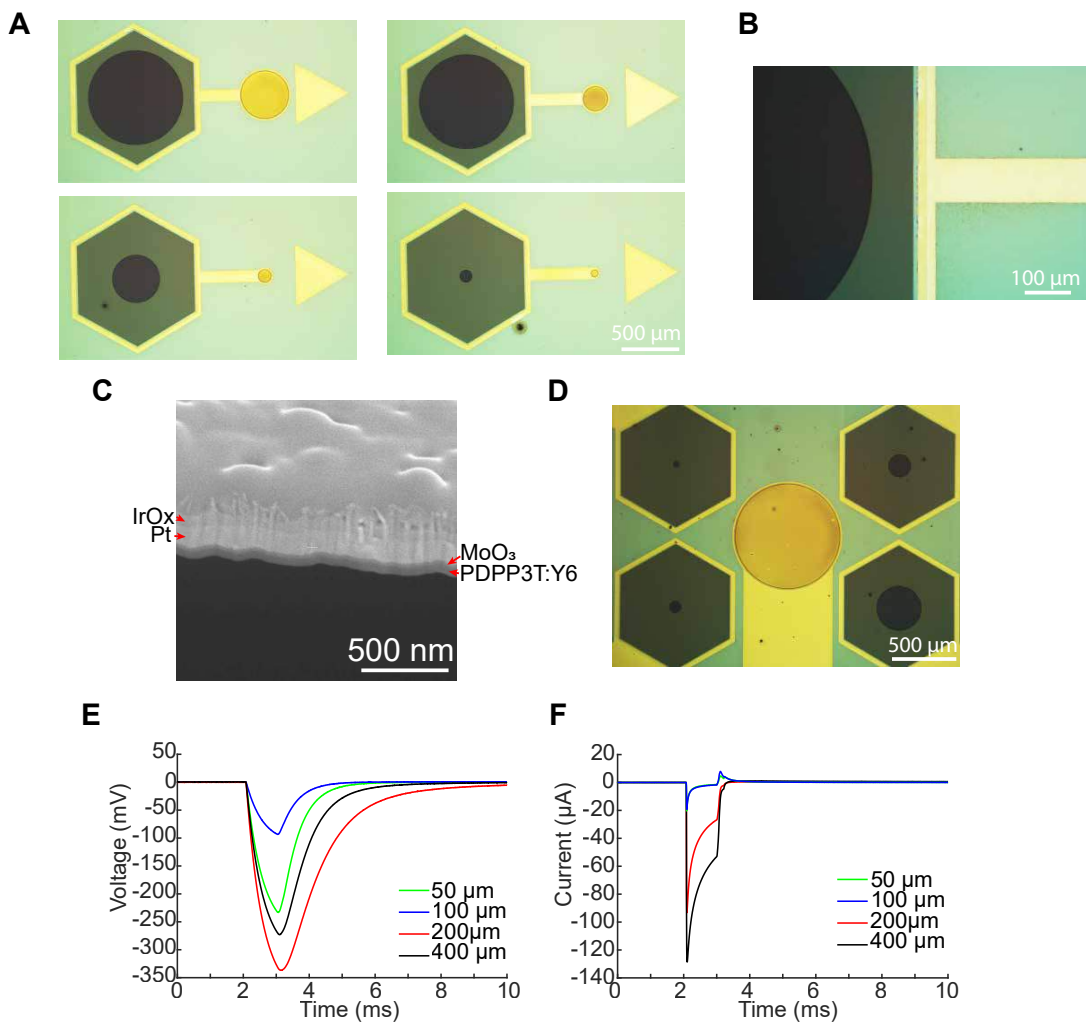
Figure 4.20: **Fabricated PV implants for neural stimulation** A) Examples of PV implants with various diameters of anode (above pixel) and cathode (smaller IrOx) opening on 1 mm hexagonal PV pixels with a guiding Pt arrow. B) Close-up on the edge of the PV pixel showing the opening, encapsulated PV, the surrounding support Pt and trace to the cathode. ITO is seen in the gap between the PV and the Pt. C) SEM image of the PV implant after focused ion-beam etching. Only the top 4 layers of the implant can be seen (PDPP3T:Y6, MoO$_3$, Pt and IrOx) before the electron transport layer ZnO. D) Test device fabricated on the same wafer as the implants with the same dimensions as Figure 4.17. E) Voltage and F) Current traces of the test device after release and placement on a supporting glass chip.

4.3.8 Preliminary in vitro and in vivo testing

Implants were still considered sufficient for the stimulation of neural tissue due to the remaining electrical output from light irradiance. To assess their feasibility, neural organoids, three-dimensional in vitro cultures that recapitulate aspects of brain development, were utilized as a preliminary model system. These organoids, measuring 3 mm in diameter, provided

a simplified yet valuable platform for investigating the implant's ability to elicit neural responses in a controlled environment. A spiderweb-like structure was designed and optimized for this tissue within the lab (Figure 4.21A) and a PV implant was placed atop the tissue, 4 months post-seeding of the organoid (Figure 4.21B). Light was delivered from an 850 nm LED connected to a 600 µm optical fibre as 1 ms pulses at 4 Hz through a plexiglass window above the organoids. The maximum output power of the LED was 38 mW, with an unknown fraction of this reaching the PV implant.

The signal was measured from all recording electrodes (Figure 4.21C) and a clear stimulation artifact was seen. The electrodes closest to the larger anode, such as electrode 26, showed an anodic-first artifact pattern while those closest to the cathode, such as electrode 23, had a cathodic-first artifact. As the light power was increased, the artifact magnitude increased as well as the amplitude of oscillations seen following the artifact (Figure 4.21D). The peak-to-peak amplitude of these oscillations increased for the electrodes directly beneath the anode (electrode 26) and cathode (electrode 23) while no oscillations were seen in surrounding electrodes (Figure 4.21E). These organoids did not exhibit spontaneous spiking activity at baseline and no spikes were seen during PV stimulation. Importantly, shining NIR light alone, without the PV pixel present, did not elicit any artifact or response in the organoid.

When the PV implants were placed on the mouse motor cortex (Figure 4.21F), as in Chapter 3, no EMG response was measured for all tested cathode openings (Figure 4.21G). An artifact was seen when the PV implant was placed on the mouse hindlimb close to, but not above, the recording EMG needles (Figure 4.21H). The oscillation seen with the organoids was also seen when activating the PV device on the muscle.

To gain a better understanding of cortical stimulation with these dimensions of electrode openings and spacing, a typical PI implant was made with Pt and IrOx as the electrode coating (Figure 4.22A). Electrode pairs were each tested for their threshold to elicit EMG response, indicating cortical stimulation, with the cathode placed over the motor cortex and the anode 1.1 mm rostrally located. A decrease in cathode or anode size both resulted in a decrease in stimulation threshold. The minimum threshold was 220 µA with a 100 µm cathode and 200 µm anode, more than 13-fold higher than previously seen with 20 or 40 µm openings. The total area, including cathode and anode, was $39\,250\,\mu m^2$, 6.25 more than the previous in vivo tests. However, this was tested with only one mouse so further exploration is needed to validate these differences.

Notably, when using the same pair of electrodes and without adjusting the implant, the threshold for 6 pulses of 1 ms was 220 µA while the threshold was 700 µA when using 0.1 ms pulses with the same frequency. In terms of charge, this was 70 nC instead of 220 nC for the longer pulses.
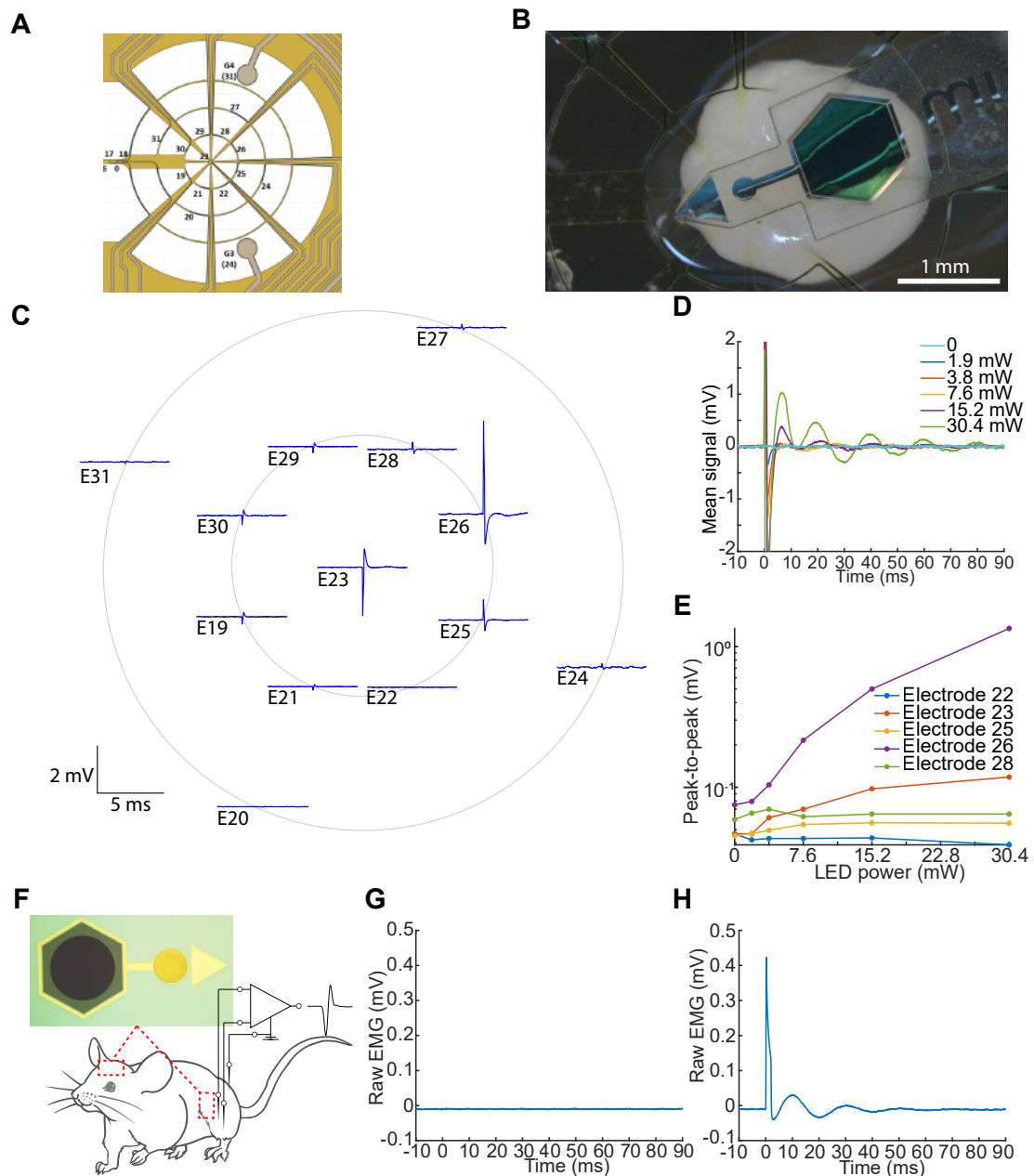
Figure 4.21: **Pilot test of PV implants on neural tissue** A) Layout of recording system on which neural organoids can be placed made of PI and contacts of Pt. B) Neural organoid with a PV implant placed on the top surface of the tissue. The cathode was 200 μm and the anode was 800 μm. C) Response map of all electrodes, corresponding to electrodes 19 to 31, when a 1 ms light pulse was delivered. Full-field light of 7.6 mW was delivered from an optical fibre connected to an LED placed outside the chamber above the organoid. D) Mean signal from electrode 26 of 30 pulses delivered at 4 Hz for increasing light intensities. E) Peak-to-peak voltage amplitude for increasing LED power. F) Experimental set-up for PV implants placed on either the motor cortex or the mouse hindlimb. EMG is recorded from the mouse hindlimb. G) Recorded EMG response from 38 mW with cathode placed above the motor cortex. H) Recorded EMG response from 38 mW with anode and cathode placed on the mouse hindlimb muscle, the tibialis anterior.

A

B

C
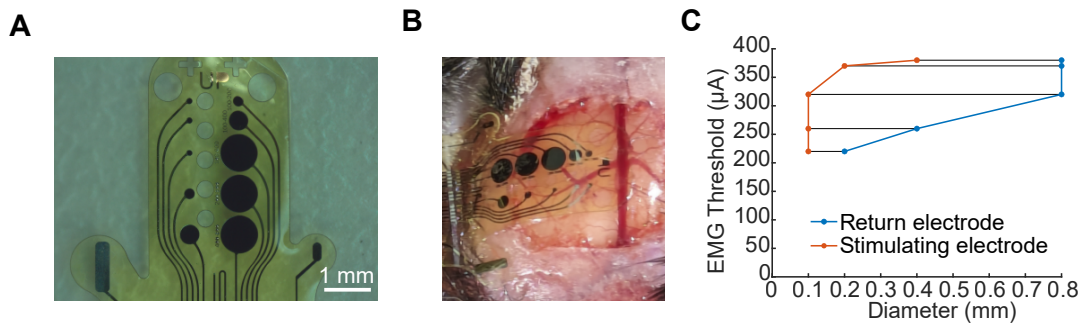
Figure 4.22: **Exploration of thresholds with PV-mimicking electrical device** A) Image of the device with pairs of electrodes of increasing stimulation (left) and return (right) area. Diameters from top to bottom: (cathode, anode) = (100 μm, 200 μm),(100 μm, 400 μm),(100 μm, 800 μm),(200 μm, 800 μm),(400 μm, 800 μm) B) Implant placed on the mouse cortex with the first pair cathode at 1 mm posterior and 1 mm lateral to bregma. C) Stimulation thresholds for an EMG response for each pair of electrodes, plotting plot the stimulating and return electrode, and pairs indicated by the connecting black lines.

4.4   Discussion

Summary

The development of a near-infrared (NIR) sensitive photovoltaic cell began with the selection of PDPP3T as the donor material due to its NIR absorption. Initial explorations compared the acceptor materials $PC_{71}BM$ and ITIC, with ITIC demonstrating low efficiency and fill factors attributed to fabrication defects. Further testing transitioned to the acceptor Y6, which showed significantly improved short-circuit current (J_{sc}) over ITIC, but still displayed an "S-kink" in the current-voltage curve. To address this issue, the HTL was changed from NiO to MoO_3, resulting in a dramatic improvement in both J_{sc} and fill factor, resolving the "S-kink" in the process for ITIC devices only. Additionally, reducing the PDPP3T:Y6 donor-acceptor ratio to 1:1.2 produced smoother films, substantially improving overall performance and eliminating the poor FF. This optimization ultimately led to a power conversion efficiency (PCE) of 5.56%.

Testing in an aqueous environment confirmed that the smoother 1:1.2 ratio pixels demonstrated double the performance under pulsed light in saline compared to previous configurations. While longer pulse widths increased the generated voltage, although below the V_{oc}, the current remained unaffected. The peak voltage remained constant at 480 mV across various opening sizes, with both current and charge increasing linearly with the opening area. However, the smallest opening size demonstrated the highest current and charge densities, reaching 2 A/cm² and 659 µC/cm², respectively.

When assessed for stability, the pixels were found to be unstable in water. Two strategies, plasma-activation prior to MoO_3 deposition and a SiOx layer, improved stability. SiOx-coated pixels performed for longer. However, plasma-activation and SiOx coating negatively impacted absolute device performance. Importantly, the degradation rate was independent of electrode opening size, implicating water diffusion through the encapsulation layer as the primary failure mechanism, rather than through the exposed electrode.

Preliminary in vivo testing of the NIR-sensitive photovoltaic implants, using SiOx coating for acute experiments, yielded mixed results. While the implant was successfully activated with diffuse NIR light on neural organoids, with clear artifacts and oscillatory activity in nearby electrodes, no EMG response was elicited from the mouse motor cortex.

Photovoltaics and microfabrication

This chapter underscores the delicate nature of organic solar cell materials and the detrimental impact solvents can have on their performance. The catastrophic delamination observed during the patterning process clearly highlighted the need for a protective strategy. The introduction of a PaC layer proved to be a crucial step in safeguarding sensitive photovoltaic materials from the harsh chemicals used in subsequent microfabrication steps. This protective layer not only prevented damage but also enabled the exploration of higher-performance

materials like MoO_3, which would otherwise be too sensitive for use in this process.

While the organic materials used in NIR-sensitive solar cells are inherently sensitive to fabrication processes, this chapter demonstrates the feasibility of successfully patterning these devices using standard microfabrication techniques. Notably, challenges encountered with the variability of ITO properties, across seemingly identical deposition conditions, underscore the importance of meticulous process control throughout device fabrication. Ensuring the consistency and quality of each layer, including those considered standard, is crucial for achieving reliable device performance and reproducibility.

The incremental nature of optimization was seen with each step, from the donor material, the hole transport layer (HTL) and the BHJ ratio providing an improvement towards attaining an efficient pixel. Using Y6 as the acceptor material capitalizes on the range of research into improving acceptor layers[131]. While not a direct contributor to charge generation, complementary absorption spectrums of the acceptor material can improve efficiency through beneficial energy transfer mechanisms to the donor[132,133]. The substantial improvements in performance parameters like J_{sc} and fill factor after switching from NiO to MoO_3 demonstrate how the choice of HTL can dramatically influence device behaviour. Furthermore, the ability to evaporate MoO_3 allowed for precise control of the HTL thickness with low deposition energy to protect organic materials, likely contributing to better charge transport compared to the solution-processed NiO layer. The BHJ ratio led to a large change in the roughness of the organic layer, with a smoother layer providing better performance and notably, consistent performance regardless of pixel diameter. In the case of the rougher material, the smaller pixels being less efficient was largely attributed to the difference in normalized series resistance. This indicates the presence of edge effects, which are a larger proportion for smaller pixels, likely introduced during the patterning process.

Continuous vs pulsed performance

It was intuitive that an improved efficiency, from the JV pixels, would lead to improved performance in the aqueous environment but the proportion of this improvement needed to be characterized. This is due to the interfacial dynamics between the pixel and the solution.

While not present in the JV pixels, IrOx was used as an electrode coating to avoid unwanted electrochemical effects during stimulation. This could not be captured in the JV design as an IrOx layer atop the Pt would merely add additional series resistance, taking away from the efficiency of the pixel. IrOx is known to decrease the impedance of electrodes in solution[134]. At high frequencies, such as at the onset of the light pulse when the bulk of the voltage is applied, there is no capacitive component with the impedance dominated by the resistance of the interface and solution. Nonetheless, the series resistance would be naturally higher with a 150 nm semiconductor layer atop the Pt potentially reducing the performance of the pixel.

The instantaneous current cannot be correlated with the J_{sc} of the JV curve as the JV curve

is obtained during a continuous, and static, illumination of light. While the J_{sc} of these pixels was 210 mA/cm^2, the normalized current density changed with the opening diameter. Extrapolating from the gathered data, a 1 mm opening would provide approximately 596 μA of current and 76 mA/cm^2. This reduction by a factor of 2-3 can then be attributed to the presence of solution. The JV comes into play when considering the relative performance of pixels where comparing the rougher and smoother PDPP3T:Y6 layers, there was an 2.49 times increase in J_{sc} while it was a 2.04 times difference in peak current density. In terms of voltage, the correlation between PVPC and JV is more evident with the continuous light resulting in a V_{oc} of 521 mV while a short 5 ms pulse width had a max voltage of 481 mV. Due to the exponential relationship of pulse length and voltage, it can be expected that for longer pulse widths, the open-circuit voltage could then be obtained.

Poor in vitro and in vivo performance

Despite achieving relatively high performance, the NIR-sensitive implants failed to elicit the desired neural responses in vivo. While reduced in performance from the encapsulation, the pixels were still considered efficient enough for testing in vivo. A consistent oscillatory pattern was observed in both organoid and muscle tissue yet this pattern appears to be an artifact stemming from the photovoltaic stimulation rather than true neural activation or potentially a subthreshold activation of tissue[135]. This type of artifact has also been observed in other studies employing photoactive stimulation of the cortex[81].

This raises questions about whether device layout or voltage limitations might be the primary obstacles. The larger electrode openings used in these implants could necessitate higher stimulation thresholds, as suggested by the follow-up experiment with an electrical stimulation device. The observation that shorter pulse durations (0.1ms) required higher stimulation currents compared to longer pulses (1ms) underscores the complex interplay between current, charge, and stimulation efficacy.

Conclusion

This chapter demonstrates successful progress in the fabrication and optimization of NIR-sensitive photovoltaic cells. Careful attention to material selection, device design, and protective strategies resulted in an efficiency of 5.6%. Key advancements include the implementation of a protective PaC layer, which allowed for the use of a higher-performance hole transport layer and shielded photovoltaic materials from damaging solvents during fabrication. Additionally, optimization of the donor-acceptor ratio within the photoactive layer (PDPP3T:Y6) led to smoother films and a substantial improvement in overall device efficiency. This efficiency was highly unstable, with devices degrading in aqueous solution, and needing encapsulation to allow for sustained immersion. However, this encapsulation came at a cost to performance contributing to the lack of reliable cortical stimulation highlighting the complexities of translating lab-bench performance into real-world biological applications.

5 Discussion and Outlook

5.1 Summary of research

Developing a photovoltaic implant for neurostimulation has the potential to be a transformative technology in the field of neural engineering, with the potential to revolutionize the way we treat neurological disorders and injuries. It has the potential to remove cables and associated failure points and reduce the FBR while also being compatible with standard fabrication methods for flexible implants. This thesis has explored the design, fabrication, and testing of such an implant, to demonstrate its feasibility and efficacy. It presents a thin, flexible, microfabricated organic photovoltaic implant with the potential to activate neural tissue in vivo using near-infrared light. The following sections summarize the key findings of this research. These results provide a strong foundation for further development of this technology, with the potential to significantly improve the lives of patients suffering from a wide range of neurological conditions.

5.1.1 Chapter 2

An initial section of this research focused on the fabrication of P3HT:PCBM photovoltaic pixels. The fabrication process was optimized to enhance pulsed output, which is crucial for neurostimulation applications. Current-voltage (JV) measurements were performed to assess the performance of inverted solar cells with the final structure of the device being ITO as the transparent cathode, ZnO as the electron-transport layer, P3HT:PCBM at a 1:1 ratio as the photoactive layer, NiO as the hole-transport layer, Pt as the top anode and coated with IrOx.

5.1.2 Chapter 3

Concurrent with the fabrication and optimization of the photovoltaic cell, experiments using bipolar stimulation of the mouse motor cortex were used to investigate stimulation thresholds. These experiments revealed that both the direction and distance between electrodes influenced the stimulation threshold. Notably, a threshold of 16 μA was observed using six 1 ms

cathodic-first biphasic pulses at 181 Hz. This threshold did not change when the stimulating electrode was 20 or 40 μm in diameter. This finding highlights the importance of electrode placement and configuration in achieving effective neurostimulation.

5.1.3 Chapter 4

These sections were preliminary investigations prior to using NIR materials to fabricate a photovoltaic pixel sensitive to light that transmits through the biological tissue window. Several steps of optimizations established a pixel architecture with: ITO - ZnO - PDPP3T:Y6 (at a 1:1.2 ratio) - MoO_3 - Pt using the JV measurement system. When tested in an aqueous solution with an IrOx electrode coating, these pixels demonstrated a peak current of 219 μA for 400 μm openings and 80 μA for 100 μm openings, with a charge of 40 nC for 1 ms pulses from 100 μm openings. This charge was increased for longer pulse durations or opening diameters. However, the pixels were found to be unstable, with their lifespan dependent on the encapsulation layer. SiOx encapsulation extended the peak lifespan to several hours. Preliminary in vivo work with these pixels on neural organoids and exposed muscle resulted in subthreshold or artifact-related activity, but no successful in vivo cortical stimulation was achieved.

5.2 General discussion, limitations and future work

5.2.1 Performance

Solar cell efficiency

While progress was made in optimizing the fabrication and performance of the NIR-sensitive photovoltaic cells, it's important to consider their efficiency within the broader context of solar cell technology. The best-performing pixels achieved a 5.6% efficiency under illumination from a single LED with a spectrum of 800-900 nm. This result is encouraging, especially given the challenges of working with sensitive organic materials in microfabrication and the narrow spectral input compared to standard solar cell testing conditions.

Traditional solar cell fabrication and efficiency measurements utilize the full solar spectrum (AM1.5G) to assess device performance. Since the chosen material PDPP3T also has a smaller shoulder peak in its absorption spectrum at 780 nm, it can potentially utilize a broader range of wavelengths. Therefore, leveraging the full solar spectrum could further enhance the efficiency of these NIR-sensitive devices by taking advantage of a larger spectrum of available energy transitions in the material. Limiting the available spectrum to a specific range would naturally lead to a reduction in efficiency compared to standard AM1.5G conditions. This is consistent with the findings from other studies that evaluated solar cell performance under varying spectral conditions[136].

In order to fully evaluate the potential of the photovoltaic pixels developed in this research, future work should include a characterization under standard AM1.5G illumination conditions. While likely to have reduced efficiency, as shorter wavelengths would not be harnessed by the NIR-sensitive PV pixel, this would provide a standardized assessment of the pixel's power conversion efficiency and other performance metrics, allowing for a direct comparison with other organic PV devices reported in the literature. This comprehensive analysis would offer a more accurate evaluation of the pixel's capabilities and potential for real-world applications, ultimately informing further design optimization and material selection for future iterations of the photovoltaic implant.

A fraction of the conceivable optimizations were done in a trade-off between improving PV performance and testing applications on neural tissue with a consideration of time. Further optimization is undeniably possible. A ratio of 1:1.2 of Y6 was deemed acceptable for its efficiency but, similar to the ITIC and $PC_{71}BM$ tests, a series of ratios should be tested particularly noting that Y6 can form molecular aggregates at high concentrations resulting in the roughness seen. Furthermore, a systematic optimization of the pixel itself could be undertaken. This could involve exploring various layer thicknesses and processing parameters, such as baking temperatures and surface treatments, to enhance the overall performance of the photovoltaic implant.

More broadly, the organic donor material PDPP3T was chosen for its absorption spectrum from 600 to 900 nm. Despite stimulation from only 800 - 900 nm, the 5.6% efficiency compares favourably to the published results being 5.3% with a $PC_{71}BM$ donor[137]. Typically, this donor is used as support for other, newer, and more efficient materials such as perovskites[138] for hole transport or in tandem with amorphous silicon[137]. Novel organic materials such as PM6 have, in combination with Y6, shown a performance of 15.11% without additives[139] and even higher efficiencies with additives and treatments[140]. However, these novel materials do not absorb in the NIR so are not relevant for this application. This makes it difficult to capitalize on advancements in material science to produce better NIR-sensitive organic solar cells with the current trend being in NIR acceptor materials, such as Y6, but high-energy visible spectrum donor materials. This is also true for the perovskites which are highly efficient in the UV and visible spectrum but absorption is minimal in the NIR.

Output in solution

A notable limitation of this work was the lack of exploration into the effect of varying pixel sizes on the pulsed performance of the photovoltaic cells in solution. While this was investigated during the JV characterization, this was not further examined in the PVPC configuration. The focus on optimizing pixel architecture and material composition was valuable but it neglected the potential impact of pixel size. By measuring the output from smaller pixels, any edge effects coming from the fabrication process could be elucidated filling this critical gap in our understanding. Future studies should systematically investigate the influence of pixel size to determine the optimal dimensions for maximizing pulsed performance and achieving

efficient neural stimulation in vivo.

Another limitation of this work, and an aspect worth exploring further, is the spatial distribution of the delivered charges. As noted previously, there exists a separation between the epicortically positioned implant and the targeted neurons, which can significantly impact the effectiveness of stimulation. While previous studies have utilized micropipettes in solution to examine transient voltage changes at specific distances from the electrode surface[71], a more comprehensive understanding of the spatial voltage distribution emanating from these photovoltaic pixels is warranted.

Future investigations should aim to systematically probe this spatial distribution, potentially using a combination of experimental approaches and detailed computational modelling. Comparing experimental results with simulations of both the pixel device and the surrounding neural tissue could offer valuable insights into the expected stimulation range and spatial precision achievable with these implants. This is of particular importance in the context of cortical stimulation, where precise spatial targeting may be crucial for selective neural activation and minimizing unintended effects on neighbouring neurons or neural circuits.

5.2.2   In vivo cortical activation

Despite the promising results obtained in bench-top characterisation, the in vivo experiments with the photovoltaic implant did not yield the expected cortical stimulation. This section delves into the potential reasons behind this discrepancy, exploring factors related to the determination of thresholds and PV design. A comprehensive analysis of these factors is crucial for identifying the limitations of the current approach and devising strategies for future improvement.

Setting an electrical benchmark

In vivo testing using electrically activated devices provided valuable insights, highlighting the intricate relationship between stimulation parameters and device configuration. Neural stimulation paradigms often prioritize charge delivery over current. A notable output, while preliminary, was the difference in charge requirements from a rapid 0.1 ms pulse, needing 70 nC of charge, compared to a longer 1 ms pulse needing 220 nC despite using the same electrodes. This invites further exploration as then it is not charge density alone but the duration over which this charge is applied that determines whether neural activity is elicited. For PV devices, it means that the dynamics of the pixel play a large role in delivering sufficient charge within a biologically relevant timeframe.

Perhaps the most unexpected finding was the minimal variation in current thresholds between different stimulating electrode sizes. This warrants a deeper investigation into the complex interplay between total electrode area, current amplitude, and current density. Further investigation down this path would require a broad range of both stimulating and return electrode

areas, determining how the current threshold varies with the total area as opposed to the area of the stimulating electrode alone. Depending on the results of such an investigation, it could have profound effects for both photovoltaic stimulation and electrical stimulation of the cortex at large.

An aspect this thesis did not explore was using voltage-controlled stimulation of the cortex. Current amplitudes were set through a pulse stimulator with high voltage compliance. Voltage-controlled stimulation is not commonly used because it is sensitive to the impedance of the device and system while current-controlled stimulation can minimize these differences. Investigating voltage-controlled systems is particularly challenging when determining minimum thresholds for cortex activation as it is sensitive to the electrode impedance, track resistance and contact resistance, all difficult to control in the in vivo setting. Given that photovoltaic devices are inherently voltage-driven, exploring voltage-controlled stimulation strategies provides an understanding of the requirements needed and correlates this to photovoltaic performance. The lower voltages typically generated by organic solar cells might be insufficient for effective neural stimulation, even with adequate current output. Future work could investigate strategies to increase voltage output, such as modifying the design to connect multiple pixels in series[127].

Voltage limitations

This aspect has been explored in the literature theoretically, considering the impedance of the tissue, stimulation requirements and the voltage output of the system. In particular, a question about voltage limitations from the PV cell has resulted in the commercial PRIMA device[126], the GaAs-based device[50] and the organic bilayer[141] all employing two or three photovoltaic cells in series to aggregate the output voltage. Tandem solar cells effectively double the output voltage while halving the output current for the same light intensity, as multiple photons are then needed for the same flow of current. Conversely, the POLYRETINA[71] used single photovoltaic pixels for retinal stimulation. Given the successful retinal stimulation of the POLYRETINA, a single junction solar cell was maintained for this work.

The limiting factor in neurostimulation circuits can be either photovoltage or photocurrent, depending on the electrode's charge capacity.[142]. Iridium oxide electrodes, with their high charge injection capacity and low impedance, make photocurrent the more likely limiting factor on the device side. However, tissue impedance and electrode size also play crucial roles. Here, the photovoltaic material properties set a hard upper limit on photovoltage, making stimulation highly reliant on a constant and low impedance at the tissue and electrode-electrolyte interface. This ideal condition is often not met, potentially leading to stimulation failure, as observed in this work. While pixel efficiency is necessary for high photocurrent, the interface and tissue ultimately determine the voltage spread and charge interacting with the target tissue. A critical step is then incorporating a tandem solar cell to overcome these limitations.

Translating bench-top results to in vivo stimulation

One potential explanation for the lack of in vivo stimulation despite promising results using pulsed light lies in the inherent differences between the experimental setups. The pulsed experiments conducted in aqueous solution, while valuable for assessing the photovoltaic pixel's electrical properties and the electrode-electrolyte interface, may not fully replicate the complex environment of the mouse cortical tissue. The presence of lipids, proteins, and the non-uniform structure of brain tissue can significantly impede the propagation and distribution of ionic currents necessary for neural activation. These factors could potentially attenuate or distort the electrical signals generated by the PV pixel, rendering them insufficient to reach the stimulation threshold of the target neurons embedded within the intricate cortical tissue.

Making and using PV implants

As noted in Chapter 4, the fabrication of PV implants for neurostimulation required several alterations to the fabrication process. The resultant PV implant had less power output compared to the devices fabricated on glass, as expected given the additional steps and stress placed on the PV pixel. Of particular note was the use of sputtered SiOx for adhesion of the PaC to itself and slight encapsulation of the PV pixel. This layer, while instilling a small degree of stability, likely also damaged the PV pixel resulting in its lower performance. While considered acceptable for the in vivo tests, it was evidently too large a reduction in performance to enable neural stimulation.

As such, a key limitation of the work is the lack of optimization of the implant fabrication process in terms of both encapsulation, which will be explored later, and performance. An immediate future step is to fabricate devices without the SiOx layer, tolerating poor stability and adhesion, to assess if the PV design that delivered 5.6% efficiency in the NIR range would elicit neural stimulation. Further tailoring of the in vivo fabrication process is necessary to optimize device performance within this new context and to ensure that the efficiency gains achieved on glass substrates translate effectively to the in vivo setting. Examples of this are to replace the transparent conductive oxide, ITO, with a less brittle material such as a thin metallic or graphene layer. The implant could also be designed to keep the PV pixel away from the cortical tissue, with its curved surface, with tracks to the anode and cathode openings.

A distinct oscillatory pattern was measured from recording electrodes when interfacing with the muscle or organoid tissue. As posited in Chapter 4, this could be a subthreshold stimulation artifact as seen with optogenetic activation of brain slices[135]. Other studies using PV devices[81] on cortical tissue also show this oscillatory pattern with laser-sourced light, and without rhythmic time-locked muscle activation, so perhaps the EMG response was merely too high a bar to achieve with the current stimulation set-up. A simple increase in the light intensity should elicit the desired suprathreshold stimulation of tissue and muscular activation. Undoubtedly, this would then bring about questions of safety limits with high

amounts of NIR light known to cause noxious levels of tissue heating and it capitalized on for cancer treatment[143]. The short pulses, in the ms-range, would avoid these large levels of tissue heating but should be carefully considered. Conversely, the light intensity could be maintained, but the implant size could be expanded, increasing the absorbed light and thus the output current. This thesis focused on a 1 mm diameter footprint for PV devices to maintain comparability however future devices with large diameters would be another facile way of moving towards cortical stimulation.

5.2.3 Stability

Organic solar cells are notoriously unstable with recent efforts prioritising this aspect and improvements made in the area[144] based on organic layers and the buffer layers around them. Of particular concern is molybdenum trioxide (MoO_3) which acts as a hole transport layer. It facilitates the extraction of positive charges (holes) from the organic active layer and improves device performance. However, MoO_3 exhibits instability in the presence of water[145]. This is due to its hygroscopic nature, meaning it readily adsorbs moisture from the environment. Water absorption can lead to changes in the chemical composition of MoO_3, altering its electronic properties and reducing its effectiveness as a hole transport layer. Furthermore, moisture can promote interfacial degradation within the organic PV device, compromising overall stability and longevity. The high performance with MoO_3 is counteracted by its instability so future exploration could be on the evaporation of other hole-transport layers.

It was encouraging to discover that, while the pixel is unstable, it can be mitigated with extra encapsulation thus it is then possible to focus on the encapsulation itself, an ongoing problem within neural implant research. There is an inherent limitation of single-layer encapsulation as regardless of the meticulousness of the deposition process, unavoidable defects within a single layer provide direct pathways for water ingress. Multi-layered or hybrid encapsulation approaches address this challenge by creating a more convoluted path for diffusion[146]. Thus, despite defects within individual layers, the staggered nature of a multi-layered system ensures that a defect in one layer is less likely to align with a defect in the subsequent layer. This significantly increases the distance that water molecules must travel to reach the sensitive components of the photovoltaic pixel, dramatically enhancing protection. The failure of single-layer strategies underscores the critical importance of advanced encapsulation solutions, a well-recognized challenge within the broader field of neural implants[125].

While a comprehensive investigation of encapsulation strategies lies beyond the scope of this thesis, the results presented here highlight several promising avenues. The improved stability observed with plasma-activation and SiOx integration points towards the potential benefits of surface modification and additional barrier layers. The trade-offs associated with these techniques, such as the reduction in absolute device performance seen with plasma-activation, necessitate further refinement. Ultimately, the development of robust encapsulation solutions

will be essential to ensure the long-term functionality and viability of photovoltaic neural implants, paving the way for advancements in neuroscience research and clinical applications.

5.3   Conclusion

The development of a photovoltaic implant for neurostimulation represents a significant step forward in neural engineering, with the potential to revolutionize the treatment of neurological disorders and injuries. This thesis has explored a minimally invasive, flexible organic photovoltaic implant with the potential to activate neural tissue in vivo using NIR light, demonstrating its feasibility for neural applications.

While the prototype exhibited promising results, further advancements are needed to achieve reliable in vivo stimulation. To benchmark performance against other organic photovoltaic devices, characterization under standard AM1.5G illumination conditions will provide a standardized assessment of power conversion efficiency and other performance metrics. Investigating novel device architectures and fabrication techniques may further maximize light absorption and charge collection, leading to more efficient neural stimulation.

Another critical area for future research is ensuring long-term functionality in vivo. This necessitates the development of robust encapsulation strategies to mitigate the instability of organic materials in the physiological environment. Optimizing the fabrication process is also essential to achieve better adhesion and stability of implant components while minimizing damage to the photovoltaic pixel. This could involve replacing brittle materials like ITO with more flexible alternatives and designing the implant to shield the photovoltaic pixel from direct contact with cortical tissue.

In vivo performance can be improved through systematic investigation of the influence of pixel size on pulsed performance. This will aid in determining the optimal dimensions for efficient neural stimulation. Additionally, detailed studies on the spatial distribution of delivered charges, combining experimental measurements with computational simulations, are necessary to understand and optimize the stimulation range and precision. Exploring voltage-controlled stimulation strategies could also overcome the limitations of low voltage output from organic solar cells. To fully realize the potential of photovoltaic implants, a deeper understanding of the underlying mechanisms of neural stimulation is essential. This involves investigating the relationship between stimulation parameters and neural activation thresholds, exploring the effects of photovoltaic implants on neural circuits, and developing comprehensive computational models that accurately predict their behaviour in vivo.

5.4   Outlook

The photovoltaic implant, despite its current limitations in vivo, holds promise for several exciting applications. Its wireless nature, relying solely on light stimulation, makes it partic-

ularly attractive for temporary patches used to assess neurological function. Compared to other wireless methods, such as radiofrequency or magnetic induction, light sources simplify the experimental setup and reduce the learning curve. By eliminating the need for wires, such patches could offer a more convenient and comfortable option for patients undergoing diagnostic procedures or monitoring neurological activity. Furthermore, the implant's ability to stimulate neural organoids, as demonstrated in this work, opens up possibilities for utilizing it as a research tool to investigate neural development, disease mechanisms, and potential therapeutic interventions in a controlled in vitro environment. The compact and non-invasive nature of light delivery makes the freestanding photovoltaic implant ideal for use with delicate organoid structures, avoiding the bulk and potential damage associated with implanted coils or antennas. The ease of wireless stimulation afforded by the photovoltaic implant could facilitate high-throughput screening of drugs and other interventions, accelerating the discovery of novel treatments for neurological disorders.

In conclusion, this thesis has laid the groundwork for future advancements in organic photovoltaic neural implants. By addressing the challenges identified in this work and continuing to refine the technology, the photovoltaic implant holds immense potential to transform the field of neuromodulation. The successful development of a reliable, efficient, and biocompatible photovoltaic implant could assist in treating neurological disorders, offering new hope and improved quality of life for countless patients.

A Appendix

A.1 Impedance of IrOx electrodes

This section examines the impedance characteristics of the IrOx-coated electrodes (Figure 3.5) used in in vivo neural implants.

A.1.1 Methods and Results

Electrochemical impedance spectroscopy was performed with a potentiostat (Autolab PG-STAT128n, Metrohm) in a 3-electrode configuration with the working electrode, the Ag/AgCl reference and a large Pt counter electrode immersed in 1x PBS solution. The impedance was measured from 1 Hz to 100 kHz with an input signal amplitude of 100 mV rms.

The PI implants of Figure 3.5 were assessed for their impedance, comparing the different electrode diameters with a IrOx coating. The larger 80 μm electrodes had the lowest impedance magnitude (Figure A.1) with the smallest 20 μm electrodes having the highest impedance.
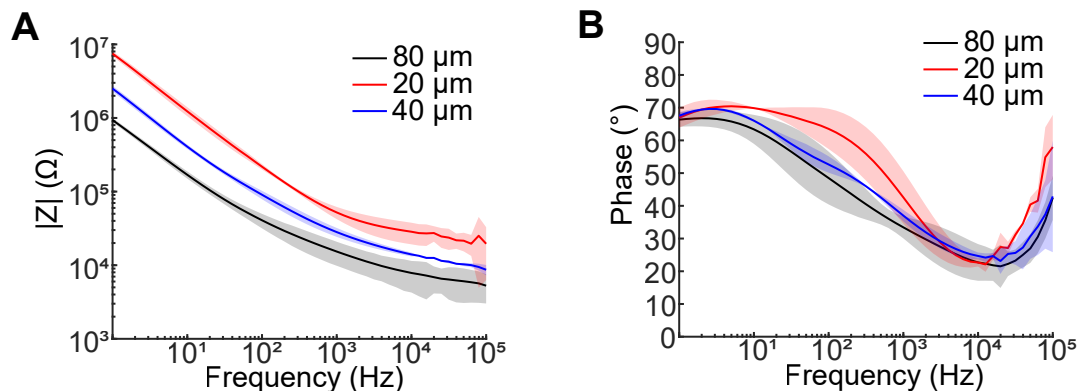
Figure A.1: **Impedance of electrical in vivo devices** A) Impedance magnitude for 80 µm (black, n = 52), 20 µm (red, n = 3) and 40 µm (blue, n = 2) electrode diameters (mean ± std) A) Phase angle for 80 µm (black, n = 52), 20 µm (red, n = 3) and 40 µm (blue, n = 2) electrode diameters (mean ± std)

.

A.2 Using an Off-stoichiometry thiol-ene-epoxy (OSTE+) thermoset as the substrate material

Adapted from Borda*, Medagoda* et al.[108]

This section details the potential of OSTE+ thermoset, a biocompatible polymer, as a substrate material for neural implants, evaluating its mechanical properties, barrier properties, and overall suitability for integration with PV implants.

A.2.1 Methods

OSTEMER 324 Flex (Mercene Labs) was prepared by mixing the two components in a 1.24:1 ratio. OSTEMER 324 Flex mix was spin-coated (1000 rpm, 60 s) onto 4-inch silicon (Si) wafers previously coated with a sacrificial layer in poly(4-styrene-sulfonic acid) (PSS; 561223, Sigma Aldrich). Thiol-ene photopolymerisation was performed under UV light in an exposure box (365 nm, 2 min; Gia-Tec). This step was repeated five times to reach a thickness of 150 µm. Then, samples were baked overnight at 95 °C to complete the thiol-epoxy thermal polymerisation from the thiol excess. Once fully cured, samples were cut by laser (10 J; WS Turret200, Optec Laser Systems) and released in deionised water.

Mechanical properties of OSTEMER 324 Flex samples were determined by dynamic mechanical and thermal analysis (DMTA; DMA Q800, TA Instruments) and tensile testing (MTS Systems Corporation). DMTA was operated using a 150 µm thick sample at a thermal ramping of 0.2 °C s^{-1} and a measurement frequency of 1 Hz. For the tensile test, 150 µm thick dog-bone-shaped samples (ASTM D412) were mounted in the MTS grips, and the crosshead speed was set at 1% of the length between the grips (in mm s^{-1}). The displacement and the corresponding

force during the test were recorded automatically using the MTS TestSuite™ TW Software (MTS Systems Corporation). Tests were performed in dry condition at room temperature (RT), dry condition at 37 °C and in wet condition (immersed in deionised water) at 37 °C using the Bionix® EnviroBath (MTS Systems Corporation). The Young's modulus was then calculated as the slope of the curve between 0 and 2% strain using MATLAB (MathWorks), while the strain and stress at break were defined as the strain and stress corresponding to the fracture point. PI samples for the tensile test were prepared by spin-coating PI (PI2611, HD MicroSystems) on a 4-inch Si wafer (1500 rpm, 60 s), soft-baking at 65 °C (5 min) and 95 °C (5 min), and hard-baking at 200 °C (1 h) and 300 °C (1 h) both in a nitrogen atmosphere. Samples were cut by laser and peeled off the wafer. PI thickness was 8 μm.

Samples were prepared by spin-coating PI, at 2500 rpm for 60 s to obtain a thickness of 5 μm. This was then plasma activated with oxygen plasma (30 W, 30 s) before spin-coating with OSTEMER 324 Flex mix (3000 rpm, 60 s) to obtain a 4 μm thickness then polymerized and baked as above. Samples of 2 cm radius were then cut by laser and peeled from the wafer. WVTR was measured at 37°C and 50% relative humidity (RH) using a permeation cell (Systech Instrument 7001).

A.2.2   Results and Discussion

Ultra-thin layers of PI, PaC and SU-8 allow device flexibility. However, the relatively high Young's modulus (GPa range) and limited elastic deformation make them less attractive than elastomers like PDMS (MPa range). OSTEMER 324 Flex closes this gap in neural interfaces. DMTA revealed that the glass transition temperature was 29.2°C (Figure A.2a, green circle) lower than the operating body temperature for neural implants (37°C). This feature is interesting compared to other materials (PI, parylene-C, SU-8 and PDMS) because OSTEMER 324 Flex is stiffer at room temperature for easier handling and softens once inserted into the body meaning reduced mechanical mismatch. Accordingly, the storage moduli at room (21 °C) and physiological (37 °C) temperatures are respectively 323.7 MPa and 15.2 MPa (Figure A.2a, red circles).

Then, we performed tensile tests (Figure A.2b) to quantify the Young's modulus (Figure A.2c), the stress at break (Figure A.2d), and the strain at break (Figure A.2e). At RT and dry (black in Figure A.2b–e), OSTEMER 324 Flex samples have an average Young's modulus of 26.19 ± 4.20 MPa, an average stress at break of 13.10 ± 4.06 MPa and an average strain at break of 69.32 ± 14.04% (n = 9 samples, mean ± s.d.). This condition represents the moment of handling the implant before implantation when the stress and strain levels are the highest. Next, the experiment was repeated at 37 °C and dry (red in Figure A.2b–e). The average Young's modulus is reduced to 12.97 ± 4.07 MPa, the average stress at break to 4.27 ± 1.69 MPa and the average strain at break to 32.72 ± 13.36% (n = 6 samples, mean ± s.d.). Similarly, at 37 °C and wet (blue in Figure A.2b–e), the average Young's modulus is reduced to 10.29 ± 4.56 MPa, the average stress at break to 3.50 ± 0.43 MPa and the average strain at break to 26.18 ± 6.58% (n = 6

samples, mean ± s.d.). Overall, the temperature increase from RT to body temperature (37 °C) significantly reduces the Young's modulus, the stress at break and the strain at break. Sample wetting did not alter mechanical properties as no significant difference was found between the dry and wet conditions at 37 °C. The sample at 37 °C and wet represents the implanted condition during which the implant softens and increases its conformability. At the same time, the reduction of the stress and strain at break is not a concern as the stress and strain levels are much lower after implantation than during the preceding manipulation. Moreover, an average strain at break of 26.18% is largely above the small and large movements in the brain. For comparison, results from tensile stress/strain tests in conformable PI samples (8 μm thick) at RT and dry are reported in Figure A.2f.

These promising mechanical properties should be considered with the encapsulation requirements of the photovoltaic pixel. A reduced strain at break at the operating temperature means less support for the rigid, brittle ITO component increasing the likelihood of cracking of the pixel. Also as explored, (Section 4), water ingress into the sample is quite damaging. When compared to similar thicknesses of PI and PaC, OSTE has a much higher water vapour transmission rate ($120 ± 9.26$ g/m^2/day (mean ± std, n = 4) vs 7.02 and 5.12) discounting its use for a PV implant.
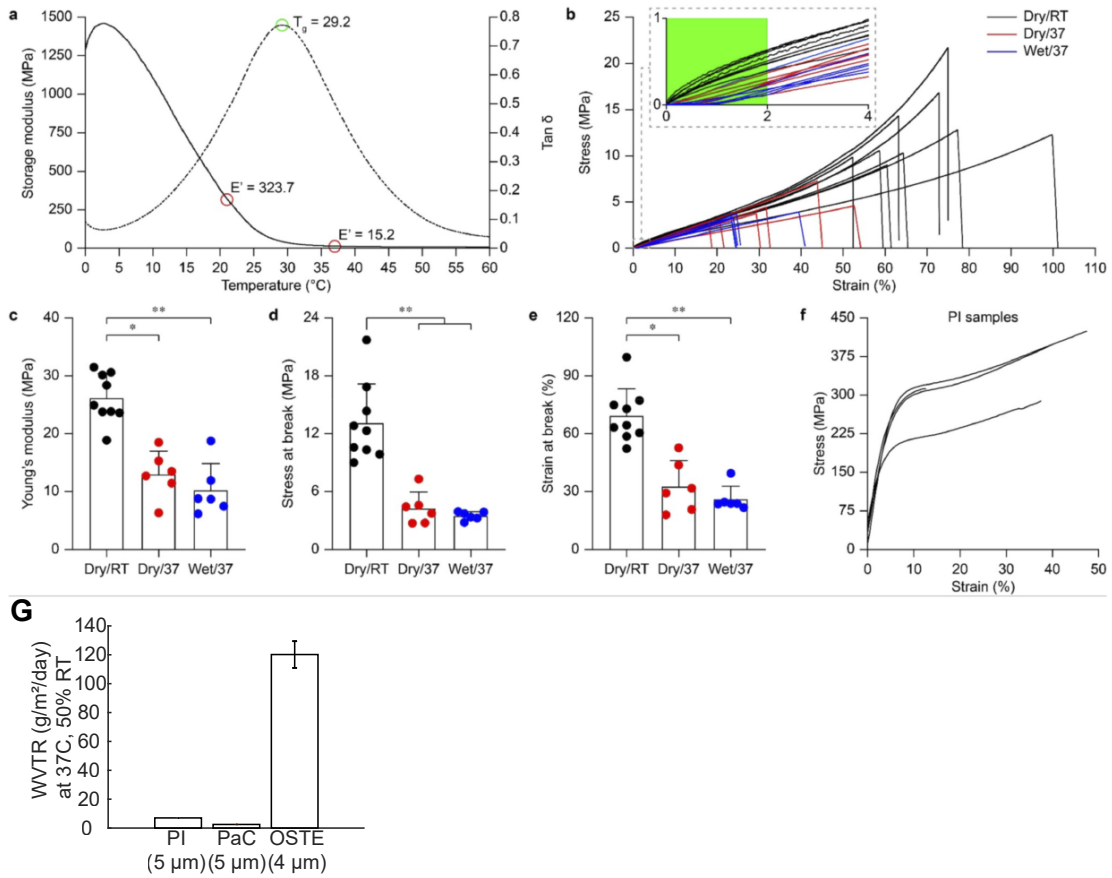
Figure A.2: **Properties of OSTEMER 324 Flex** (a) DMTA in one OSTEMER 324 Flex sample. The black line is the storage modulus, and the dashed line is the tan δ as a function of the temperature. The green circle highlights the Tg, and the two red circles highlight the storage modulus at 21 and 37 °C. (b) Stress-strain curves of OSTEMER 324 Flex samples under tensile test at RT and dry (black, n = 9), at 37 °C and dry (red, n = 6) and at 37 °C and wet (blue, n = 6). The inset shows a magnification of the stress-strain curves at the beginning of the elastic phase. The green area highlights the region used to compute the Young's modulus. (c-e) Quantification of the Young's modulus (c), stress at break (d) and strain at break (e) in OSTEMER 324 Flex samples at RT and dry (black, n = 9), at 37 °C and dry (red, n = 6), and at 37 °C and wet (blue, n = 6). Bar plots are mean ± s.d. Asterisks indicate the significance levels: *p < 0.05, **p < 0.01. (f) Stress-strain curves were obtained from four conformable PI samples at RT and dry. *Figures (a) - (f) adapted from Borda, Medagoda et al.[108]* G) Water Vapour Transmission Rate (WTVR) for different polymer materials used for neural implants. PI from Wu et al.[147], PaC from Kim et al.[146]. OSTEMER 324 Flex (OSTE) as mean ± std, n = 4)

.

A.3   Minimizing the amount of PaC in the implant

This section describes the fabrication and testing of non-functional photovoltaic implant prototypes using Parylene C, evaluating the minimum connectivity required to prevent self-folding and assessing electrical performance under cyclic bending.

A.3.1   Methods

Device fabrication was done similarly to Section 4 without the PV cell patterning. Briefly, Parylene C (2.5 μm) was deposited on a 4-inch Si wafer through vapor-phase deposition and photolithography was performed prior to sputtering with SiOx (10 nm), ITO (300 nm), IrOx (20 nm), Ir (10 nm), Pt (200 nm), Ir (10 nm) and IrOx (100 nm). Lift-off was then performed to leave the mock pixels on the Parylene C surface. Notably, this leaves a freestanding hexagon without any extensions as per a standard PV implant. Devices were then laser cut, with the design depending on the number of connections, and peeled from the Si wafer.

For the ITO-only devices, only SiOx and ITO were sputtered on PaC and fully connected devices were fabricated. The design included extensions of the ITO layer onto the bridge to visualize bending on these extensions and longer arms to allow for attachment to the bending machine.

To assess the effect of handling on the folding of pixels, devices were manipulated by placing them on a wet curved glass surface and then a dry surface and this was repeated twice more. Following this, devices were placed on a flat surface and observed under the microscope counting the number of extended pixels.

A.3.2   Results and discussion

PaC is transparent, has a better WVTR and is commonly used in neural implants thus suitable for use in the PV implant. In the pursuit of a minimally invasive device, different thicknesses of PaC were explored with 2.5 μm being the lowest thickness that allowed for reasonable handling. From here, the ability to remove more material around the PV pixels was explored. An array of 37 non-functional pixels, with only ITO, Pt and IrIx were fabricated atop 2.5 μm then laser cut a different number of connections between pixels (Figure A.3A). A fully connected device comprised of 90 connections between pixels with each pixel being connected with three thin bridges to its neighbouring pixels. The width of these bridges was either 80 μm or 40 μm. These connections were removed down to 39 (43%), below which it was impossible to remove from the wafer without folding. The array was transferred between multiple wet and dry surfaces and their final conformation was assessed for pixels that had folded into themselves or remained extended. For the 80 μm bridge width, 73% connectivity was needed before pixels began to fold onto themselves while with the thinner 40 μm bridges, any uniform removal of connections led to the folding of some pixels with more than 50% of pixels folded when there were less than 45 connections remaining. (Figure A.3A,B).

These devices were further investigated for their electrical properties, with only ITO on top as the most brittle component of the PV pixel. Devices underwent cycling bending to a radius of 2.3 mm, the radius of curvature of the mouse brain, by clamping the extremities and reducing their distance to 3 mm. For both widths, the bending did not change the resistance of the ITO pixels up to 10,000 cycles (Figure A.3D,E), well above the amount of bending considered plausible for the implants. This was due to the PaC and the thin bridges being the components that underwent deformation during the cyclic bending while the larger hexagon remained intact (Figure A.3C).
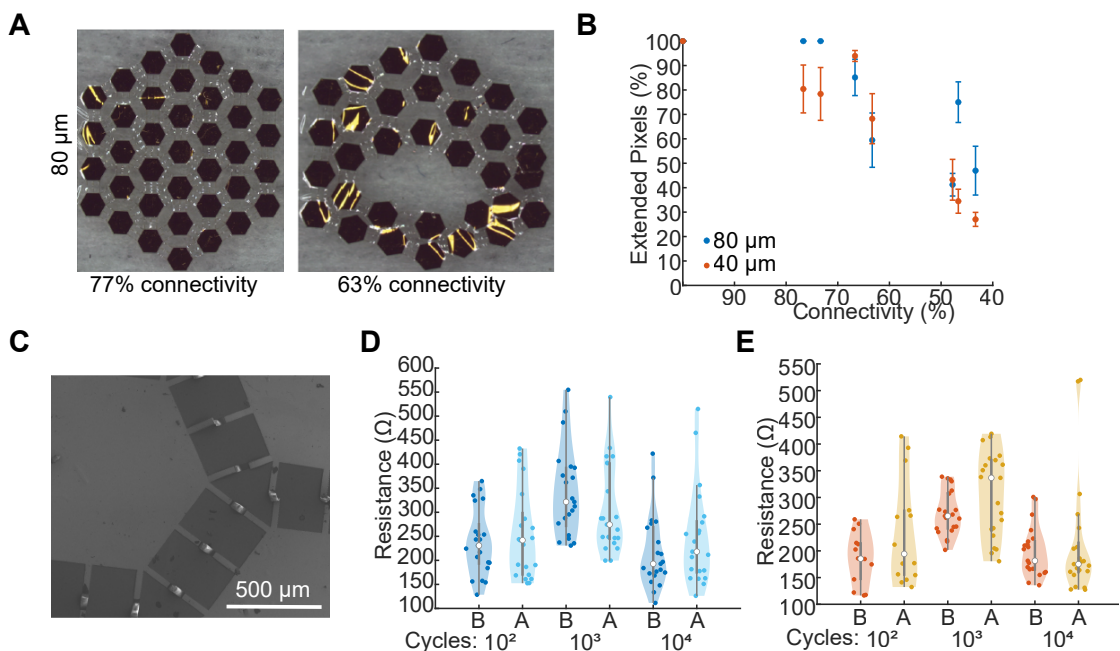
Figure A.3: **Mechanical challenging of mock PV devices on a 2.5 μm Parylene C substrate** A) An intact (left) and folded (right) device with different connectivity levels. B) Percentage of extended pixels relative to their connectivity for 80 μm (blue, n = 6) and 40 μm (orange, n = 6) bridge width after three manipulations. C) SEM image of ITO-only mock samples with PaC between underneath. The scale bar is 500 μm. D) Resistance of ITO before (orange) and after (yellow) 100, 1000 and 10000 bending cycles for fully connected 80 μm wide bridge devices. E) Resistance of ITO before (dark blue) and after (light blue) 100, 1000 and 10000 bending cycles for fully connected 40 μm wide bridge devices.

A.4 Stability of NIR-sensitive pixels in PBS at 57°C with single layer complete encapsulation

This section examines the longevity of photovoltaic pixels under simulated biological conditions, evaluating the efficacy of different encapsulation materials in preventing device degradation in a heated aqueous environment.

A.4.1 Methods

JV devices were fabricated and assessed as previously. In the case of JV measurements, which normally do not involve an encapsulation process, several modifications had to be incorporated. For pixels encapsulated with epoxy, they were first soldered with connector wires then completely covered with epoxy (Araldite® RAPID) and left to cure for 1 hour at room temperature before measurement. When encapsulated with PaC (5 or 10 μm), chips were soldered, the contacts covered in epoxy then the entire chip was coated in PaC. The ends of the wires were then stripped before measurement.

Al_2O_3 and TiO_2 were deposited via atomic layer deposition (ALD). The contacts of the fabricated chips were covered in polyimide tape and then coated with the appropriate material (Beneq TFS200). For Al_2O_3, deposition took place at 100°C using Trimethyl aluminium (TMAl) and deionized water (H_2O) precursors. TMAl precursor was flowed into the chamber for 0.4 s and then purged for 30 seconds before 0.4 s of H_2O was flowed for 0.4 s and purged. This was repeated until the desired thickness was reached. In the plasma-enhanced deposition process, the flow of precursors was preceded by a plasma step of 1 s and purge. A similar process was employed for TiO_2 with a $TiCl_4$ and H_2O precursor at a deposition temperature of 90°C.

Measurements were conducted as in Section 4 at each relevant time point. For JV samples, the chip was fully immersed in 37°C PBS then removed and dried before measurement. For pulsed light samples, the electrodes remained in 0.9% saline at RT for the duration of the experiment.

A.4.2 Results and Discussion

A crucial consideration for neural implants is their lifespan during exposure to the biological environment. To mimic this process, pixels designed for JV characterization (Figure 4.11C) were coated in a single layer of encapsulation material leaving the contacts open. Wires were then soldered to the contacts and completely covered in epoxy. The materials tested were epoxy, a bare device, PaC, and materials deposited by ALD, Al_2O_3 and TiO_2.

In all cases, bar the thick layer of water-resistant epoxy, the pixels began degradation in the first half hour (Figure A.4B-G). Compared to the bare devices, PaC encapsulation slowed the rate of loss of J_{sc} and PCE by half and maintained a mediocre level of V_{oc} after 1.5 hours (Figure A.4B-D). The difference between the PaC 5 μm and 10 μm samples points to inconsistencies in

the deposition process from the machine. All processes involving ALD-deposited materials, either with (P) or without (T) plasma-enhancement, also completely lost their efficiency after 2 hours in the heated aqueous environment (Figure A.4E-G). Given that these were single-layer materials, or depositing immediately afterwards, in the case of TiO_2, this loss in efficiency means that the aqueous solution, or water alone, was entering the pixel after diffusing through the encapsulation resulting in failure of the pixels. There is a possibility, however, that the soldering and annealing process itself, led to defects within the encapsulation films and their consequential failure.
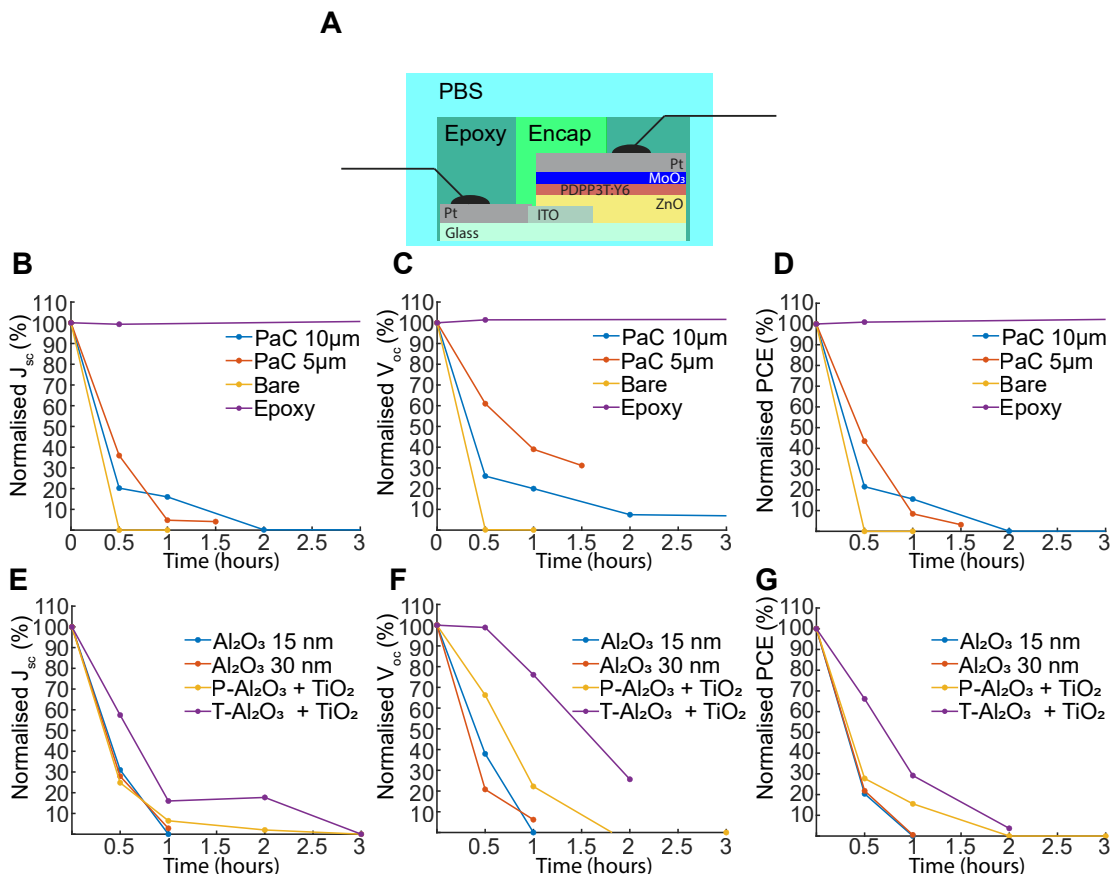
Figure A.4: **Degradation of PV pixels in PBS with polymer and encapsulations** A) The experimental set-up with the given encapsulation covering the complete pixel itself and the sidewalls while the epoxy coats the contact sides and soldered wire. This chip is then immersed in 57°C PBS and dried for measurement before re-immersion. B) The normalised J_{sc} C) V_{oc} and D) PCE for pixels coated in PaC 10 μm (blue, n = 12), PaC 5 μm (orange, n = 12), unencapsulated (yellow, n = 6) or in epoxy (purple, n = 6) E) The normalised J_{sc} F) V_{oc} and G) PCE for pixels coated in thermal ALD Al_2O_3 15 nm (blue, n = 24), thermal ALD Al_2O_3 30 nm (orange, n = 24), plasma-enhanced ALD Al_2O_3 15 nm and TiO_2 20 nm (yellow, n = 24) or in thermal ALD Al_2O_3 and TiO_2 20 nm (purple, n = 24). Each value was divided by its value at t = 0 and the mean was plotted.

Bibliography

1. Lozano, A. M. *et al.* Deep brain stimulation: current challenges and future directions. *Nature Reviews Neurology* **15,** 148–160 (2019).

2. Mo, J.-J. *et al.* Motor cortex stimulation: a systematic literature-based analysis of effectiveness and case series experience. *BMC neurology* **19,** 1–9 (2019).

3. Kathe, C. *et al.* The neurons that restore walking after paralysis. *Nature* **611,** 540–547 (2022).

4. Rao, V. R. & Rolston, J. D. Unearthing the mechanisms of responsive neurostimulation for epilepsy. *Communications Medicine* **3,** 166 (2023).

5. Shipton, E. A. *et al.* Movement disorders and neuromodulation. *Neurology Research International* **2012** (2012).

6. Lenarz, T. Cochlear implant–state of the art. *Laryngo-rhino-otologie* **96,** S123–S151 (2017).

7. Isagulyan, E. *et al.* Spinal cord stimulation in chronic pain: technical advances. *The Korean Journal of Pain* **33,** 99 (2020).

8. Lorach, H. *et al.* Walking naturally after spinal cord injury using a brain–spine interface. *Nature* **618,** 126–133 (2023).

9. Lin, T., Gargya, A., Singh, H., Sivanesan, E. & Gulati, A. Mechanism of peripheral nerve stimulation in chronic pain. *Pain Medicine* **21,** S6–S12 (2020).

10. Tilborghs, S. & De Wachter, S. Sacral neuromodulation for the treatment of overactive bladder: systematic review and future prospects. *Expert review of medical devices* **19,** 161–187 (2022).

11. Worsøe, J., Rasmussen, M., Christensen, P., Krogh, K., *et al.* Neurostimulation for neurogenic bowel dysfunction. *Gastroenterology Research and Practice* **2013** (2013).

12. Wang, Y. *et al.* Vagus nerve stimulation in brain diseases: Therapeutic applications and biological mechanisms. *Neuroscience & Biobehavioral Reviews* **127,** 37–53 (2021).

13. Erhardt, J. B. *et al.* Should patients with brain implants undergo MRI? *Journal of neural engineering* **15,** 041002 (2018).

14. Koch, J., Schuettler, M., Pasluosta, C. & Stieglitz, T. Electrical connectors for neural implants: design, state of the art and future challenges of an underestimated component. *Journal of neural engineering* **16,** 061002 (2019).

15. Gulino, M., Kim, D., Pané, S., Santos, S. D. & Pêgo, A. P. Tissue response to neural implants: the use of model systems toward new design solutions of implantable micro-electrodes. *Frontiers in neuroscience* **13,** 454701 (2019).

16. Simões, M., Simões, L. C. & Vieira, M. J. A review of current and emergent biofilm control strategies. *LWT-Food Science and Technology* **43,** 573–583 (2010).

17. Lecomte, A., Descamps, E. & Bergaud, C. A review on mechanical considerations for chronically-implanted neural probes. *Journal of neural engineering* **15,** 031001 (2018).

18. Delbeke, J., Haesler, S. & Prodanov, D. Failure modes of implanted neural interfaces. *Neural Interface engineering: Linking the physical world and the nervous system,* 123–172 (2020).

19. Anderson, J. M., Rodriguez, A. & Chang, D. T. *Foreign body reaction to biomaterials* in *Seminars in immunology* **20** (2008), 86–100.

20. Carnicer-Lombarte, A., Chen, S.-T., Malliaras, G. G. & Barone, D. G. Foreign body reaction to implanted biomaterials and its impact in nerve neuroprosthetics. *Frontiers in Bioengineering and Biotechnology* **9,** 622524 (2021).

21. Lacour, S. P., Courtine, G. & Guck, J. Materials and technologies for soft implantable neuroprostheses. *Nature Reviews Materials* **1,** 1–14 (2016).

22. Hassler, C., Boretius, T. & Stieglitz, T. Polymers for neural implants. *Journal of Polymer Science Part B: Polymer Physics* **49,** 18–33 (2011).

23. Dimov, I. B., Moser, M., Malliaras, G. G. & McCulloch, I. Semiconducting polymers for neural applications. *Chemical reviews* **122,** 4356–4396 (2022).

24. Gori, M., Vadalà, G., Giannitelli, S. M., Denaro, V. & Di Pino, G. Biomedical and tissue engineering strategies to control foreign body reaction to invasive neural electrodes. *Frontiers in Bioengineering and Biotechnology* **9,** 659033 (2021).

25. Yang, Q. *et al.* Zwitterionic polymer coating suppresses microglial encapsulation to neural implants in vitro and in vivo. *Advanced biosystems* **4,** 1900287 (2020).

26. Harawaza, K., Cousins, B., Roach, P. & Fernandez, A. Modification of the surface nanotopography of implant devices: A translational perspective. *Materials Today Bio* **12,** 100152 (2021).

27. Yuk, H., Wu, J. & Zhao, X. Hydrogel interfaces for merging humans and machines. *Nature Reviews Materials* **7,** 935–952 (2022).

28. Barbruni, G. L., Ros, P. M., Demarchi, D., Carrara, S. & Ghezzi, D. Miniaturised wireless power transfer systems for neurostimulation: A review. *IEEE Transactions on Biomedical Circuits and Systems* **14,** 1160–1178 (2020).

29. Fini, M. & Tyler, W. J. Transcranial focused ultrasound: a new tool for non-invasive neuromodulation. *International Review of Psychiatry* **29,** 168–177 (2017).

30. Sun, T., Wright, J. & Datta-Chaudhuri, T. Ultrasound powered piezoelectric neurostimulation devices: a commentary. *Bioelectronic Medicine* **6,** 16 (2020).

31. Kamimura, H. A., Conti, A., Toschi, N. & Konofagou, E. E. Ultrasound neuromodulation: Mechanisms and the potential of multimodal stimulation for neuronal function assessment. *Frontiers in physics* **8,** 150 (2020).

32. Saha, R. *et al.* A review on magnetic and spintronic neurostimulation: challenges and prospects. *Nanotechnology* **33,** 182004 (2022).

33. Chen, J. C. *et al.* A wireless millimetric magnetoelectric implant for the endovascular stimulation of peripheral nerves. *Nature Biomedical Engineering* **6,** 706–716 (2022).

34. Palanker, D., Le Mer, Y., Mohand-Said, S. & Sahel, J.-A. Simultaneous perception of prosthetic and natural vision in AMD patients. *Nature communications* **13,** 513 (2022).

35. Shen, Y., Campbell, R. E., Côté, D. C. & Paquet, M.-E. Challenges for therapeutic applications of opsin-based optogenetic tools in humans. *Frontiers in neural circuits* **14,** 542693 (2020).

36. Golovynskyi, S. *et al.* Optical windows for head tissues in near-infrared and short-wave infrared regions: approaching transcranial light applications. *Journal of biophotonics* **11,** e201800141 (2018).

37. Green, M. A. Photovoltaics: technology overview. *Energy policy* **28,** 989–998 (2000).

38. Kant, N. & Singh, P. Review of next generation photovoltaic solar cell technology and comparative materialistic development. *Materials Today: Proceedings* **56,** 3460–3470 (2022).

39. Płaczek-Popko, E. Top PV market solar cells 2016. *Opto-Electronics Review* **25,** 55–64 (2017).

40. Fukuda, K., Yu, K. & Someya, T. The future of flexible organic solar cells. *Advanced Energy Materials* **10,** 2000765 (2020).

41. National Renewable Energy Laboratory (NREL). *Best Research-Cell Efficiency Chart* https://www.nrel.gov/pv/cell-efficiency.html. [Online; accessed 16-May-2024].

42. Lin, C.-F., Su, W.-F., Wu, C.-I. & Cheng, I.-C. *Organic, Inorganic and Hybrid Solar Cells: Principles and Practice* (John Wiley & Sons, 2012).

43. Commons, W. *Band Gap Comparison* https://commons.wikimedia.org/wiki/File:Band_gap_comparison.svg. [Online; accessed 16-May-2024]. Sept. 2015.

44. Images SI, Inc. *How Photovoltaic Cells Generate Electricity* https://www.imagesco.com/articles/photovoltaic/photovoltaic-pg4.html. [Online; accessed 16-May-2024].

45. Electronics Tutorials. *Diode Theory* https://www.electronics-tutorials.ws/diode/diode_2.html. [Online; accessed 16-May-2024].

46. Palanker, D., Vankov, A., Huie, P. & Baccus, S. Design of a high-resolution optoelectronic retinal prosthesis. *Journal of neural engineering* **2,** S105 (2005).

47. Wang, L. *et al.* Photovoltaic retinal prosthesis: implant fabrication and performance. *Journal of neural engineering* **9,** 046014 (2012).

48. Wang, B.-Y. *et al.* Electronic photoreceptors enable prosthetic visual acuity matching the natural resolution in rats. *Nature communications* **13,** 6627 (2022).

49. Abdo, A. & Sahin, M. Feasibility of neural stimulation with floating-light-activated microelectrical stimulators. *IEEE transactions on biomedical circuits and systems* **5,** 179–188 (2011).

50. Abdo, A. *et al.* Floating light-activated microelectrical stimulators tested in the rat spinal cord. *Journal of neural engineering* **8,** 056012 (2011).

51. Seymour, E. Ç. *et al.* Improved selectivity from a wavelength addressable device for wireless stimulation of neural tissue. *Frontiers in neuroengineering* **7,** 5 (2014).

52. Jiang, Y. *et al.* Nongenetic optical neuromodulation with silicon-based materials. *Nature protocols* **14,** 1339–1376 (2019).

53. Huang, Y. *et al.* Bioresorbable thin-film silicon diodes for the optoelectronic excitation and inhibition of neural activities. *Nature Biomedical Engineering* **7,** 486–498 (2023).

54. Li, G., Shrotriya, V., Yao, Y. & Yang, Y. Investigation of annealing effects and film thickness dependence of polymer solar cells based on poly (3-hexylthiophene). *Journal of Applied Physics* **98** (2005).

55. Su, Y.-W., Lan, S.-C. & Wei, K.-H. Organic photovoltaics. *Materials Today* **15,** 554–562 (2012).

56. Kippelen, B. & Brédas, J.-L. Organic photovoltaics. *Energy & Environmental Science* **2,** 251–261 (2009).

57. Xu, X. & Peng, Q. Hole/electron transporting materials for nonfullerene organic solar cells. *Chemistry–A European Journal* **28,** e202104453 (2022).

58. Dang, M. T., Hirsch, L., Wantz, G. & Wuest, J. D. Controlling the morphology and performance of bulk heterojunctions in solar cells. Lessons learned from the benchmark poly (3-hexylthiophene):[6, 6]-phenyl-C61-butyric acid methyl ester system. *Chemical reviews* **113,** 3734–3765 (2013).

59. Scharber, M. C. & Sariciftci, N. S. Efficiency of bulk-heterojunction organic solar cells. *Progress in polymer science* **38,** 1929–1940 (2013).

60. Paula, T. & de Fatima Marques, M. Recent advances in polymer structures for organic solar cells: A review. *AIMS energy* **10,** 149–176 (2022).

61. Lai, T.-H., Tsang, S.-W., Manders, J. R., Chen, S. & So, F. Properties of interlayer for organic photovoltaics. *Materials Today* **16,** 424–432 (2013).

62. Ghezzi, D. *et al.* A hybrid bioorganic interface for neuronal photoactivation. *Nature communications* **2,** 166 (2011).

63. Ghezzi, D. *et al.* A polymer optoelectronic interface restores light sensitivity in blind rat retinas. *Nature Photonics* **7,** 400–406 (2013).

64. Gautam, V., Rand, D., Hanein, Y. & Narayan, K. A polymer optoelectronic interface provides visual cues to a blind retina. *Advanced Materials* **26,** 1751–1756 (2014).

65. Maya-Vetencourt, J. F. *et al.* A fully organic retinal prosthesis restores vision in a rat model of degenerative blindness. *Nature materials* **16,** 681–689 (2017).

66. Rand, D. *et al.* Direct electrical neurostimulation with organic pigment photocapacitors. *Advanced Materials* **30,** 1707292 (2018).

67. Han, M. *et al.* Photovoltaic neurointerface based on aluminum antimonide nanocrystals. *Communications Materials* **2,** 19 (2021).

68. Karatum, O. *et al.* Nanoengineering InP quantum dot-based photoactive biointerfaces for optical control of neurons. *Frontiers in neuroscience* **15,** 652608 (2021).

69. Karatum, O. *et al.* Quantum dot and electron acceptor nano-heterojunction for photo-induced capacitive charge-transfer. *Scientific reports* **11,** 2460 (2021).

70. Srivastava, S. B. *et al.* Bulk-heterojunction photocapacitors with high open-circuit voltage for low light intensity photostimulation of neurons. *Journal of Materials Chemistry C* **9,** 1755–1763 (2021).

71. Ferlauto, L. *et al.* Design and validation of a foldable and photovoltaic wide-field epiretinal prosthesis. *Nature communications* **9,** 992 (2018).

72. Chenais, N. A. L., Leccardi, M. J. I. A. & Ghezzi, D. Capacitive-like photovoltaic epiretinal stimulation enhances and narrows the network-mediated activity of retinal ganglion cells by recruiting the lateral inhibitory network. *Journal of neural engineering* **16,** 066009 (2019).

73. Chenais, N. A. L., Airaghi Leccardi, M. J. I. & Ghezzi, D. Photovoltaic retinal prosthesis restores high-resolution responses to single-pixel stimulation in blind retinas. *Communications Materials* **2,** 28 (2021).

74. Airaghi Leccardi, M. J. I. *et al.* Photovoltaic organic interface for neuronal stimulation in the near-infrared. *Communications Materials* **1,** 21 (2020).

75. Martino, N. *et al.* Photothermal cellular stimulation in functional bio-polymer interfaces. *Scientific reports* **5,** 8911 (2015).

76. Feyen, P. *et al.* Light-evoked hyperpolarization and silencing of neurons by conjugated polymers. *Scientific reports* **6,** 22718 (2016).

77. Gribi, S., du Bois de Dunilac, S., Ghezzi, D. & Lacour, S. P. A microfabricated nerve-on-a-chip platform for rapid assessment of neural conduction in explanted peripheral nerve fibers. *Nature Communications* **9,** 4403 (2018).

78. Lodola, F., Martino, N., Tullii, G., Lanzani, G. & Antognazza, M. Conjugated polymers mediate effective activation of the mammalian ion channel transient receptor potential vanilloid 1. *Scientific reports* **7,** 8477 (2017).

Bibliography

79. Shuba, Y. M. Beyond neuronal heat sensing: diversity of TRPV1 heat-capsaicin receptor-channel functions. *Frontiers in Cellular Neuroscience* **14,** 612480 (2021).

80. Silverå Ejneby, M. *et al.* Chronic electrical stimulation of peripheral nerves via deep-red light transduced by an implanted organic photocapacitor. *Nature biomedical engineering* **6,** 741–753 (2022).

81. Missey, F. *et al.* Organic electrolytic photocapacitors for stimulation of the mouse somatosensory cortex. *Journal of Neural Engineering* **18,** 066016 (2021).

82. Benfenati, V. *et al.* Photostimulation of whole-cell conductance in primary rat neocortical astrocytes mediated by organic semiconducting thin films. *Advanced healthcare materials* **3,** 392–399 (2014).

83. Doumon, N. Y. The degradation of organic solar cells: From chemistry to device physics through materials. *University of Groningen* (2019).

84. Köntges, M. *et al.* Review of failures of photovoltaic modules (2014).

85. Merrill, D. R., Bikson, M. & Jefferys, J. G. Electrical stimulation of excitable tissue: design of efficacious and safe protocols. *Journal of neuroscience methods* **141,** 171–198 (2005).

86. Cogan, S. F. Neural stimulation and recording electrodes. *Annu. Rev. Biomed. Eng.* **10,** 275–309 (2008).

87. Stieglitz, T. in *Neuroprosthetics: theory and practice* 475–516 (World Scientific, 2004).

88. Polachan, K., Chatterjee, B., Weigand, S. & Sen, S. Human body–electrode interfaces for wide-frequency sensing and communication: A review. *Nanomaterials* **11,** 2152 (2021).

89. Gaillet, V. *et al.* Spatially selective activation of the visual cortex via intraneural stimulation of the optic nerve. *Nature biomedical engineering* **4,** 181–194 (2020).

90. Dupont, S. R., Voroshazi, E., Heremans, P. & Dauskardt, R. H. Adhesion properties of inverted polymer solarcells: Processing and film structure parameters. *Organic Electronics* **14,** 1262–1270 (2013).

91. Holliday, S. *et al.* High-efficiency and air-stable P3HT-based polymer solar cells with a new non-fullerene acceptor. *Nature communications* **7,** 1–11 (2016).

92. Berger, P. & Kim, M. Polymer solar cells: P3HT: PCBM and beyond. *Journal of Renewable and Sustainable Energy* **10** (2018).

93. Meier, J. D., Aflalo, T. N., Kastner, S. & Graziano, M. S. Complex organization of human primary motor cortex: a high-resolution fMRI study. *Journal of neurophysiology* **100,** 1800–1812 (2008).

94. Tennant, K. A. *et al.* The organization of the forelimb representation of the C57BL/6 mouse motor cortex as defined by intracortical microstimulation and cytoarchitecture. *Cerebral cortex* **21,** 865–876 (2011).

95. Lecturio. *Upper and Lower Motor Neuron Lesions* https://www.lecturio.com/concepts/upper-and-lower-motor-neuron-lesions/. [Online; accessed 16-May-2024].

96. Butman, J. & Floeter, M. Decreased thickness of primary motor cortex in primary lateral sclerosis. *American journal of neuroradiology* **28,** 87–91 (2007).

97. Blech-Hermoni, Y. *et al.* Expression of LIM domain-binding 3 (LDB3), a striated muscle Z-band alternatively spliced PDZ-motif protein in the nervous system. *Scientific Reports* **13,** 270 (2023).

98. Fukui, A. *et al.* Layer-specific sensory processing impairment in the primary somatosensory cortex after motor cortex infarction. *Scientific reports* **10,** 3771 (2020).

99. Yip, D. W. & Lui, F. Physiology, motor cortical (2019).

100. Bartholow, R. Experiments on the functions of the human brain. *British medical journal* **1,** 727 (1874).

101. Ramos-Fresnedo, A. *et al.* Motor cortex stimulation for pain: a narrative review of indications, techniques, and outcomes. *Neuromodulation: Technology at the Neural Interface* **25,** 211–221 (2022).

102. Carmel, J. B. & Martin, J. H. Motor cortex electrical stimulation augments sprouting of the corticospinal tract and promotes recovery of motor function. *Frontiers in integrative neuroscience* **8,** 51 (2014).

103. Ilyas, S. *et al.* Exploring the Differential Effects of Transcranial Direct Current Stimulation: A Comparative Analysis of Motor Cortex and Cerebellar Stimulation. *Heliyon* **10** (2024).

104. Sreenivasan, V. *et al.* Movement initiation signals in mouse whisker motor cortex. *Neuron* **92,** 1368–1382 (2016).

105. Peters, A. J., Liu, H. & Komiyama, T. Learning in the rodent motor cortex. *Annual review of neuroscience* **40,** 77–97 (2017).

106. Young, N. A., Vuong, J., Flynn, C. & Teskey, G. C. Optimal parameters for microstimulation derived forelimb movement thresholds and motor maps in rats and mice. *Journal of neuroscience methods* **196,** 60–69 (2011).

107. Takemi, M. *et al.* Rapid identification of cortical motor areas in rodents by high-frequency automatic cortical stimulation and novel motor threshold algorithm. *Frontiers in Neuroscience* **11,** 295504 (2017).

108. Borda, E., Medagoda, D. I., Leccardi, M. J. I. A., Zollinger, E. G. & Ghezzi, D. Conformable neural interface based on off-stoichiometry thiol-ene-epoxy thermosets. *Biomaterials* **293,** 121979 (2023).

109. Leccardi, M. J. I. A., Vagni, P. & Ghezzi, D. Multilayer 3D electrodes for neural implants. *Journal of neural engineering* **16,** 026013 (2019).

110. Gaillet, V., Borda, E., Zollinger, E. G. & Ghezzi, D. A machine-learning algorithm correctly classifies cortical evoked potentials from both visual stimulation and electrical stimulation of the optic nerve. *Journal of Neural Engineering* **18,** 046031 (2021).

111. Uguz, I. & Shepard, K. L. Spatially controlled, bipolar, cortical stimulation with high-capacitance, mechanically flexible subdural surface microelectrode arrays. *Science Advances* **8,** eabq6354 (2022).

112. Wang, E. B. *et al.* in *Photobiomodulation in the Brain* 49–66 (Elsevier, 2019).

113. Hale, G. M. & Querry, M. R. Optical constants of water in the 200-nm to 200-μm wavelength region. *Applied optics* **12,** 555–563 (1973).

114. Jagdeo, J. R., Adams, L. E., Brody, N. I. & Siegel, D. M. Transcranial red and near infrared light transmission in a cadaveric model (2012).

115. Henderson, T. A. & Morries, L. D. Near-infrared photonic energy penetration: can infrared phototherapy effectively reach the human brain? *Neuropsychiatric disease and treatment,* 2191–2208 (2015).

116. Jean, M., Schulmeister, K., Kotzur, S. & Frederiksen, A. Validation of a generalized laser safety analysis method for irregular pulse trains. *Journal of Laser Applications* **32** (2020).

117. Wang, B.-Y., Chen, Z. C., Bhuckory, M., Goldstein, A. K. & Palanker, D. Pixel size limit of the PRIMA implants: from humans to rodents and back. *Journal of neural engineering* **19,** 055003 (2022).

118. Mohamed El Amine, B. *et al.* Latest Updates of Single-Junction Organic Solar Cells up to 20% Efficiency. *Energies* **16,** 3895 (2023).

119. Meng, D. *et al.* Near-infrared materials: the turning point of organic photovoltaics. *Advanced Materials* **34,** 2107330 (2022).

120. Grifoni, F. *et al.* Toward sustainable, colorless, and transparent photovoltaics: state of the art and perspectives for the development of selective near-infrared dye-sensitized solar cells. *Advanced Energy Materials* **11,** 2101598 (2021).

121. Luke, J., Yang, E. J., Labanti, C., Park, S. Y. & Kim, J.-S. Key molecular perspectives for high stability in organic photovoltaics. *Nature Reviews Materials* **8,** 839–852. doi:10.1038/s41578-023-00606-5 (Oct. 2023).

122. Yang, W. *et al.* Balancing the efficiency, stability, and cost potential for organic solar cells via a new figure of merit. *Joule* **5,** 1209–1230 (2021).

123. Mateker, W. R. & McGehee, M. D. Progress in understanding degradation mechanisms and improving stability in organic photovoltaics. *Advanced materials* **29,** 1603940 (2017).

124. Segbefia, O. K., Imenes, A. G. & Sætre, T. O. Moisture ingress in photovoltaic modules: A review. *Solar Energy* **224,** 889–906 (2021).

125. Mariello, M., Kim, K., Wu, K., Lacour, S. P. & Leterrier, Y. Recent advances in encapsulation of flexible bioelectronic implants: Materials, technologies, and characterization methods. *Advanced Materials* **34,** 2201129 (2022).

126. Palanker, D., Le Mer, Y., Mohand-Said, S., Muqit, M. & Sahel, J. A. Photovoltaic restoration of central vision in atrophic age-related macular degeneration. *Ophthalmology* **127,** 1097–1104 (2020).

127. Simone, G. *et al.* Near-infrared tandem organic photodiodes for future application in artificial retinal implants. *Advanced Materials* **30,** 1804678 (2018).

128. Yoon, S.-J. *et al.* Reliability of human cortical organoid generation. *Nature methods* **16,** 75–78 (2019).

129. He, K., Kumar, P., Yuan, Y. & Li, Y. Wide bandgap polymer donors for high efficiency non-fullerene acceptor based organic solar cells. *Materials Advances* **2,** 115–145 (2021).

130. Wang, J. *et al.* Enhanced performance of polymer solar cells by dipole-assisted hole extraction. *Solar energy materials and solar cells* **130,** 15–19 (2014).

131. Li, X., Kong, X., Sun, G. & Li, Y. Organic small molecule acceptor materials for organic solar cells. *eScience,* 100171 (2023).

132. Wang, H. *et al.* 14.55% efficiency PBDB-T ternary organic solar cells enabled by two alloy-forming acceptors featuring distinct structural orders. *Chemical Engineering Journal* **413,** 127444 (2021).

133. Wei, Y. *et al.* The charge-transfer states and excitation energy transfers of halogen-free organic molecules from first-principles many-body Green's function theory. *Spectrochimica Acta Part A: Molecular and Biomolecular Spectroscopy* **286,** 121925 (2023).

134. Cogan, S. F., Plante, T. & Ehrlich, J. *Sputtered iridium oxide films (SIROFs) for low-impedance neural stimulation and recording electrodes* in *The 26th Annual International Conference of the IEEE Engineering in Medicine and Biology Society* **2** (2004), 4153–4156.

135. Chiang, C.-C. & Durand, D. M. Subthreshold Oscillating Waves in Neural Tissue Propagate by Volume Conduction and Generate Interference. *Brain Sciences* **13,** 74 (2022).

136. Njok, A., Ogbulezie, J. & Akonjom, N. Evaluation of the performance of photovoltaic system under different wavelengths from artificial light in a controlled environment. *Journal of Applied Sciences and Environmental Management* **26,** 1015–1020 (2022).

137. Liu, X., Wu, S., Liang, Y., Xu, W. & Liu, H. Organic/amorphous silicon hybrid tandem solar cell with PDPP3T as organic active layer. *Microelectronics Journal* **113,** 105098 (2021).

138. Dubey, A. *et al.* Solution processed pristine PDPP3T polymer as hole transport layer for efficient perovskite solar cells with slower degradation. *Solar Energy Materials and Solar Cells* **145,** 193–199 (2016).

139. Yang, X. *et al.* Intrinsic Role of Volatile Solid Additive in High-Efficiency PM6: Y6 Series Nonfullerene Solar Cells. *Advanced Materials* **35,** 2301604 (2023).

140. Yu, K. *et al.* 18.01% Efficiency organic solar cell and 2.53% light utilization efficiency semitransparent organic solar cell enabled by optimizing PM6: Y6 active layer morphology. *Science China Chemistry* **65,** 1615–1622 (2022).

141. Silverå Ejneby, M. *et al.* Extracellular photovoltage clamp using conducting polymer-modified organic photocapacitors. *Advanced Materials Technologies* **5,** 1900860 (2020).

Bibliography

142. Jakešová, M. *et al.* Coupling of photovoltaics with neurostimulation electrodes–optical to electrolytic transduction. *Journal of Neural Engineering* (2024).

143. Zhang, Y. *et al.* Recent progress on NIR-II photothermal therapy. *Frontiers in Chemistry* **9,** 728066 (2021).

144. Xu, X., Li, D., Yuan, J., Zhou, Y. & Zou, Y. Recent advances in stability of organic solar cells. *EnergyChem* **3,** 100046 (2021).

145. Zhu, Y. *et al.* Nanostructured MoO3 for Efficient Energy and Environmental Catalysis. *Molecules* **25,** 18. doi:10.3390/molecules25010018 (Dec. 2019).

146. Kim, K. *et al.* Extended barrier lifetime of partially cracked organic/inorganic multilayers for compliant implantable electronics. *Small* **17,** 2103039 (2021).

147. Wu, K., Mariello, M., Leterrier, Y. & Lacour, S. P. Optical monitoring of water side permeation in thin film encapsulation. *Advanced Materials,* 2310201 (2024).

Danashi Medagoda

Avenue de Jurigoz 13B, 1006 Lausanne
+41 76 791 18 41
DOB : 15/06/1995

danashi.medagoda@epfl.ch
https://www.linkedin.com/in/danashi-medagoda/
B Permit Holder, Australian

EDUCATION

PhD Bioengineering | 2020 - Currently
EPFL, Geneva

MSc Bioengineering - Neuroprosthetics minor | 2017 –
2020 EPFL, Lausanne

Science and Policy – How to bridge the gap? | July 2023
Beatenberg, Switzerland

BSc Computer Science and Neuroscience | 2013 – 2016
USYD, Sydney

ACADEMIC EXPERIENCE

PhD candidate

Laboratory for Soft Bioelectronic Interfaces, Prof. Stéphanie P. Lacour. EPFL, Campus Biotech, Geneva | 2022 - Present

Laboratory of Neuroengineering, Dr. Diego Ghezzi, EPFL, Campus Biotech, Geneva | 2020 - 2022

- Developed an innovative organic photovoltaic neural interface
- Employed advanced microfabrication techniques to manufacture electrical and photovoltaic implants
- Performed animal experiments to test fabricated devices on rodent animal models

Master Thesis

Laboratory of Life Sciences Electronics, Prof. Carlotta Guiducci, EPFL, Lausanne | Autumn 2019

- Development of a biomarker assay using dielectrophoresis-based technology

Semester Project

Laboratory for Soft Bioelectronic Interfaces, Prof. Stéphanie P. Lacour. EPFL, Campus Biotech, Geneva | Spring 2018

- Optimize the extracellular matrix structure for cell growth in microchannels for a peripheral nerve-on-a-chip interface

Semester Project

Laboratory of Neuroengineering, Dr. Diego Ghezzi, EPFL, Campus Biotech, Geneva | Autumn 2018

- Fabricate stretchable interconnects using gold-coated nanowires for use in a visual prosthesis

Semester Project

Laboratory of Life Sciences Electronics, Prof. Carlotta Guiducci, EPFL, Lausanne | Autumn 2018

- Characterize single cells using impedance spectroscopy across three-dimensional electrodes and hydrodynamic trapping

Bachelor Honours Year

Bagley Laboratory, Prof. Elena Bagley, USYD, Sydney | 2016

- Assessing the effect of the change in opioid receptor expression in intercalated cells of the amygdala

WORK EXPERIENCE

Teaching Assistant | EPFL | 2020 – 2023

- Master courses: Biomaterials, Neuroengineering of Vision (Master course)
- Bachelor course: Material Science for Bioengineers

Industry Internship | bNovate | Spring 2019

- Development and optimization of a live cell assay for an advanced microfluidic system

TECHNICAL SKILLS AND EXPERTISE

Cleanroom fabrication: processing on rigid or polymer substrates, thin film sputtering and evaporation, dry etching, photolithography (direct-write system and mask aligner), glovebox manipulation, laser machining

Materials expertise: epoxies (OSTEmers, SU8), elastomers (PDMS), polyimide, parylene C, organic and inorganic semiconductor materials, organic photovoltaics and LEDs, electrode and coating materials, nanomaterials

Characterization: SEM, FIB, AFM, KPFM, electrochemical, optoelectronic, mechanical, optical

Engineering software: AutoCAD, COMSOL Multiphysics, Clewin, KLayout, Blender

Programming: Python, MATLAB, C++

Animal experimentation: RESAL Module 1, rodent neurosurgery

Design software: Adobe Illustrator, Photoshop, Premiere Pro, LaTeX, Microsoft office

LANGUAGES

English: Native

French: B2

PUBLICATIONS

- *Borda, E., ***Medagoda, D.I**., Leccardi, M.J.I.A., Zollinger, E.G. and Ghezzi, D., 2023. Conformable neural interface based on off-stoichiometry thiol-ene-epoxy thermosets. *Biomaterials,* 293, p.121979.
- **Medagoda, D.I.** and Ghezzi, D., 2021. Organic semiconductors for light-mediated neuromodulation. *Communications Materials*, 2(1), p.111.
- Thiriet, P.E., **Medagoda, D.,** Porro, G. and Guiducci, C., 2020. Rapid multianalyte microfluidic homogeneous immunoassay on electrokinetically driven beads. *Biosensors*, 10(12), p.212.
- Winters, B.L., Gregoriou, G.C., Kissiwaa, S.A., Wells, O.A., **Medagoda, D.I.,** Hermes, S.M., Burford, N.T., Alt, A., Aicher, S.A. and Bagley, E.E., 2017. Endogenous opioids regulate moment-to-moment neuronal communication and excitability. *Nature communications*, 8(1), p.14611.